POLITECNICO DI TORINO

Master Degree in Biomedical Engineering
Biomedical Instrumentation

Master Degree Thesis

Application of speckle tracking to follow the edges of the inferior vena cava

Supervisor:
Luca Mesin

Co-supervisor:
Piero Policastro

Candidate:
Elio Gregori Lombardi

December 2021

Contents

2

List of Figures

List of Tables

Abstract

The pulsatility of the inferior vena cava can be an indicator to estimate important clinical parameters such as the volemic status of a patient or the right atrial pressure. The manual measurement of the pulsatility is a time consuming task, and the results do not have an high repeatability since they can depend on multiple factors such as the experience of the physician or the section of the vena cava taken into consideration. To reduce the magnitude of those problems, an algorithm to track the displacements of the edges of the vena cava was developed at the Polytechnic University of Turin. The aim of this thesis was to develop an algorithm having the same purpose, but by using a different method: the speckle tracking. Speckle tracking is a common technique used in echocardiography to follow the displacements of the myocardial tissue. To validate the functionality of the speckle tracking algorithm, the comparison of the diameters as well as the pulsatility obtained with both algorithms was done. Also, since in literature the speckle tracking has been shown to depend on the acquisition's frame rate, the performance of the algorithm was evaluated by simulating lower frame rate acquisitions compared to the original. Finally, the beginning of a study concerning the pulsatility of the inferior vena cava for patients with pulmonary diseases was done. The echographies of the inferior vena cava on the longitudinal and transverse plane of four patients were collected by some physicians and they were processed by both the algorithms when possible, and the cardiac, respiratory and global pulsatility indexes were evaluated. The respiratory pulsatility index was always the lowest one, which seems to suggest that the vessel's rigidity for people with pulmonary diseases is mostly caused by the lower variations of pulmonary pressure.

Chapter 1

Introduction

1.1 Respiratory system physiology and anatomy

The respiratory system is responsible for the respiration process, that is the gas exchange between the body and the external environment. This process takes place in four main steps. First, the exchange between the external atmosphere and the lungs. Second, the exchange between the lungs and the blood circulating in the body. Here,the blood, rich in carbon dioxide, enters the alveolar capillaries and carbon dioxide is diffused outside the bloodstream, while oxygen in diffused inside it. Third, the transport of oxygen and CO_2 from the blood in the tissues of the whole body. When the blood leaves the alveolar capillaries rich in oxygen, before reaching tissues capillaries it passes through the pulmonary veins, right heart atrium, right ventricule and systemic arteries. Fourth and last step, the exchange through diffusion of oxygen and CO_2 between the blood and the tissues in the body. By reaching the tissue capillaries, the oxygen can diffuse inside the tissues, and the carbon dioxide in excess is diffused inside the bloodstream. The carbon dioxide will be brought back to the alveolar capillaries with the blood passing through the systemic veins, left atrium and ventricule, and pulmonary arteries.The main organs of the respiratory system are the lungs, which are located in the thoracic cavity. The right lung is composed by three lobes while the left lung is composed by two lobes. Before reaching the lungs the inspired air must pass through the upper airways. Those airways are the passages for the air which are located in the head and in the neck. First, the air penetrates through the nasal or the oral cavity, which both lead to the pharynx, a conduct which has the purpose of letting pass the air and the food. After the pharynx, the air enters the first part of the respiratory tract,the larynx, a conduct kept open thanks to the cartilage. The respiratory tract, according to Weibel[1], is composed by two main zones: the conduction zone (superior part of the respiratory tract), and the respiratory zone(inferior part of the respiratory tract). Those two zones are composed by a total of twenty-four generations of ramifications. The first seventeen generations, (from generation zero to sixteen), form the conduction zone. The first five generations are composed by a remarkable part of cartilage. In particular, the trachea and the primary bronchi have incomplete cartilage rings disposed in the form of a "C" along they whole length. Instead, in the secondary bronchi the cartilage is disposed in the form of plaques. From generation 5 to generation 11 (little bronchi), the cartilaginous content diminishes greatly, until it completely disappears in the bronchioles and the terminal bronchioles (generation twelve to sixteen). Since the bronchioles and the terminal bronchioles do not present cartilage, to avoid a mechanical collapse, they are mainly composed of elastic fibers. The main functionality of the conduction zone is to permit the entrance and the exit of the external air in the respiratory zone, where the gaseous exchanges effectively take place. The conduction zone has also heats and humidify the inspired air. The respiratory zone is constituted by respiratory bronchioles, alveolar ducts and alveolar sacs. Alveolar sacs have a form reminiscent of the grapes.

The 300 millions of alveoli in the lungs form an area of approximately 100 m^2. This great surface makes the gas exchange much more efficient. Indeed, according to Fick's law, $F = PA(\Delta C)$, where F is the flux passing through the membrane, A is the surface area of said membrane, ΔC is the concentration gradient and P is the permeability coefficient (depends from the membrane type and the transported molecule). Lungs are deprived of support or muscular structures. They are able to keep their habitual conformation thanks to the pleura, which attaches the lungs to the rib cage. The pleura covers the internal surface of the thoracic wall (parietal pleura) and the external surface of the lungs (visceral pleura).Between the two layers of pleura there is the the intrapleuric space, an extremely thin compartment full of liquid. This liquid, approximately 15 mL[2] is called the intrapleuric liquid and allows the scrolling between the two pleuras. Due to this conformation, the
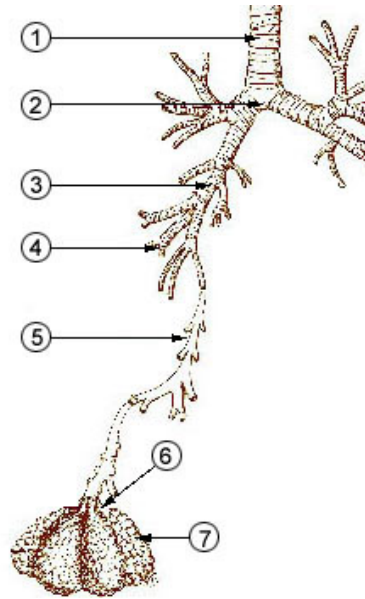
Figure 1.1: Schematic reprensentation of the "respiratory tree". 1) Trachea 2) Mainstream bronchus 3) Lobar bronchus 4)Segmental bronchus 5)Bronchiole 6)Alveolar duct 7) Alveoli (Image from wikipedia [30])

volume variations of the lungs are a result of the movements of the rib cage. The movements of the rib cage determine the respiration process, which can be divided in two phases, inspiration and expiration. The muscles responsible for the inspiration are mainly the diaphragm and the external intercostal muscles, while the ones responsible for the expiration are the internal intercostal muscles and the abdominal wall muscles. Inspiration is the expansion of the lungs volume, and does require the contraction of the inspiration muscles, while expiration is the reduction of the lungs volume, but it does not strictly require the contraction of the expiration muscles. The relaxation of the inspiration muscles is sufficient. There are four main pressures which are considered during the ventilation process:

- The atmospheric pressure, it is the external body air pressure. It has a value of 760 $mmHg$ at the sea level. It serves as a reference measure: each one of the following pressures is compared to the this one.

- The intra-alveolar pressure. It is the air pressure inside the alveoli, in resting conditions it is equivalent to the external air pressure. This means the differential is 0 $mmHg$. During phase of inspiration, this pressure diminishes, while during the expiration phase this pressure augments.

- The intrapleural pressure. It is the pressure inside the pleuric sac (the space between the two layers of pleura). In resting conditions, the value is -4 $mmHg$ compared to the atmospheric pressure. This pressure is always negative, in each phase of the respiration, because the forces exercised from the lungs and the thoracic wall are opposed and tend to separate the two layers of pleura.

3

- The transpulmonary pressure: it is the difference between the intra-alveolar pressure and the intrapleural pressure $(P_{alv} - P_{ip})$. It is an indication of the distension force through the lungs. An increase of this pressure indicates a major distension force and consequently an expansion of the lungs volume.

The air flux inside the lungs is guided by the pressure gradients. Those pressure gradients are caused by the variation of volume inside the lungs. If the volume increases, the intra-alveolar pressure decreases. The opposite is true. The flux can then be represented with the following formula: $\frac{P_{atm} - P_{alv}}{R}$. R represents the resistance against the air flux. A last factor which can have effects on the respiration process is the pulmonary compliance. It is represented by the ratio between the variation of volume and the variation of transpulmonary pressure : $\frac{\Delta V}{\Delta(P_{alv} - P_{ip})}$. An altered compliance is usually the result of pulmonary diseases.

1.2   Pulmonary Diseases

1.2.1   Emphysema

An emphysema is a type of chronic obstructive pulmonary disease (COPD). Obstructive diseases are a result of chronic inflammations of the lungs. Those inflammations often cause an overproduction of mucus, a thickening of the bronchial walls and, in the case of the emphysema, damage to the air sacs. More specifically, the inner walls of the air sacs become weakened and end up rupturing[4]. This leads to a reduced surface of the total number of alveoli, and so the gaseous exchange between the lungs and the blood is much less efficient. The principal symptom of the emphysema is the dyspnea, a condition where the patient feels he can not breathe enough air. When the emphysema is less acute, dyspnea can manifest just when the patient does physical activity, but as the disease worsen, this symptom may appear even in resting conditions. Other symptoms can be a cough that produces a lot of mucus, frequent coughing, tightness in the chest, wheezing. The risk factors of emphysema are the following[3][4]:

- Smoking: this one is the main risk factor. Most of the people diagnosed with an emphysema are smokers or used to smoke. Obviously the risk increases the more the person smokes.

- Age: the damage in the lungs develops over time, and generally the symptoms begin to manifest in people between 40 and 60 years old

- Exposure to pollution

- Passive smoke

- Genetics: can be caused by alpha-1 antitrypsin deficiency. Also, patients with emphysema are more likely to have other family members with COPD

The emphysema can also result in severe complications such as a collapsed lung (can be a life threatening condition) and increase of the pressure in the arteries that connect heart and lungs. The emphysema is generally diagnosed by doing functional lung tests (such as spirometry,lung volume test , gas diffusion test, exercise stress test), a chest x-ray, an high resolution computed tomography (HRCT), blood tests, asking about the symptoms and the family medical history.

1.2.2   Fibrosis

The pulmonary fibrosis is a type of restrictive respiratory disease. In those types of diseases, the lungs or chest muscles are not able to expand enough. There is a reduction of the pulmonary compliance, since for the same gradient of pressure generated by the muscles the gradient of volume is lesser. This reduces air flow and the ability to send oxygen into the bloodstream. In the pulmonary fibrosis, the lung tissue becomes scarred over time, which causes the stiffness of lungs. Finding the causes of pulmonary fibrosis is not always an easy task. The main causes of fibrosis are the following[5]:

- Drug induced: there are some medications which are implied to cause injury, inflammation, and scarring in the lungs. Some of them can be used to treat cancer, abnormal heart rhythms(such as amiodarone), to treat inflammatory conditions (such as methotrexate), and to treat urinary tract infections (nitrofurantoin).

- Radiation induced: it is usually a late complication of radiation therapy and may occur weeks or even years after treatment.

- Environmental causes : can be triggered when lungs react with inflammation and scarring after breathing in mold spores, bacteria or animal proteins.

- Autoimmune diseases such as Rheumatoid arthritis or scleroderma can cause the body's immune system to attack the lungs and cause the subsequent scarring

- Occupational causes: fibrosis can develop after significant exposure to a wide variety of inorganic dusts, including asbestos, silica, coal dust, beryllium, and hard metal dusts.

There can be more than one cause of fibrosis. When the clinician can not establish the cause, the fibrosis is idiopathic. The main symptoms are dry, hacking cough and shortness of breath. At the beginning of the scarring process, those symptoms can be present in a reduced form or even be absent. As the condition worsen, so do the symptoms. Other symptoms can be fatigue and weakness, discomfort in the chest, loss of appetite and unexplained weight loss. To diagnose the fibrosis the clinician may want to check the stiffness of the lungs with pulmonary function tests, the oxygen level after some physical activity, and if there are crackle sounds (sounds similar to velcro) while the patient breathes. To find out which specific type of fibrosis the patient haves, the clinician may want to perform blood tests, lung biopsy or an HRCT.

1.2.3   Combined Pulmonary fibrosis and emphysema

The combined pulmonary fibrosis and emphysema (CPFE) is the clinical manifestation of both fibrosis and emphysema in a patient. As such, the risk factors are the ones of those diseases mentioned earlier, with smoking being the main one. CPFE can be harder to diagnose than an emphysema or a fibrosis. This is due to the opposite physiological of those two diseases. For instance, an emphysema implies an increased compliance and a decreased recoil of the lungs, while the fibrosis presents an increased recoil and a decreased compliance. The combination of those two factors results in lung volumes and capacity which are often in the regular range[27], as well as standard functional tests such as the FEV_1. This renders the diagnosis more complicated through spirometry. Indeed, the CPFE is often diagnosed with HRCT, where it is possible to see anatomical alterations caused by both the emphysema and the fibrosis. Also, CPFE presents altered values

in the DLCO test. The CPFE can lead to pulmonary hypertension (condition where the pressure in the pulmonary artery and in the right part of the heart is increased), an acute pulmonary injury, and also increases the chances of lung cancer.

1.3 Diagnostic instrumentation

1.3.1 Computed Tomography

Before discussing how computed tomography works, it is necessary to explain the principal characteristics of X-Rays. They are ionizing radiations with a wavelength between 10 pm and 100 nm. Their frequency varies between $3 \cdot 10^{16}$ and $3 \cdot 10^{21}$ Hz. Due to their high frequencies, x-rays can penetrate and reemerge from the human body tissue. This property is used to visualize anatomical zones inside of the body. One of the main drawback of the x-rays is that they can alter the physical and chemical properties of the exposed tissues. It is an invasive diagnostic method. X-rays are transmitted from an x-ray tube, the beam passes through the patient, and collide on a device which has the task to capture the information (it can be a film or a multitude of sensors).

The formed image on the receptor is a result of the interaction between the x-rays and the human tissues. Let us suppose that there is an x-ray beam constituted by photons which all have identical energy. This beam passes through a material with a thickness dx. But the number of photons which exit the material is inferior to the number of photons which enter it. So the material absorbs some photons proportionally to his thickness. This way, we have the following equation[6]:

$$\frac{dN}{N} = -\mu dx$$

By integrating, we obtain:

$$\int_{N}^{N_0} \frac{dN}{N} = -\mu \int_{0}^{x} dx$$

$$ln(\frac{N_0}{N}) = -\mu x$$

$$\frac{N_0}{N} = e^{-\mu x}$$

$$N_0 = N e^{-\mu x}$$

N represents the number of entering photons, N_0 is the number of exiting photons, μ is the linear attenuation coefficient of the material and x is the thickness of the material. The last equation obtained is the Lambert-Beer law. This law states that the number of photons exiting from the body is the number of emitted photons multiplied by the exponential. The main problem is that in the human body there is not just one type of tissue, but there are many different types, which form multiple layer that the photons beam has to pass through. Each one of those layers has a specific thickness and a specific attenuation coefficient. So the equation mentioned before must be corrected in this way:

$$N_0 = Ne^{-\sum \mu_i x_i}$$

μ_i and x_i represent respectively attenuation coefficients and thicknesses of each type of tissue. The only data available in a traditional radiography are the number of entering and exiting photons. This means that it is impossible to know in which order are disposed the tissues. The information about the third dimension disposition is lost. That is why computed tomography is used. The principle is simple: a narrow beam of x-rays is aimed at the patient then it rotates around him, performing multiple acquisitions. The rotation is usually from 0 to 180 degrees.The x-ray beams rotate on a ring called the gantry. After the the acquisitions are completed, a "slice" of the patient can be reconstructed with filtered retroprojection algorithms. Multiple slice allow the reconstruction of a 3D volume. The lesser is the distance between those slices, the more the volume reconstruction is precise. This 3D volume reconstruction allows the clinician to a spatial representation of the anatomical region of interest.
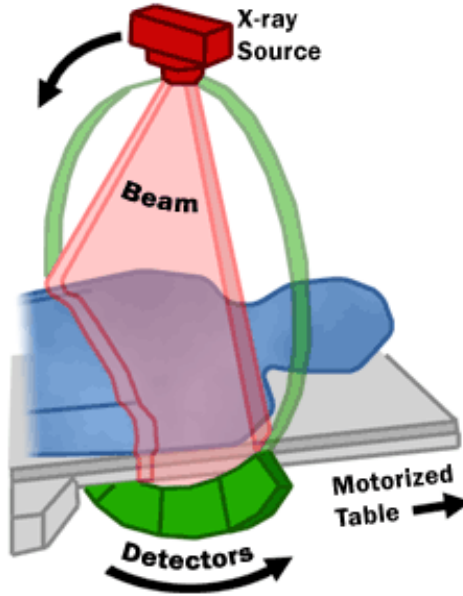
Figure 1.2: Representation of a standard tomograph. The x-ray tube rotates around the gantry, and manages to visualize the internal body of the patient from different perspectives. Image from the U.S. food and drug administration website[31]

A basic tomograph in terms of hardware is constituted by the following apparatuses:

- The x-ray tube: it emits the photons.

- The pre-patient collimator: a collimator is it is used to avoid the diffusion of the photons in

directions where the receptor would not see them. In this way a useless dose of photons to the patient is prevented.

- The post-patient collimator: his purpose is to have all the photons which arrive on the receptor to have a straight direction. Oblique and deviated photons are removed.

- The receptor, which can be formed by an array of sensors.

This particular conformation allows to have instead of a large beam which covers the whole body, multiple narrow x-ray beams which take a precise direction. On CT reconstructed volumes, the value of each voxel can be represented in Hounsfield units, which are calculated as follows[6][7]:

$$HU = 1000 \cdot \frac{\mu - \mu_w}{\mu_w}$$

Since there is a significant contrast between the lung tissue and the air, it is possible to use the HRCT (which is a CT with higher resolution, achieved with narrower x-ray beams) to see the internal morphology of the lungs. By looking at certain characteristics of the images, the clinician can diagnose certain pulmonary diseases. For instance, a healthy lung appears completely black on the tomography. Instead,in a patient having a fibrosis, some spots on the lungs may appear. Those spots appear due to the scarring of the tissue, and the more severe is the disease, the more numerous and intense the spots will be. On the other hand, in the case of emphysema, some honeycombing conformations will appear inside the lungs. Again, the more severe is the disease, the more numerous those conformations will be.

Substance	Hounsfield Units (HU)
Compact bone	1000(300:2500)
Liver	60(50:70)
Blood	55(50:60)
Kidneys	30(20:40)
Muscle	25(10:40)
Brain,grey matter	35(30:40)
Brain,white matter	25(20:30)
Water	0
Fat	-90(-100:-80)
Lung	-750(-950:-600)
Air	-1000

Table 1.1: Table taken from the "Diagnostic radiology physics"[6],here are reported the HU values for certain body' s tissues, as well as water and air. The values outside the parenthesis are the average ones, while the ones inside it indicate the range.

1.3.2 Spirometry

Some diseases can alter the volumes of air in the lungs, as well as the speed of entrance and exit of the air. One of the most used methods to assess those alterations in a quantitative manner is spirometry. A classic spirometer is formed by a calibrated bell filled with air inside a cylinder filled with water. This bell is connected to the patient thanks to a flexible tube. When the patient inhales, the bell goes down, when the patient exhales, the bell goes up. Through a system of pulleys, a pen writes on a rotating cylinder the variations of volume. There are four pulmonary volumes which do not overlap each other, while there are other volumes which are a combination of those four volumes. Those last volumes are called pulmonary capacities.
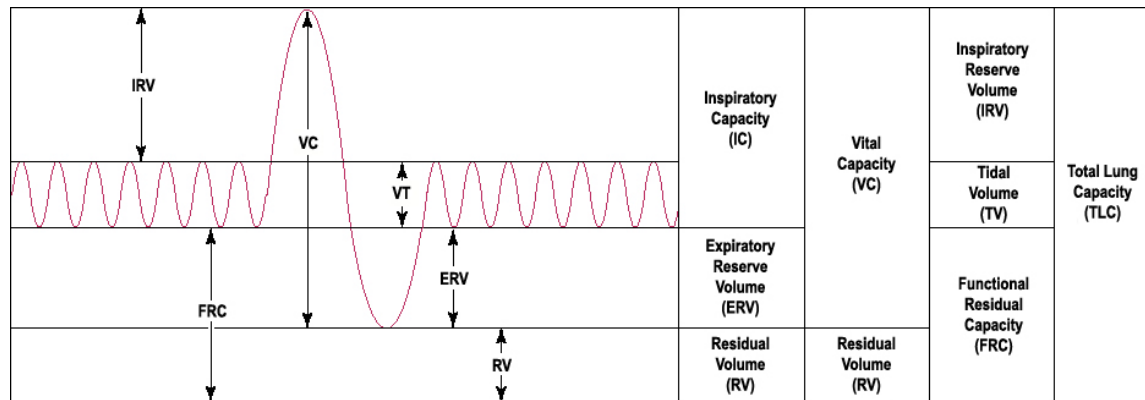
Figure 1.3: Graphycal representation of lung volumes and capacities. Image from wikipedia, the author of the image is the user Vihsadas[32]

- Tidal Volume (TV): it is the air volume in a regular (not forced) respiratory cycle. It is in average around 500 mL[2].

- Inspiratory reserve volume (IRV): it is the maximal air volume which can be inhaled after a regular inhalation. It is in average around 3000 mL[2].

- Expiratory reserve volume (ERV): it is the maximal air volume which can be exhaled after a regular exhalation. It is in average around 1000 mL[2].

- Residual volume (RV): it is the air volume remaining in the lung after a forced exhalation. Of the four regular volumes, it is the only one which can't be measured with spirometry. Helium diluition techniques are generally used to measure it. It is in average around 1200 mL[2].

- Inspiratory capacity (IC): it is the air volume which can be inhaled after a regular exhalation. It is in average around 3500 mL[2]. It is the combination of the tidal volume and the inspiratory reserve volume (IC=IRV+TV).

- Total lung capacity (TLC): it is the air volume present in the lungs after a forced inhalation. It is the combination of all the four main pulmonary volumes (TLC= TV+IRV+ERV+IC).It is in average around 5700 mL[2].

- Vital capacity (VC): It is the maximal air volume which can be exhaled after a forced inhalation. It is the combination of the tidal volume, the inspiratory reserve volume and and the expiratory reserve volume (CV=TV+IRV+ERC). It is in average around 4500 mL[2].

- Functional residual capacity (FRC): it is the air volume which remains in the lungs after a regular exhalation. It is the combination of the expiratory residual volume and of the residual volume (FRC=ERV+RV). It is in average around 2200 mL[2].

The calculation of volumes and capacities can help to do the distinction between obstructive and restrictive diseases. For example, in obstructive disorders, residual volume is often increased, because the patient has problems to inhale and exhale air. This means the lungs have often more air than necessary, which results in an increased TLC and FRC. In the other hand, restrictive disorders are often associated with decreased TLC and FRC because of the a minor pulmonary compliance.To diagnose pulmonary diseases, functional pulmonary tests with computed spirometry can also be executed. The most common measures for those tests are the forced vital capacity (FVC) and the forced expiratory volume in one second (FEV_1). FEV_1 is the ratio between the exhaled volume in one second and the FVC multiplied by 100[2]. During the test, the patient does a forced inhalation. Then, he exhales as much as he can and the faster possible. Thanks to the computer, it is possible to know the quantity of air exhaled in function of the time. A reduced FVC is a sign of restrictive disease. A regular FEV_1 is a value superior to 80 % . An inferior percentage indicates an obstructive disease.
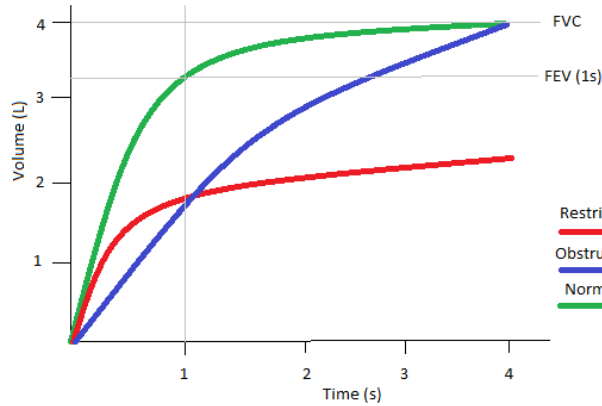
Figure 1.4: Representation of the expired volume as a function of time. It is possible to notice that normal condition and restrictive diseases the graphics have the same shape, but the one with restrictive diseases is compressed, which means that the maximal volume is reduced. The one with obstructive diseases instead presents a slower growth, indicating a reduced flux, typical of obstructive diseases.

Usually, the clinical data about those tests is plotted on a flux/volume graph. Restrictive and obstructive diseases both present a reduced flux peak if we confront it to healthy patients, although in the case of obstructive diseases this reduction is much more evident. Also, in restrictive diseases the volume is greatly reduced if confronted to healthy lungs or obstructive diseases.
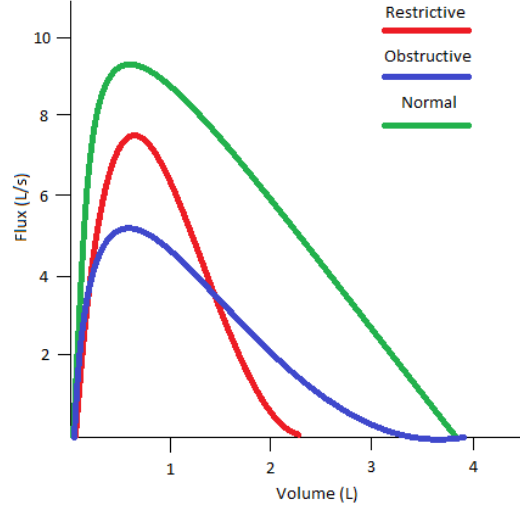
Figure 1.5: Qualitative representation of the flux-volume diagram in pulmonary diseases, in the horizontal axis the volume is represented in liters, while on the vertical axis the flux is represented in liters per seconds. It is possible to notice that in the case of an obstructive disease such ad emphysema, the flux is considerably reduced. In the case of a restrictive disease such as fibrosis, the volume and the flux are both reduced, although the flux is reduced in a lesser manner compared to the emphysema.

1.3.3   Diffusion lung capacity for carbon monoxide

Diffusion lung capacity for carbon monoxide (DLCO) is a test which permits to establish in a quantitative manner the capacity of lungs to exchange gas from the inspired air between alveoli and blood vessels[13]. This test is done with a spirometer,the patient breathes a blend constituted of air with a really low percentage of carbon monoxide (0,3%) and methane (0,3%). Carbon monoxide (CO) has a high affinity for hemoglobin (around 250 times the one of the oxygen), and it follows the same pathway as that of oxygen to finally bind with hemoglobin. In a typical test, the patient is asked to exhale until only the RV remains, then he must inhale until TLC is reached. After the inhalation he is asked to hold is breath for around ten seconds. Finally, the patient is asked to exhale as much as possible. The difference of concentration of CO inhaled and exhaled is in function of the lung efficiency to exchange gases. The higher the difference in concentration the more the lungs are efficient. The efficiency in the gas exchange depends from multiple factors. According to Fick's equation of gas diffusion[12]:

$$V_x = \frac{k \cdot A \cdot \Delta P}{\Delta X} \tag{1.1}$$

In the equation, V_x is the volume of gas transferred per unit time, k is the diffusion coefficient of the specific gas, A is the area of the surface for the gas exchange, ΔP is the partial pressure gradient from the two sides of the membrane, and ΔX is the membrane thickness. A reduced

11

DLCO is synonymous with decreased transfer volume. According to the equation above, a reduced transfer volume can be due to for example to a thicker membrane or a decreased exchange surface. The gravity of DLCO reduction can expressed in percentage doing the ratio between the measured DLCO and the predicted DLCO which is a theoretical value for an healthy person given certain characteristics (height, age, sex...). A percentage between 75% and 140% indicates a regular DLCO, a range between 60-75% indicates a mild reduction, a range between 40-60% a moderate reduction and a a value inferior to 40% indicates a severe reduction[14]. The DLCO can be expressed by the multiplication of two factors:

$$DLCO = V_a \cdot K_{CO} \tag{1.2}$$

V_a represents the number of contributing alveolar units measured by the tracer gas (methane or helium are the most common ones), and K_{CO}, which is often written as $DLCO/V_a$, represents the CO transfer coefficient which indicates the efficiency of CO transfer by alveoli. So, DLCO can be helpful in diagnosing the pulmonary diseases, like emphysema, where the walls of the air sacs are ruptured, thus the exchange surface is reduced. Those ruptured walls cause a decrease of both V_a and K_{CO}, and consequently a decrease of the DLCO. Also restrictive diseases can present a reduced DLCO, like fibrosis due to the thickening of the membrane[15].

1.3.4   Arterial blood gas test

Arterial blood gas (ABG) test is a commonly used diagnostic tool to help in the diagnosis of respiratory, metabolic and circulatory disorders[8]. This test is done by taking a sample of blood from the artery. Then, from the blood sample pH, partial oxygen arterial pressure (PaO_2), partial carbon dioxide arterial pressure ($PaCO_2$) are measured. Bicarbonate arterial concentration (HCO_3), arterial oxygen saturation (SaO_2) and base excess/deficit are calculated. A pH lower than the regular range (7,35-7,45)[9][10] and a $PaCO_2$ higher than the regular range (35-45 mmHg)[9][10], can be a sign of respiratory acidosis. Respiratory acidosis may be tied to obstructive lung diseases. On the other hand, a pH higher than the regular range and $PaCO_2$ lower than the regular range can be a sign of respiratory alkalosis. A possible origin of respiratory alkalosis can be hypoxia. This condition can be tied to lung diseases like pulmonary fibrosis[11]. So ABG is a complementary clinical test which can help the identification of pathological lung conditions.

1.4   Anatomy and physiology of inferior vena cava

The inferior vena cava transports deoxygenated blood from the lower half of the body (abdomen, lower limbs, pelvis...) to the right atrium. Compared to the arteries, the veins are thinner and are less resistant in the radial direction. This is because the veins are subjected to lesser pressure forces compared to the arteries. Also, the veins are more deformed compared to arteries in their longitudinal section. This deformation helps to avoid occlusions, which would be more likely to occur since the pressure in the veins is lower. Veins, like all blood vessels are constituted of three layers[2][29]:

- Tunica intima: The inner layer (tunica intima) is the thinnest layer, formed from a single continuous layer of endothelial cells and supported by a subendothelial layer of connective

tissue and supportive cells. The tunica intima is surrounded by a thin membrane comprised of elastic fibers running parallel to the vessel.

- Tunica media: surrounding the tunica intima is the tunica media, comprised of smooth muscle cells and elastic and connective tissues arranged circularly around the vessel. This layer is responsible for most of the mechanical properties of the blood vessels

- Tunica adventitia: the outermost layer is the tunica adventitia, composed entirely of connective fibers and surrounded by an external elastic lamina which functions to anchor vessels with surrounding tissues.

The inferior vena cava is subjected to variations of volume. Those variations depend from the variations of transmural pressure. The transmural pressure is the difference between the pressure inside the vessel and outside the vessel ($P_{tr} = P_{ext} - P_{int}$). It is possible to define the compliance of the inferior vena cava as the ratio between the variation of volume and the variation of transmural pressure ($C = \frac{\Delta V}{\Delta P_{tr}}$)[2]. The compliance is associated with the pulsatility of the inferior vena cava. This parameter can be helpful to have an estimation of different clinical conditions. For instance, it can be used to assess the volemic status[21][23] or to estimate the right atrial pressure[22].

1.5 Ultrasound imaging

1.5.1 Ultrasound physics

Ultrasound imaging is the most common medical imaging diagnostic exam used nowadays. This is probably due to a large number of interesting characteristics, like the non-ionizing nature of ultrasound waves, the low cost and portability of the ultrasound device, as well as a high temporal resolution, which permits to see in real time moving structures such as a beating heart, or blood vessels pulsing. The ultrasound imaging is based on acoustic waves having a frequency greater than the audible range by humans. In particular, ultrasounds have a frequency superior to 20 kHz, but generally in medical imaging the frequency range is of 1-15 MHz[6]. The selection of the frequency range depends on the clinical application. A fundamental law for ultrasound imaging is the relation between the speed of propagation, the wavelength and the frequency which is:

$$v = \lambda \cdot f$$

Where v is the velocity, f is the frequency and λ is the wavelength Ultrasound imaging is used for soft tissues, which have an average estimated propagation speed of 1540 $m \cdot s^{-1}$. If speed is fixed, an augmentation in frequency implies a lower wavelength. Having a lower wavelength permits the interaction with objects having reduced dimensions. This means that working with higher frequencies guarantees a higher spatial resolution. However, ultrasounds are mechanical waves which propagate through the tissues by successive cycles of compression and expansion of the molecules of those tissues. By travelling through the tissues, their mechanical energy is dissipated and converted into heat. So, if the acoustic wave is represented by a sine wave with an amplitude A_0, the wave after travelling for a certain distance z will have a reduced amplitude $A(z)$. This amplitude reduction follows a law of exponential type:

$$A(z) = A_0 \cdot e^{-\alpha z}$$

Here α represents the attenuation coefficient, which is a characteristic of each type of tissue. The higher is the attenuation coefficient, the faster the wave amplitude decreases, and if the the coefficient is too high, the wave is completely absorbed by the tissue before it can even be received. This coefficient is not fixed, but it varies with the frequency. More precisely, the higher is the frequency, the higher the attenuation coefficient will be and the more the amplitude of the wave will be reduced[16].This means that higher frequencies have an higher resolution, but can not penetrate deeply into the body. The consequence is that the frequency is generally chosen as a compromise between spatial resolution and penetration depth. An ultrasound image displays the absolute values of the ultrasound echoes. Those echoes are the partial reflection of the original wave and are due to the difference of acoustic impedance between two mediums, which in this case are the body's tissues. The acoustic impedance is the product between the density of the medium and the velocity of the ultrasound wave inside said medium:

$$Z = \rho \cdot v$$

Where Z is the acoustic impedance, ρ is the density of the medium and v is the velocity of propagation of the wave.

Material	Sound speed (m/s)	Acoustic impedance (MRayl)	Attenuation coefficient (dB/cm at 1 MHz)
Air	330	0,0004	12
Water	1480	1,48	0,0022
Fat	1450-1460	1,34-1,38	0,52
Liver	1555-1570	1,65	0,96
Blood	1550-1560	1,61-1,65	0,17
Muscle	1550-1600	1,62-1,71	1,2
Skull Bone	3360-4080	6,0-7,8	11,3

Table 1.2: From "Diagnostic radiology physics"[6], table with acoustic properties of different body's tissues, air and water.

Supposing we have two mediums, the first one with acoustic impedance Z_1 and the second one with acoustic impedance Z_2, at the interface between those two mediums there is a phenomenon similar to the one expressed by the Snell's law . This law states that if light passes through the interface of two different mediums, the ratio of the sines of the angles of incidence and refraction is equivalent to the ratio of velocities in the two media, or equivalent to the reciprocal of the ratio of the indices of refraction:

$$\frac{sin(\theta_i)}{sin(\theta_t)} = \frac{v_1}{v_2} = \frac{n_2}{n_1}$$

Where θ_i is the incidence angle, θ_t is the transmitted angle, v_1 is the velocity in the first medium, v_2 is the velocity in the second medium, n_1 is the refraction index in the first medium and n_2 is the refraction index of the second medium.
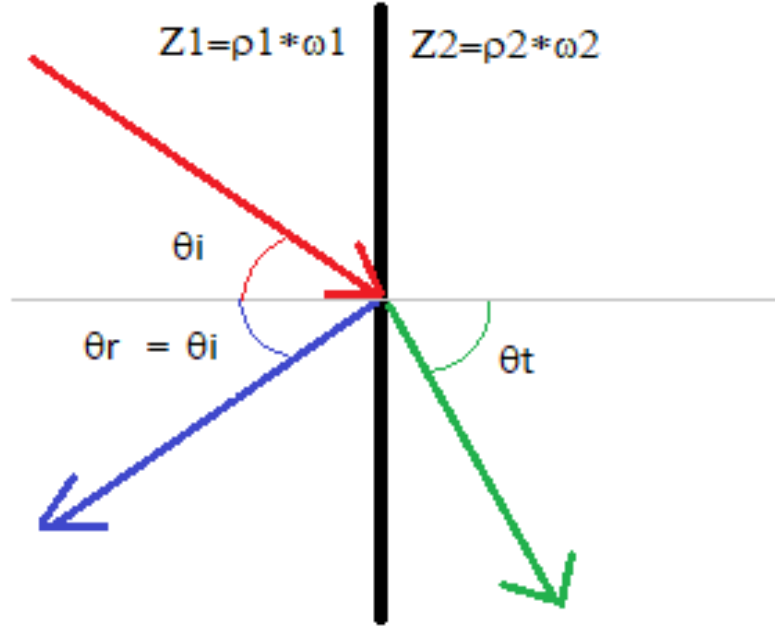
Figure 1.6: Angles of incidence, reflection and transmission at a planar interface between a material with sound speed $\omega 1$ and a second material with a higher sound speed $\omega 2$

Snell's law also states the a part of the light is reflected back, with a reflection angle identical to the incidence angle. The concept with ultrasounds is the same, but instead of the refraction index n there would be the impedance Z, and the light would be replaced by the ultrasound wave. To form an image, it must be known how much of the energy returns, and this can be done with the reflection coefficient.It is possible to express the reflection coefficient, which is the ratio between the energy of the reflected wave and the energy of the generated wave, with the following equation[18]:

$$R = \frac{E_r}{E_i} = \left[\frac{Z_2 cos(\theta_i) - Z_1 cos(\theta_t)}{Z_2 cos(\theta_i) + Z_1 cos(\theta_t)} \right]^2$$

Where E_r is the reflected energy, E_i is the energy of the incident (generated) wave . Generally, in ultrasonography it is considered that the incidence angle and the transmitted angle are both null, and since the cosine of a null angle is equal to one, the equation can be simplified:

$$R = \frac{E_r}{E_i} = \left[\frac{Z_2 - Z_1}{Z_2 + Z_1} \right]^2$$

Anything which is not reflected, it is transmitted, and the sum of the transmission coefficient and the reflection coefficient must be equal one thus we have the following relation:

15

$$T = 1 - R$$

Where the transmission coefficient is simply the reflection coefficient subtracted to one. Since an ultrasound image is directly dependent from the reflection coefficient, it is possible that two different medium interfaces produce the same reflection coefficient, and by consequence, the same image. This is why it is not possible to distinguish a type tissue simply by looking at tonality of grey on the image. The clinician requires an extensive formation to know exactly what is represented by an ultrasound image.

1.5.2 Ultrasound transducer

The ultrasound waves are generated and received by ultrasound transducers. It is the part of the machine which is held by the clinician. The transducer is composed by five main parts[17]:

- An element with piezoelectrical properties. It is an element where a deformation of his structure will generate a variation of potential between the two faces of the element (direct piezoelectric effect) and vice versa (indirect piezoelectric effect).To generate the ultrasound wave, it is used the indirect piezoelectric effect, while to receive it is used the direct effect. It can be a crystal like quartz, or a ceramic alloy like lead zirconate titanate (PZT), which is more and more common nowadays. To optimize the response of the element for a certain frequency, this one should have the thickness of $h = \frac{v}{2f}$ (v is the velocity of propagation and f is the frequency)

- Two electrodes, a positive one and a ground one. They are placed on each side of the piezoelectric element. They are used to generate the difference of potential necessary to have the piezoelectric effect.

- A damping block: is bonded to the back of the element to dampen the resonant vibrations in the element which creates a shorter spatial pulse length, allowing better spatial resolution. A typical backing material has been a type of epoxy resin with tungsten filaments.

- A matching layer: it tries to minimize the reflection of ultrasound waves between the piezoelectric element and the patient tissue. It is generally achieved by using a material which has an acoustic impedance between the ones of the piezoelectric element and the tissues. There can be multiple matching layers to allow a smoother transmission

- Insulation layers: there is the housing, made of plastic, which provides electrical insulation and protection to the element. Electric insulation is necessary both to shield the internal components from any outside electromagnetic interference and to prevent electric leakage from the element. There is also the acoustic insulator, which protects the element from external vibrations, which could cause differences of voltage inside the element.

Generally speaking, ultrasound transducers, or probes, have an array of 256 piezoelectric elements. Each one of those elements represents a scan line. For each one of those scan lines, ultrasound waves are generated in packets. After a packet is generated, the probe waits a certain time before sending another packet. During this time, the probe works as a receiver. So, the final image is a matrix where the columns are represented by the piezoelectric array, and the lines are

the number of time instants where the probe works as a receiver. This system is called pulsed-echo. There are three main probe types[19]:

- Linear type: all the piezoelectric elements are disposed in a linear array. The image has a rectangular form. Those probes can be used in vascular applications (ateriosclerosis, needle guididng..), in thyroid, breast, fat and muscle imaging, in musculoskeltal medicine (Tendon, Arthrosis) as well as intraoperative applications like laparoscopy.

- Convex type: the piezoelectric elements are disposed in a semi-circular shape. The image takes the form of a folding fan. The more the distance from the probe, the more the scan lines diverge. This means that for tissues which are located at a considerable depth, the spatial resolution is reduced. Those probes can be used for abdominal and prostate imaging as well as ostetric and ginecology applications.

- Sector or phased type: it is a particular type of probe. It has a rectangular base for the piezoelectrical array, but can emit an ultrasound beam with straigth scan lines, or deflected ones, depending on the needs of the clinician. The deflection can even be regulated in terms of quantity. This type of probe was created mostly for cardiac applications. In particular, there can be the need to see the movements of the heart in real time. Since the heart is covered by the rib cage, having a probe which can adapt depending on the anatomical conformation of the patient was necessary. This probe can also be used for abdominal and intraoperative applications.

1.5.3   Echographs

An echograph is a medical device used to generate and visualize anatomical images of the patients tissues. It is constituted of different blocks. The first block is the transducer, which was explained in detail in the precedent paragraph. This transducer, through a switch can be connected to the transmitter electronics or to a preamplifier. The transducer is connected to the transmitter electronics if the ultrasound are transmitted. The transmitter electronics apply the difference of potential to the transducer and in this way the ultrasound wave is generated. After the emission of the ultrasound packet, the switch trips, and the transducer is connected to the preamplier. In this case the transducer works as a receiver. The echoes hit the transducer, and the mechanical compression and decompression is converted in a difference of potential. This potential is amplified by the preamplifier, since the received wave is really attenuated compared to the emitted one. After the amplification, the analog signal is converted into a digital signal with an analog to digital converter (ADC). Then, the echo signals are beamformed and the time gain compensation (TGC) is applied. TCG is an amplification of the signal proportionate to how much time has passed between the transmission and the reception of an ultrasound wave. The more in depth the ultrasound travels, the more the echo will be attenuated, so the signal must be amplified to compensate this attenuation and to avoid that tissues which are further from the transducer will be visualized only in black. Then, the amplitude of the envelope is detected and logarithmic compression is applied. This type of compression is necessary to have a maximal variability in the gray scale of the image. Then, the scan conversion put each received signal into a map. This map is a matrix formed by values typically ranging from 0 to 255, and those values are bound to the amplitude of the signal received after all the processing. The lines of the matrix, as previously stated are the number of elements of the transducer, while the columns are the number of monitored time instants.Finally,

this matrix is visualized on a monitor, where 0 corresponds to black, while 255 corresponds to white. The intermediate values are the gray tonalities.
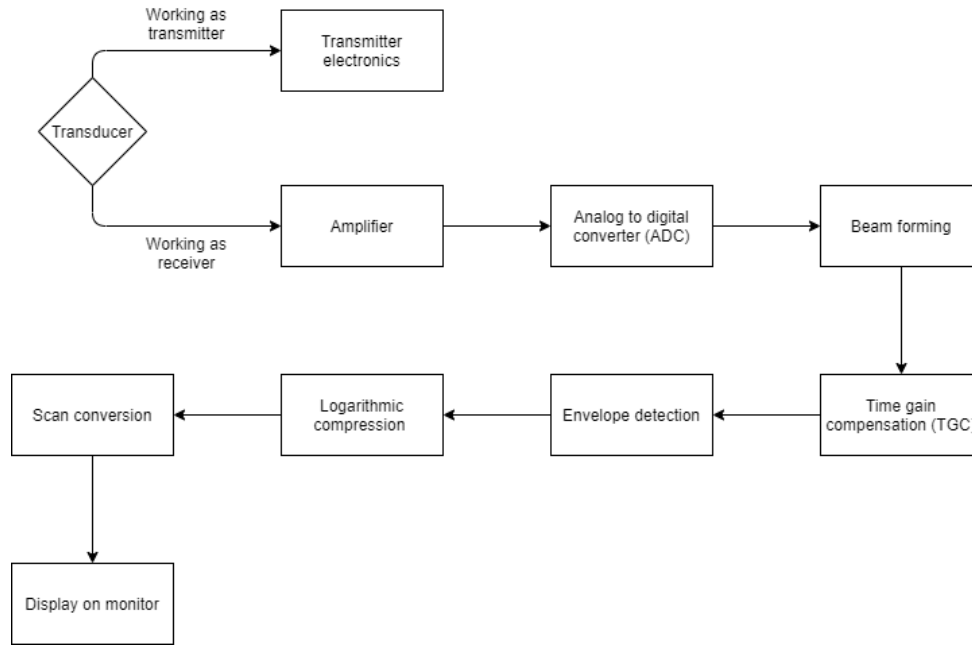
Figure 1.7: From "Diagnostic radiology physics"[6]. Block diagram of a B-mode ultrasound imaging system.

Three main strategies are adopted to visualize ultrasound images, although one of those three is less used nowadays:

- A-mode (amplitude): this strategy is not much used anymore. In this case there is a single scan line, and the image returned is just a graph, where one axis represents the depth and the other axis is the amplitude of the returned echo. The depth of the returned echo is identified by calculating the time which passes between the transmission and the return of the echo. With this mode, it is possible to know at which depth there is the interface between two tissues. So, by knowing the anatomy of the human body, the clinician can have an idea of the thickness of certain layers of tissue. Some of the main applications of this mode are ophthalmology, localization of brain midline, liver cirrhosis, myocardium infarction.

- B-mode (brightness): it form a two dimensional image. The shape depends on the type of probe. Each pixel of the image has a certain brightness depending on the amplitude of the returned echo the more the echo is ample, the more the pixel is bright.

- M-mode (motion): in this strategy, a single scan line is considered. In this case, the image is displayed again on a graph, but the vertical axis displays the depth of the received echo (the more bright the pixel, the more the echo was ample), while the horizontal axis displays the time. This visualization mode is commonly used to monitor the displacement of certain

18

tissues, like the myocardial walls or the walls of blood vessels like the inferior vena cava. Most of the time the acquisition of this image is synchronized with an electrocardiogram (ECG) so it is possible to see the displacement of said tissues in function of the systolic and diastolic phases of the heartbeat.

1.5.4 Doppler flowmetry

Having a general idea of the behavior of the blood flow within a vessel can be useful for clinicians. The doppler effect can be useful for this purpose. This effect is based on the principle that if a source emits an acoustic wave at certain frequency, and this source is mobile, an observer will perceive the acoustic wave with a shifted frequency. If the source is approaching the perceived frequency will be higher, vice versa if the source moving away, the perceived frequency will be lower. In this case, the sources would be the erythrocytes moving inside the blood vessels, which reflect the acoustic wave emitted by the transducer. The frequency shift is expressed by the following equation[6]:

$$f_d = \frac{2v f_0 cos(\theta_d)}{c}$$

Where v is the speed of the erythrocytes, f_0 is the frequency of the emitted wave, θ_d is the angle between the direction of motion of the erythrocytes and the scan line of the transducer, c is the propagation speed of ultrasounds inside the tissue (generally assumed 1540 m/s) and f_d is the frequency shift. If we want to estimate the flow, the speed of the erythrocytes must be calculated. The frequency of the emitted wave and the propagation speed are known terms. The frequency shift is measured. The only terms which can cause problems is the angle, which can not be estimated automatically.The angle must be estimated by the operator. Generally, the clinician is trained to position the transducer with an angle between 40°-60° compared to the line of motion of the blood. This is because with angles with those values, the error caused by a wrong measurement would still be linear. In this way, the speed of erythrocytes can be calculated simply by:

$$v = \frac{f_d \cdot c}{2 f_0 cos(\theta_d)}$$

Not all erythrocytes travel at the same speed. So, the power spectral density of the returning wave is calculated and the amplitude of different frequencies can provide an estimation of how many erythrocytes travel at a certain speed. There are two many modes for doppler flowmetry. The first one is the continuous wave doppler. In this case, the ultrasound wave is emitted constantly. There are two lines of piezoelectric elements: the first one is to emit and the second one is to receive. This configuration is more complex and has a greater economical cost. The main benefit is that by emitting a continuous wave, it is possible to follow the evolution of the blood flow at an higher frequency. The drawback is that by having a continuous wave emission, it is not possible to know how much time passes between the emission and reception of a specific wave. This leads to losing the information of how much in depth the echo formed. So, if for example there are two nearby vessels, it is impossible to know the blood speed of only one of them. The computed speed will be the average between the two of them. The pulsed wave doppler on the other hand, emits ultrasound waves in packets, like in classical echography. In this way, it is possible to know the speed of the erythrocytes in a precise vessel, although it is not possible to follow the evolution as precisely as

with a continuous wave doppler. Also, some medical devices allow the use of color doppler. In this case the monitor displays an ultrasound B-mode image, with superimposed a colormap. Two colors are allowed, blue and red. The red color shows a blood flow which approaches the transducer, while the blue shows a blood flow which gets away from the transducer. The more intense is the coloration, the more the module of the speed is higher.

1.5.5   Transthoracic echocardiography (TTE)

Transthoracic echocardiography is one of the most common clinical exams to assess the health of the heart[20]. With this exam it is possible to visualize all the four heart chambers (right and left atrium, right and left ventricle) and all four heart valves (pulmonary, aortic, mitral and tricuspid). It can also be used to visualize other structures in the proximity of the heart such as the aorta, the pericardium, pleural effusions, ascites, and inferior vena cava. The most common TTE use is the assessment of left ventricular function. This is generally requested when patients have symptoms of heart failure. It can also be used to see if heart murmurs are benign or are due to some anomalies, like valvular heart diseases. Additionally, other common uses can include the diagnose of mitral valve disease, mitral stenosis, atrial fibrillation and stroke. Since TTE can also visualize the inferior vena cava, it is possible to use the ultrasound images to study the pulsatility of the said vessel.

1.6   Methods to estimate the IVC pulsatility

1.6.1   Classical methods to study the pulsatility of the IVC

Pulsatility of the vena cava, as previously stated, can be a useful parameter in multiple clinical applications such as the estimation of the volemic status or the right atrial pressure. The caval index, also called collapsability index (CI), is often used in literature to study the pulsatility of the vena cava. It is the difference between the maximal diameter and the minimal diameter of the vein divided by the the maximal diameter[22][23][24]:

$$CI = \frac{D_{max} - D_{min}}{D_{max}}$$

In some cases the caval index is expressed in percentage. In those cases the previous equation is simply multiplied by 100 [21]. This index can prove to be challenging to estimate, this is firstly due to a lack of standardization on the measurements of the IVC diameters[25]. For instance, the diameter can be measured along the longitudinal or the transversal section, and in literature some authors use only one of the two types of measurements. This leads to a lower repeatability of the measures. Other factors which can influence the repeatability of the measures can be the experience of the operators (a more experienced echographer will obtain different results from a less experienced one, even on the same set of patients[25]), or the fact that depending on the clinician, the diameter of the vena cava can be measured from different portions of the said blood vessel. For example, the portion of the vena cava in proximity of the diaphragm has less pulsatility compared to more caudal ones. Furthermore, the pulsatility is influenced by two main different components, the respiratory and the cardiac one, thus leading to even more variability. A common approach to measure the diameter of the IVC along the longitudinal axis is to first use B-mode imaging to find the right orientation, then pass to M-mode to visualize the variations of the diameter of a

particular section of the IVC over time. The maximal and minimal diameters of the IVC are then measured along a respiratory cycle[21][25]. If more than one respiratory cycle is considered (which is often the case), the resulting CI is the average of the measured CI for each respiratory cycle. This standard approach however does not take into consideration that during the respiration cycle, the IVC undergoes three-dimensional displacements, which can include translations and rotations[25]. Considering this, it is not possible to say with certitude if the maximal diameter and the minimal one are measured from the same section of the IVC, factor which can influence the reliability of the results. Furthermore, not all the respiratory cycles are equal, thus leading to more variability in the measurement of the CI. Another standard approach is to measure the CI by taking the values of the diameter along the transverse section of the IVC. Those measurements can be influenced by all the factors mentioned before. Also, in the transverse section the CI is calculated by using the diameter only one direction of the blood vessel. This selected direction can vary depending on the experience of the clinician, but the diameter is not constant along all the direction, since the section of the IVC does not have a perfectly circular shape. This is further complicated by a different pulsatility along the multiple directions of the transverse section of the IVC. More in particular, a higher pulsatility along the directions in which the vein has a smaller extension has been noticed [24]. So, it is possible to say that the repeatability of the CI measures has some issues. Those issues can be partially solved by using semi-automated methods to estimate the CI of the IVC.

1.6.2 Semi-automated method on the longitudinal direction

A semi-automated approach is able to reduce the magnitude of the problems mentioned in the paragraph before. This approach consist in an algorithm able to track the borders of the IVC, and from the borders it is able to compute the caval index of multiple sections of said blood vessel[26]. First, a certain number of frames of the longitudinal section of the IVC are acquired. Then, the operator is asked to select, from the first frame, a rectangular portion of interest of the IVC. On this selected portion, the operator must select two reference points. Those reference points are assumed to be anchoring sites of the IVC. It is quite common that the left reference point is near the confluence between the hepatic vein and the IVC, while the right reference is near the lower hepatic region or at the confluence between the IVC and the portal vein.Between those two reference points, a segment is automatically traced. This segment will serve as reference to calculate displacements of the IVC in the following frames. The operator must then draw the two lines cutting the vessel transversally. Those lines limit the portion of interest of the IVC. Finally he must select two points, those two points must correspond to the leftmost higher and lower border of the IVC section of interest. After the initial user input, the algorithm automatically draws a defined number of lines between the two lines delimiting the portion of interest. Those lines are transversal to the vessel, and are uniformly distributed. Before identifying all the points corresponding to the border of the IVC, the frame is processed with a 9x9 pixels median filter. The operation of median filtering consist in sliding a window across the whole image, and the value of the central pixel of the window is replaced by the median of the pixels on the whole window. A window can have many shapes, in this case the shape was simply a rectangle. The median filter is generally used to reduce the image noise, and by doing so it helps the algorithm to identify features of interest in the image. Median filtering is especially effective against salt and pepper noise, where some pixels of the image can randomly take the maximal or minimal possible value (respectively 255 and 0 if it is an 8-bit image). The identification of the borders is done by detecting the points along the lines where

there are abrupt changes of intensity, since the interior part of the vein is usually black, while the borders have generally a higher intensity on the gray scale. However, more than one point along the line can have an abrupt change in intensity, so among the points where the intensity change is significant, only the ones which are closer to the points of the previous borders are selected. After the borders are estimated, for each line the border position is recalculated as the mean between its original value and the linear interpolation with its two nearest neighbours. This is an operation necessary to smooth the profile of the borders, and to compensate minor errors due to ultrasound artifacts. After the first frame is processed, the movements of the IVC borders are estimated. The estimation of movements is done by aligning in the 2-D fourier domain portions of two subsequent frames. Those image portions are 128x128 pixels windows both centered on the reference point of the first frame of the pair. From the third frame onward, the displacements are computed by using three frames instead of two, where the total displacement is the sum of the displacement between the first and the second frame and the displacement between the second and the third frame. The positions of the reference points are recalculated, and a new reference segment is traced. This new segment can be translated, rotated, stretched or compressed compared to the previous one. All the lines cutting transversely the IVC are then redrawn, and the borders of the vein are remapped. To further smooth the displacements of the borders between subsequent frames, positions of those borders in function of the time are low-pass filtered with a 4th order butterworth filter, having a cut-off frequency of 4 Hertz. A double filtering is applied, one filtering with time reversed, to avoid phase distortion and delay. Then, the the positions of each superior and inferior border are averaged . Those obtained points are the interpolated with a 4th order polynomial function, and in this way the midline of the IVC is computed. From the midline a defined number of equidistant points are selected, from those points lines perpendicular to the section of the IVC are computed. Then, the intersections between those lines and the segment uniting the two closest border points to the line are identified as the points which represent the two extremes of the IVC sections of interest. Caval index can finally be calculated for each section with the equation mentioned above, and a global caval index is established as the average of all the caval indexes. This semi-automated method permits to have the caval index of multiple sections of the vein, and to have an higher repeatability of the results by averaging them, thus addressing the lack of standardization about which section of the vein the clinician should measure. This method also partially solves the issue about the variability depending from the operators, as a study demonstrated that the automated method provides more homogeneous measures than the manual one , with the same set of patients [25]. Finally, with this method it is possible to separate the cardiac and the respiratory components of the IVC pulsatility. This point is treated in a later paragraph.

1.6.3   Semi-automated method on the transversal direction

A semi-automated method to evaluate the pulsatility along the transverse plane of the IVC has been proposed in literature[24]. This method can be helpful to better understand how the pulsatility is different among different directions of the blood vessel. As in the case of the longitudinal algorithm, a certain number of frames of the IVC must be recorded by using B-mode. After the recording, the dimension of a single pixel of the image is identified by comparing it to the scale present on the ultrasound image. Then, the operator is asked to select in the first frame the center of the IVC. A rectangular window centered in the pixel selected by the user, and said window includes the whole transverse view of the IVC. All the following frames share the same window of the first frame. Each frame is then converted from RGB to gray scale, and the contrast of those image is enhanced

through histogram equalization. The luminosity histogram is a graph where in the horizontal axis there are all the possible values for the pixels intensity (from 0 to 255 on 8 bit images), while on the vertical axe there are the number of pixels which have the intensity corresponding to a certain value. An image with a low contrast, will have most of the pixels with similar values, and so a peak on the graph will be formed. By equalizing the histogram, each value of intensity theoretically has the same amount of pixels, thus enhancing the contrast. After the contrast enhancement,the image was smoothed by using an 11x11 pixels median filter. Then, twenty equidistant rays , each one going in a different direction, are traced from the center of the vein. For the first frame, the entirety of each ray is analyzed, and the intensity of the pixels along each one of them is estimated by sampling 100 points by cubic interpolation. Since the internal part of the vein is black, and the external part is brighter, the points corresponding to the borders are identified where there is the most abrupt change in intensity. This change in intensity is identified by minimizing the mean root squared error between the function with the estimated intensity and a step function, which is the idealization of the change of intensity. On the frames subsequent the first, only the ten points before and after the borders of the previous frame are considered to find the new location of the borders. To achieve a smooth profile of the twenty points delimiting the borders of the vein, their position along the vertical and horizontal axis were filtered at a cut-off frequency of 0.3 Hz, with a 4th order butterworth filter. Also, between two frames the maximum displacement is assumed to be of five pixel. This means that if a variation of position was greater than five pixels, it was not considered. Instead, the position was substituted by the value of the quadratic interpolation of the four closer points. After all the frames are processed, the area for each one of the frames can be calculated by summing the areas of the 20 sections delimited by the pairs of rays. In this way it is obtained a time series, which is filtered with a 4th order butterworth filter with a cut-off frequency of 4 Hz. Finally, the diameter in each frame was calculated with the following formula:

$$D = 2\sqrt{\frac{A}{\pi}}.$$

Where D is the diameter and A is the area. From the diameter, the caval index can be computed. It is also possible to estimate the caval index along different portions of the IVC section, by calculating the diameter along different directions. It has been noted that the caval indexe along each direction can vary of a considerable margin, and it is generally greater along the direction in which the vein is less extended[24]. With this method, it is possible to partially solve the issue of the repeatability of the results, since the global caval index is calculated indirectly from the area of the vein, instead of just from the diameter along a single direction. It also gives the possibility to the user to evaluate the caval index along different directions, if it is necessary. So, this semi-automated method is more versatile than the standard one, and has been used clinically to estimate the volemic status of some patients[23].

1.6.4 Estimation of cardiac and respiratory components of the IVC pulsatility

With both the semi-automated methods, it is possible to estimate the cardiac and the respiratory components in the caval index. Once the time series of the dimension of the IVC's diameter is obtained, the respiratory caval index (RCI) and the cardiac caval index (CCI) can be extracted simply by filtering. More specifically, the cardiac component can be obtained by using an high pass

filter with a cut-off frequency of 0,8 Hz in some studies[22][23][25], or with a cut-off frequency of 0,4 Hz in others[24]. This frequency was chosen since the heartbeat is around 60 b.p.m. (1 Hz), so cutting below this frequency guaranties a certain margin of error. The respiratory component is instead extracted by filtering the time series with a low pass filter with a cut-off frequency of 0,4 Hz. After the extraction of the two components, both CCI and RCI can be calculated simply by using the regular equation of the caval index on the two filtered time series. In normal conditions, respiration is a slow process compared to the heartbeat, generally an healthy person in resting conditions breathes around twelve times in a minute, so the average frequency would be of 0,2 Hz. Globally, it has been noted that the respiratory component presents larger oscillations[22][23][24][25] compared to cardiac component of the caval index. Also, the RCI is much more variable compared to the CCI. This is mostly due to the fact that heartbeats, if there are not cardiac arhythmias, are more regular than respiratory cycles, since those last ones can be partially controlled by the person, while the heartbeats can not. Also it is possible to compute the CCI and the RCI on a singular direction for the view on the transversal plane, and on singular section of the longitudinal view of the IVC. It is possible to conclude that the separating the cardiac and the respiratory components can be done with both the views of the IVC, and that the procedure, once obtained the global time series, is quite simple.

1.6.5 Applications of the algorithms in the assessment of the right atrial pressure (RAP)

The right atrial pressure (RAP), reflects the venous return to the heart, which is the flow of blood returning to the heart. This parameter can be useful in clinical applications such as the treatment and prognosis of cardiovascular and respiratory diseases[28]. The assessment of RAP can be done by catheterization. It is the most precise procedure, but it also presents the constraint of being invasive. There is not a standardized procedure to measure the RAP in a non invasive way. However, the IVC pulsatility, along with other anthropometric characteristics of a patient have been used to build a model to estimate the RAP[22]. More specifically, in the study mentioned, the caval index was calculated both manually and with the algorithm operating on the longitudinal section. Also, RCI and CCI were computed through the algorithm. It has been noticed that the caval index is inversely correlated to the RAP, so instead of directly using the various caval indexes as features, a formula having the following form for each one of them was used:

$$\frac{1}{\alpha + ACI}$$

In the formula above, ACI can represent any type of caval index (manual,automated, respiratory, cardiac), and α is a positive number to better adjust the model and to avoid having zero at the denominator. Other parameters from the ultrasound imaging were extracted, such as the mean diameter of the IVC, both manually and with the algorithm. Also, five parameters not extracted from the ultrasound scans were used: age, sex, height, weight and body surface area. For all those features, it was calculated the correlation with the RAP, and the features extracted with the algorithm presented an higher correlation than those extracted manually. For instance, the mean diameter, which is the feature having the highest correlation, if estimated manually it had 56,7% of correlation, while if computed with the algorithm, it presented a correlation of 64,6%. The regression functions to estimate the RAP were built by considering all the possible combinations of

24

single features, doubles and triplets. The performances of the models were evaluated by considering the mean of the absolute value of the errors: $E = |x_r - x_r|$ were x_r is the RAP estimated with the regression model and x_m is the measured RAP. The best model with the manual approach was:

$$RAP_{manual} = 0,55 \cdot D_{mmanual}$$

This model includes only one feature, the mean diameter obtained manually, and has an average error of 4,04 mmHg and a correlation of 53,9%.

The best model with the semi-automated approach was:

$$RAP_{auto} = 0,52 \cdot D_{mauto} + \frac{4,13}{2,4 + CI_{auto}}$$

In this case the model included two features, the mean diameter obtained with the algorithm and the feature obtained by using the CI from the algorithm. This model presents an average error of 3,64 mmHg and a correlation of 61,6%. So, correlation was higher and error was lower for the semi-automated method compared to the manual one, meaning that the algorithm can be valuable for the RAP estimation.

1.6.6 Applications of the algorithms for the assessment of the volemic status

The assessment of the volemic status is useful to correctly treat patients in the patients in various departments such as cardiology, internal medicine and emergency. The IVC pulsatility can be used to evaluate the volemic status non invasively. A study was made to build a classifier to distinguish between euvolemic, hypovolemic and hypervolemic patients[23]. For this study, all the features necessary to build the classifier were extracted from the ultrasound scans. The scans of the IVC were taken both longitudinally and transversally. More specifically, the features from the manual approach were the diameter of the IVC and the CI in both the long and the short axis. The features using the two algorithms were: the mean diameter of the IVC, CI, RCI and the CCI in both the longitudinal and transverse axis. Various techniques were employed to build different models, but the one leading to the best results, both for manual and semi-automated approach was a binary tree model(BTM). Two BTM were finally selected, among the ones who led better results, one with only manual parameters, and the other with only semi-automated parameters. The BTM with semi automated parameters presented 90% of positive predictive value, 94,2% in negative predictive value, 95% in mean specificity, 90% in mean sensitivity and 92,9% in mean accuracy. The BTM with manual parameters presented 86,2% of positive predictive value, 91,8% in negative predictive value, 91,9% in mean specificity, 86% in mean sensitivity and 89,8% in mean accuracy. Those performances were obtained by using the entire dataset of patients to train the model. There was also a training using a leave-one-out approach. A leave one out cross validation is generally used when the dataset is not much large. In this particular approach, all the patients except one are used as training set, then the model is tested on the patient remaining. Then, another patient is left out, and the training set is again composed of the remaining patients. This procedure is repeated until all the patients have been part of the test set. Using this approach, the results were the following: 70% mean sensitivity using the the semi-automated approach, 66% using the manual one; 83,2% mean specificity using the the semi-automated approach,80,4 % using the manual one;

70% positive predictive value using the the semi-automated approach, 65,1% using the manual one; 82,1% negative predictive value using the the semi-automated approach, 80,5% using the manual one; 78% mean accuracy using the the semi-automated approach, 75,3% using the manual one. It is noticeable that the model built with the semi-automated parameters has a better performance than the model built with manual parameters. So, it is possible to say that the pulsatility of the IVC presents a multitude of relevant clinical applications, and using the semi-automated algorithms can be helpful to have more precise measurements. Of course, it is always necessary a post processing of the obtained data to have a clinical application.

Chapter 2

Material and methods

2.1 Introduction to speckle tracking

Speckle tracking is a common method used in echocardiography to follow the motion of the myocardial tissue[33]. The final application is generally to estimate the strain of said tissue. A speckle pattern is a granular appearance in the image. This granular appearance is due to the backscattering of the waves generated by the source. Each object which interacts with those waves acts as scatterer and becomes a secondary source of waves, which will have different phases and amplitudes. Those backscattered waves will thus generate a the speckle pattern. While it can be often detrimental to have an image composed only by speckles, since it can be sometimes hard for the physician to formulate a diagnosis, having a speckle pattern can also be seen as having an "imprint" which can result useful in the tracking of tissue motion. To track the motion of the tissue, the similarity between two portions of the images can be evaluated. To evaluate this similarity, it is generally used a block matching algorithm[34]. An other application where this technique can be used is the particle image velocimetry (PIV)[35]. Particle image velocimetry is quite often used to estimate the flow inside a certain object. Inside it, a liquid with little particles is made it flow. Images of the movements of those particle are taken with a camera, and then with the block-matching algorithm it is possible to estimate displacement and velocities of certain groups of particles, thus obtaining a map of the flow. Some general rules to apply the speckle tracking in echocardiography are the following: the acquisition frame rate must be at least 40 fps[36], the echography must be of good quality, the noise which is always present must be stable from one frame to another and finally the movements of the tissue visualized must not be too abrupt.

2.2 Block matching Algorithm

The block matching algorithm could be defined as the core of the speckle tracking. It is a way to estimate the similarity between two portions of different images. In tracking applications, the block matching algorithm is generally applied between two subsequent frames. In the first frame, the pixel of which it is wanted the tracking is centered on block which is generally defined as "template"[34].Then, the template is moved through another block on the second frame, this block is generally larger than the template and is defined as search area. Then, location of the centered pixel of the template can be found with the best match between the template and the portion of the search area on which it is the template. There are several methods to find the best match between those two blocks. The first one is computationally the less intensive, but is also the less precise one. It is the sum of absolute differences (SAD):

$$\sum_{dx=-w}^{w} \sum_{dy=-w}^{w} |T(x+dx, y+dy) - SA(x+u+dx, y+v+dy)|$$

Here T indicates the template and SA the search area. The letters x and y represent the coordinates of the point of which the displacement must be calculated, dx and dy represent the pixels around the point of interest. In this case those pixels form a (2w+1)x(2w+1) template. Instead u and v represent the shift of the search area compared to the template. In this case, the template slides all across the search area and each time it is shifted, all absolute values of the differences of the intensities between the corresponding pixels are calculated, then they are summed. The best match is found as the point of the search area where this sum is at the minimum. This

is the simplest and fastest method to gauge the similarity between two images, but it is also less precise compared to the other ones. A method which is more precise but also more computationally intensive can be the mean square error (MSE). The formula is the following:

$$\frac{1}{(2w+1)^2} \sum_{dx=-w}^{w} \sum_{dy=-w}^{w} [T(x+dx, y+dy) - SA(x+u+dx, y+v+dy)]^2$$

In the case of the mean squared errors, the procedure is similar to the sum of absolute differences, but there is there is a division for the total number of pixels. The best match in this case is also found in the minimum location. Finally there is a third method, the normalized cross correlation (NCC) which is often considered the gold standard to match two similar image portions[34]:

$$\frac{\sum_{dx=-w}^{w} \sum_{dy=-w}^{w} [T(x+dx, y+dy) - \overline{T}][SA(x+u+dx, y+v+dy) - \overline{SA}]}{\sqrt{\sum_{dx=-w}^{w} \sum_{dy=-w}^{w} [T(x+dx, y+dy) - \overline{T}]^2 \sum_{dx=-w}^{w} \sum_{dy=-w}^{w} [SA(x+u+dx, y+v+dy) - \overline{SA}]^2}}$$

Here the $\overline{T}$ and $\overline{SA}$ represent respectively the mean of the template and the local mean of the search area, corresponding to the zone on which the template is passed. This means that the local mean of the search area must be recalculated each time the template is shifted across it, which contributes to the computational weight of the normalized cross correlation. Also, there are three summations to compute instead of one, further enhancing the time needed to calculate the normalized cross correlation. On the other hand this method is the most stable of the three and for this master thesis is the one which has been used to write the algorithm. In this case of the new location of the pixel is found on the location of the maximum of the normalized cross correlation.

2.3 Methods of stabilization

Most of the time, simply using a block matching algorithm is not enough to correctly track the motion of certain points. The first problem can be that the pixel resolution is insufficient. The maximum found with normalized cross correlation it is not necessarily the true one, since the resolution is only of one pixel.The true maximum could be shifted around the one found. To solve this problem, it is required a sub-pixel resolution, and to achieve it, it is generally applied a peak fitting. This peak fitting is done on a 3x3 window where the center of this window is the maximum of the normalized cross correlation, and the other points are the ones around it. It is possible to use an interpolation such as the cubic one on this window to find the location of the true maximum. The resolution can be regulated by doing the interpolation with different number of points. The more points has the interpolation, the better is the resolution, but the computation becomes more intensive.

Another problem which is usually present in speckle tracking is that some of the points have anomalous displacements. In this case, it is possible to remove the outliers by applying some filters on the calculated displacements, or it is possible to use some other techniques such as edge detection or shape functions to adjust the displacements towards an expected geometry[37].
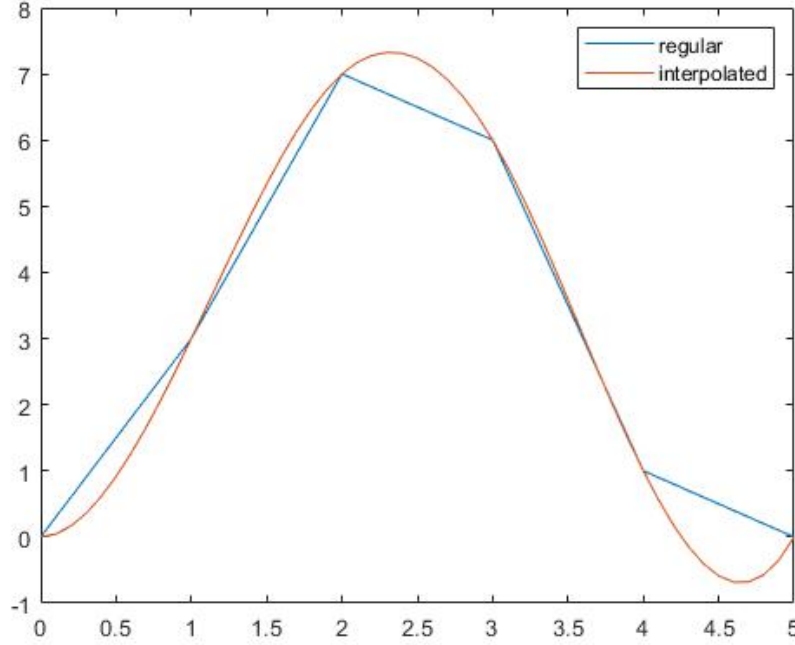
29

Figure 2.1: 2D representation of peak without interpolation and peak with interpolation: it is possible to see that after the interpolation the maximum is shifted. The same would apply on a 3D representation.

2.4 Proposed algorithm for the longitudinal section

As previously mentioned, speckle tracking in echography is generally used to evaluate the myocardial strain. So, an algorithm specifically designed to track the movements of the borders of the vena cava had to be written. The proposed algorithm has been written in Matlab, and the way it works is described in this section. First, the user is asked to select some points on the upper and on the lower border of the vena cava, those points should trace the portion of interest of the vessel and will form two different curves (one for the upper border and one for the lower border). From those curves, twenty-one equidistant points on each curve are calculated, those will be the points to track for the algorithm. In this way the user is not required to selected the points in a perfect manner, it is sufficient that the placed points give an idea of the general shape of the borders of the vessel. This recalculation to obtain twenty-one equidistant points on each border is done with the function curvspace.m present on the Matlab file exchange[38]. With this function the points are evenly spaced by using the euclidean distance.The use of euclidean distance has been accepted because the shape of the borders on the longitudinal section is not extremely complex.

After this initialisation, each of the selected points is centered in a template with a size of 31x31 pixels. So, the template is a matrix with the values of the pixel intensities of the first frame which are located around the pixel of which the displacement must be followed. Also, the selected points
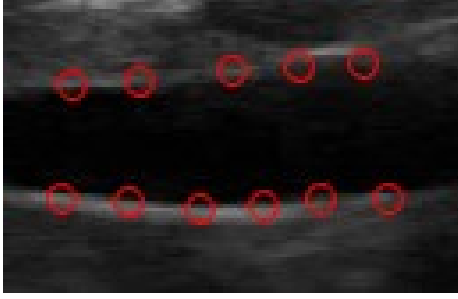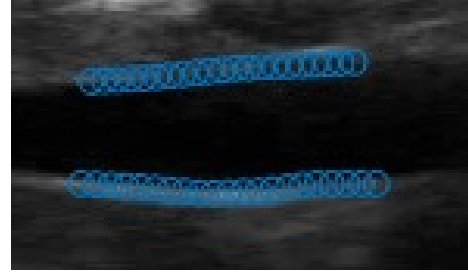
Figure 2.2: Border points selected manually

Figure 2.3: Border points recalculated with curvspace.m

are centered in a search area with a size of 51x51 pixels. In this case, the search area is a matrix with the values of the pixel intensities of the second frame which are located around the pixel of which the displacement must be followed. After the template and the search area are defined, the normalized cross-correlation between the template and the search area is computed with the lewis cross correlation in the spatial domain[41], the written code is a 2d adaption of the one written by Artan Kaso[42]. The results are numerically identical to the Matlab function normxcorr2, except that the zero padding is not done. Then, the new location of the center pixel of the template is found in the second frame by locating the maximum peak of the normalized cross correlation. By simply using this method, the resolution for calculating the displacement would be of just one pixel. To further enhance the resolution, a 3x3 matrix centered in the maximum peak of the normalized cross correlation is interpolated in the two dimensions with the function interp2. The method used for the interpolation is the cubic one, and after the cubic interpolation a 21x21 matrix is obtained, thus achieving a resolution of 0.05 pixels. On the interpolated matrix the new maximum peak is found, and so displacement of the pixel is calculated as the sum between the displacement found with the cross-correlation, and the shift of the maximum peak found with the 2D interpolation. The displacements are then filtered to remove possible outliers. It is used a median filter for the purpose, with the matlab function medfilt1. For the displacements on the horizontal axis, the filter is of order 11, and the displacements of all the points are filtered together. For the displacements on the vertical axis the filter is of order 7, and the displacements of the upper and lower border of the inferior vena cava are filtered separately. This separation is necessary because the upper and lower border of the vena cava often move in two opposite direction, due to the compression and dilation phenomenons of the vessel. For both the horizontal and the vertical axis the filter applied had a decreasing window the closer it was to the ends of the vector containing the displacements, this was done by using the option 'truncate' in the Matlab function medfilt1. A problem noticed is that sometimes the tracking of certain points can be lost. Most of the time, the points of which the tracking is lost end up in the center of the vein. So after that the new positions of the points are found, the difference between the intensity of the pixel above and the pixel below the new position is computed. If this difference is equal to zero, it would mean that the new position found can not be on the border of the vein. This because the internal zone of the vein, where the blood flows, is black on the echography, while the tissue is white, so if a point is situated on the border of the vein, the difference before mentioned should be substantial. The difference is only calculated along the vertical axis since the tracking of the points is lost much more often along this direction, due to the

31

more abrupt movements. So, if the difference is equal to zero, in an 11x3 window where the center of it is the newfound position, a sobel filter is applied. The operation of sobel filtering is simply a convolution between the area of interest and the following matrix: $\begin{bmatrix} 1 & 2 & 1 \\ 0 & 0 & 0 \\ -1 & -2 & -1 \end{bmatrix}$

Then, the location of the maximum gradient is identified, and the resolution is enhanced with a technique analogous to the one for the peak of the normalized cross correlation. The points are then displaced on the area with the maximum gradient after the resolution has been enhanced. It should be noted that the operation on the gradient is done only for the points on the upper border of the vessel, since the points are generally lost here, probably because the displacements are more intense in this area.
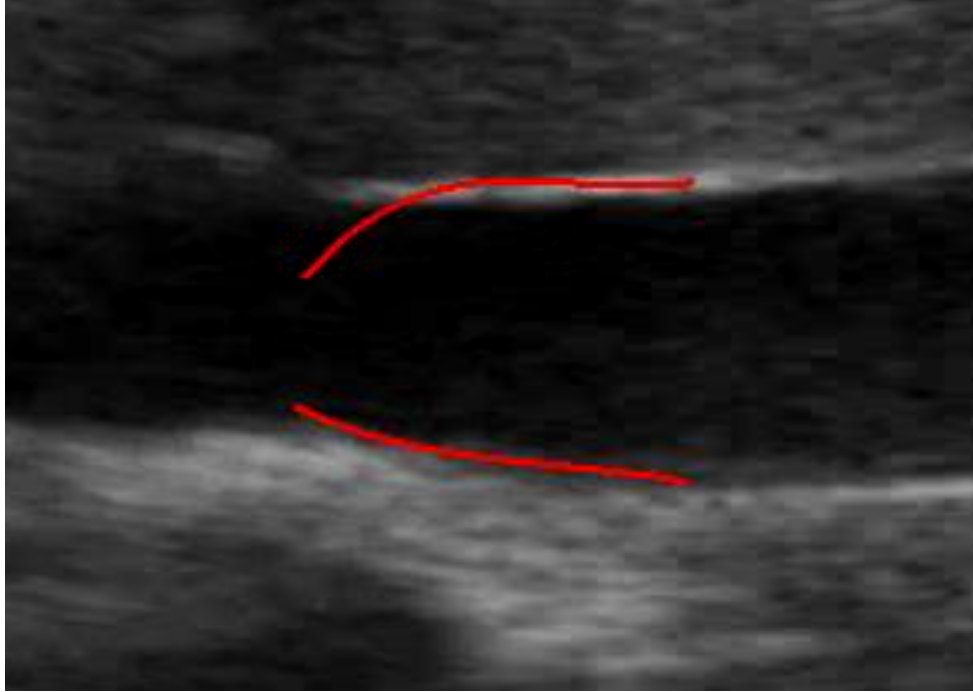

Figure 2.4: Example of some points ending up inside the vein

This procedure between two subsequent frames is then iterated for the whole video. Despite the adjustments made to stabilize the tracking, on the long run some points can still be lost. So, each N frames, the actual frame is realigned to the points of the first frame (by using the same procedure explained above) which were traced manually. N is a parameter selectable by the user, and generally varies between 20 and 30. This procedure can although be a double edged sword since there can be a decorrelation between frames[37], and the displacements could be so great that the dimensions of the search area could be insufficient to follow them, which could lead to an incorrect realignment. For those issues, the search area and the template dimensions are greater when the realignment to the first frame is done. The template in this case is a 61x61 matrix while the search area is a 81x81 matrix. The usage of the sobel filter previously explained greatly help to mitigate

the effects of misplaced points. Also, to further avoid problems due to misplacements, the positions of the points after the realignment with first frame are averaged with the positions that would have those points if there was an alignment between two subsequent frames. Also, after the positions are recalculated, the points of the upper and lower border are separately fitted to two polynomial curves of order 4, and 21 new equidistant points are taken on those curves as the new positions. It must be noted that the realignment between the current frame and the first one is computationally more intensive than calculating the displacement between two subsequent frames, and as such it is used rarely.

2.5   Calculation of the diameters

After that the points representing the borders of the inferior vena cava were found for all frames, calculating the diameters of the various sections of the vessels was necessary. For this purpose, a specific matlab code had been written. First, the points of the upper and lower borders are fitted separately to a 4th degree polynomial function. The the midline of those two curves is calculated, simply by summing the position of the points constituting the curves of the upper and lower borders, and then dividing by two. Then, 15 perpendicular straight lines to the midline passing through 15 equidistant placed on the midline were traced. Then the intersection between those straight line and the upper curve are calculated with the matlab function polyxpoly. The same is done for the lower curve. Finally the diameters are calculated as the euclidean distance between two of the intersections mentioned before placed on the same straight line.

2.6   Calculation of the Caval index

After that diameters were calculated, the caval index has to be estimated. Since the viper algorithm works in a different manner from the one developed in this thesis, a specific code to estimate the caval index had to be written. First, the dimensions of the diameters are filtered with a butterworth lowpass filter of order 4, with a cutoff frequency of 4 Hz. The filtering was done in two directions to avoid phase distortion, by using the matlab function filtfilt. This filtering was done to eliminate high frequency components which are not correlated with physiological movements. Then, the diameters were filtered again to extract the respiratory components of the diameters, this with a butterworth lowpass filter of order 4 with a cutoff frequency of 0.4 Hz.To calculate the cardiac component, the respiratory component is simply subtracted from the diameters obtained with the first filter. After that the respiratory and the cardiac components were extracted, it was used the matlab function findpeaks to find the local maximums and the local minimums of the respiratory component (to find the local minimums, the signal multiplied by -1 was simply passed through the function mentioned before). Then local maximums and minimums were interpolated separately, by using the matlab function interp1, with the method 'makima'. Finally, the midline between the two interpolations can be calculated. This midline would represent the trend of the respiratory component along time. This trend was subtracted from the cardiac and respiratory components as well as from the first filtered diameters, since it could hide some peaks of interest. Then, the function findpeaks is used again on the detrended cardiac, respiratory and filtered diameters. An interpolation of the local minimum and local maximum is done again with an analogous procedure to the one used for the detrending. After that, to each interpolation is summed the trend. In this way, it is possible to have various continuous functions representing the maximum and minimum diameters
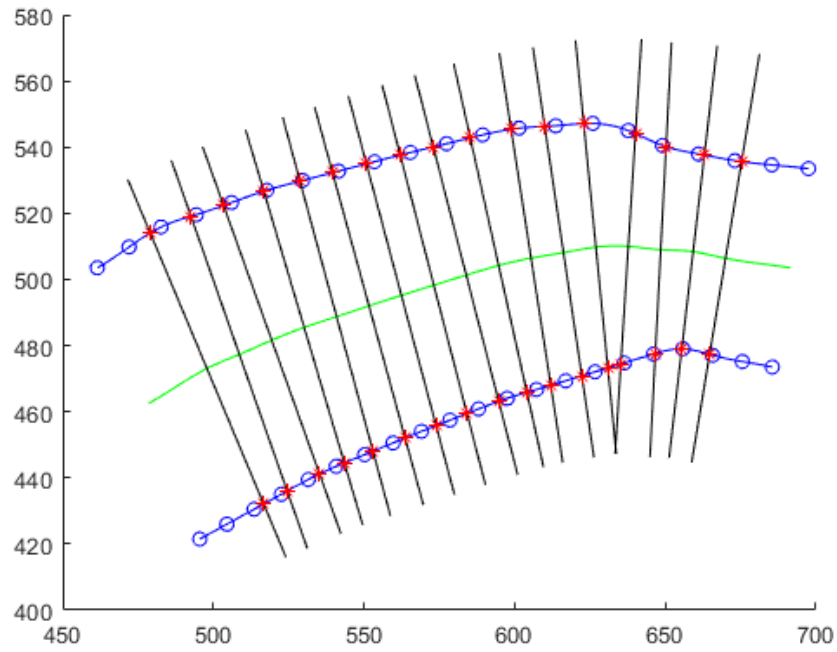
Figure 2.5: Example of the diameters calculation. The red asterisks are the intersections between the lines and the curves.

for the cardiac, respiratory and general components. Finally, the caval index, the respiratory caval index and the cardiac caval index can be calculated by subtracting from the function representing the corresponding maximum the function representing the corresponding minimum, and then by dividing all by the corresponding maximum.
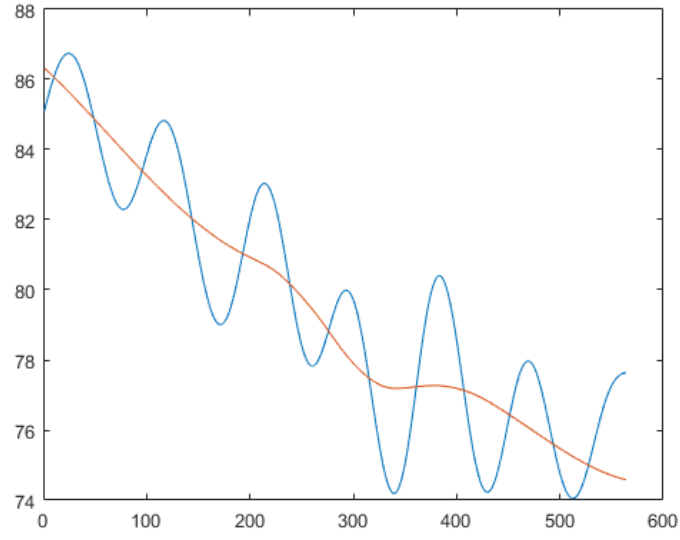
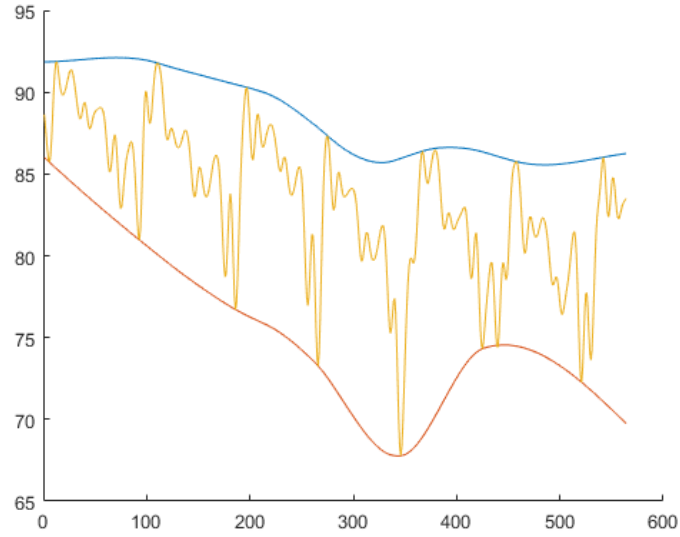Figure 2.6: Example of respiratory component with calculated trend

Figure 2.7: Example of general diameters (size in pixels) with local maximum and minimum interpolations. Those interpolations are used to calculate the global caval index.
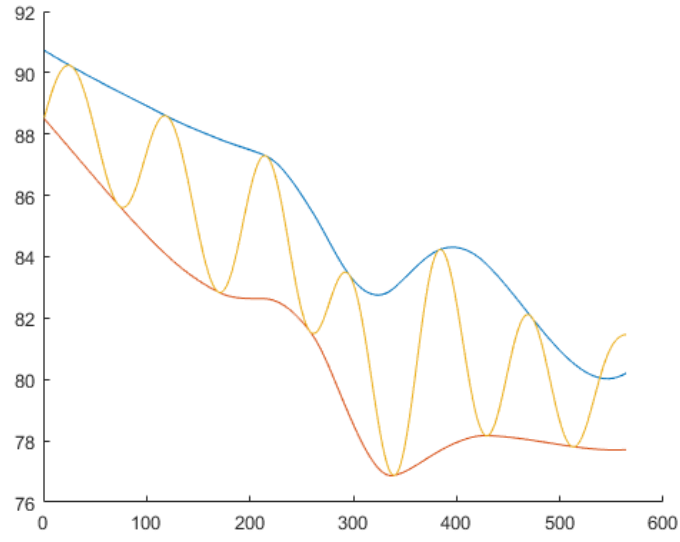
Figure 2.8: Example of respiratory diameters (size in pixels) with local maximum and minimum interpolations. Those interpolations are used to calculate the respiratory caval index.
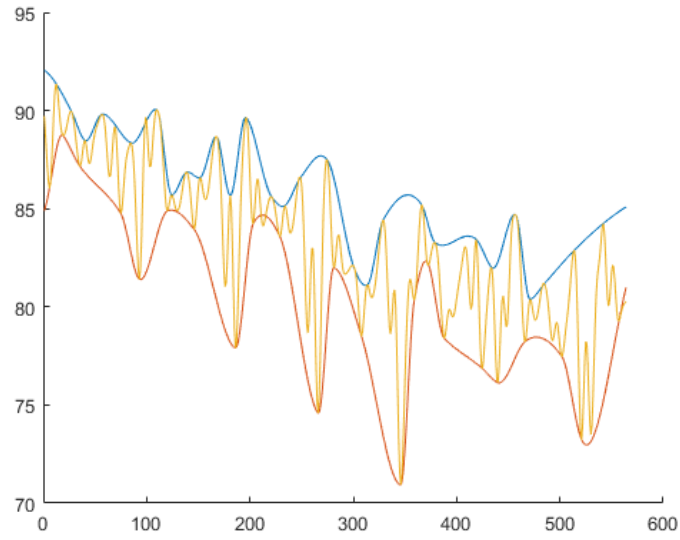

Figure 2.9: Example of cardiac diameters (size in pixels) with local maximum and minimum interpolations. Those interpolations are used to calculate the cardiac caval index.

2.7   Validation of the algorithm

The validation of the algorithm represents a fundamental step in this thesis. For a qualitative validation, the results of the algorithm were seen by a physician expert in cardiology, and confronted visually with an already existing algorithm used to track the myocardial tissue, using the same technique of the speckle tracking. Since the commercial algorithm was used to track the movements of the heart, some adjustments on the written code had to be made to match it. After the physician noted a similar behavior between the two algorithms, it was possible to use a more quantitative approach to validate the results. Initially, the idea was to validate in the algorithm in a quantitative manner by doing a comparison between the dimensions of the mean diameters obtained between the already existing algorithm (the viper), and the one using speckle tracking. For this type of validation eight videos of vena cava echographies were used, six of them having a duration of around thirty seconds, one having a duration of a minute and a half, and two of them having a duration of around five minutes. The two longest videos were recorded at 10 fps , while the other seven were recorded at 30 fps. Videos of different duration and fps were used to see how the developed algorithm would work under different conditions. Unfortunately, the algorithm with speckle tracking and the viper in three of the videos could not be used to follow the displacements of the same section of the vessel. In those cases the confrontation between the results of the two algorithms it is not possible. Since the validation using only the already existing algorithm was not possible, for each video the sections of interest of the inferior vena cava were segmented manually on a certain number of equidistant frames (for equidistant frames it is intended that each N frames of the video the segmentation is done). In this way it is not used a population of frames taken only at the beginning of the video or at the end, but all along it. For the six short videos (the ones with a length of around 30 seconds) a population of thirty frames was taken, while for the longer ones fifty frames were taken. The mean diameters were then calculated for the frames segmented manually and for the corresponding ones segmented with the speckle tracking. Then, the student test was performed using the matlab function ttest2 between the mean manual diameters and the mean speckle ones. Also, a parameter defined as error for each frame was calculated and his formula is the following:

$$\frac{|d_{manual} - d_{speckle}|}{d_{manual}}$$

Here d_{manual} is the mean manual diameter for the current frame, while $d_{speckle}$ is the mean speckle diameter for the current frame. Also, for the five videos where it was possible to follow the displacements of a similar section of the vessel for both algorithms, the comparison for the mean diameters calculated on each frame was done, again by using the student test and the parameter previously defined as error, but this time instead of using the manual diameter as reference, the one calculated with viper is. So, in this case, the formula for the error would be:

$$\frac{|d_{viper} - d_{speckle}|}{d_{viper}}$$

Also, a comparison of the obtained CI, RCI and CCI was done. In this case, the bland-altman graph was used as instrument to make the comparison between the results. For the bland-altman plot it was used the function BlandAltmann present on the matlab file exchange[39]

2.8 Proposed algorithm on the transverse plane

For the algorithm on the transverse plane, the procedure was similar to the one on the longitudinal plane. The initialisation is done by positioning the points on the borders of the inferior vena cava, then the points are fitted to an ellipse with the function fit_ellipse,m found on the matlab file exchange [40]. This ellipse has twelve points. After the initialization the tracking for each point is done in a similar way to the tracking done on the longitudinal algorithm but in this case a template of 41x41 and a search area of 51x51 pixels are used. The displacements of a point are filtered only if the value of the maximum of the correlation peak is inferior to 0.8 or if the displacement is superior to 15 pixels. The used filter is a median filter, used with the two nearest points to the point of interest. In this algorithm no terms with the gradient are used. The realignment compared to the first frame is generally not necessary. However, for some particular subjects there were better results by doing it, and the realignment was done in this case each ten frames. After that the displacements are calculated, the points are fitted again to an ellipse of 12 points, and the whole procedure is repeated for each frame of interest. In this case, to calculate the mean diameter on each frame, first the area of the ellipse is calculated by πab, where a and b represent the two semi axis. Then the mean diameter is calculated by using the following formula: $2\sqrt{Area/\pi}$. The caval index is calculated in the same way of the one of the longitudinal plane. The steps taken to validate the algorithm on the transverse plane are the same taken for the longitudinal one, except that the subjects used for this validation are a total number of eight, and the diameters on the transverse plane were not calculated manually.

2.9 Performances at different frame rates

In literature it is generally suggested to use an acquisition frame rate of at least 30-40 fps, but generally the articles talk about the ideal frame rate to follow the displacements of the myocardial tissue and not to follow the borders of the inferior vena cava. So, some tests to see what would be the ideal frame rate to acquire data of the vena cava on the longitudinal plane had been made. For the videos acquired at 30 fps (subjects 1,2,3,4,5,6) an acquisition of 15, 10 and 5 fps was simulated. For the videos with an acquisition of 10 fps, only an acquisition of 5 fps was simulated. To simulate a lower acquisition rate, some frames were simply skipped during the usage of the speckle algorithm. For instance if the starting acquisition is of 30 fps and we want to simulate an acquisition of 15 fps, the algorithm is ran only on the odd frames,so for 2 frames of the video, one of them is skipped. To simulate an acquisition of 10 fps the algorithm is ran only on 1 out of 3 frames, and for an acquisition of 5 fps the algorithm is ran on 1 out of 4 frames. To simulate an acquisition of 5 fps with a starting one of 10, the algorithm is ran on 1 out of 2 frames, because the starting frame rate was lower. After the various simulations, the mean diameters were calculated for each frame, and a spline interpolation was used to have the same number of samples as the original acquisition. After that, the student test was performed between the original acquisition and the simulations. Also, the error was calculated for each frame, and was defined as:

$$\frac{|d_{original} - d_{simulation}|}{d_{original}}$$

The performances of the transverse algorithm at different frame rates was also tested, and in this case all the original acquisitions were done at 30 fps. Finally a, comparison of the caval indexes

obtained at different frame rates was also done, but only for 15 and 10 fps. The 5 fps acquisition in this case were excluded mainly because in some cases the tracking was completely lost, and also because the if the acquisition is done at 5 Hz, the nyquist frequency would become of 2.5 Hz cutting a part of the band of interest for the cardiac caval index.

Chapter 3

Results

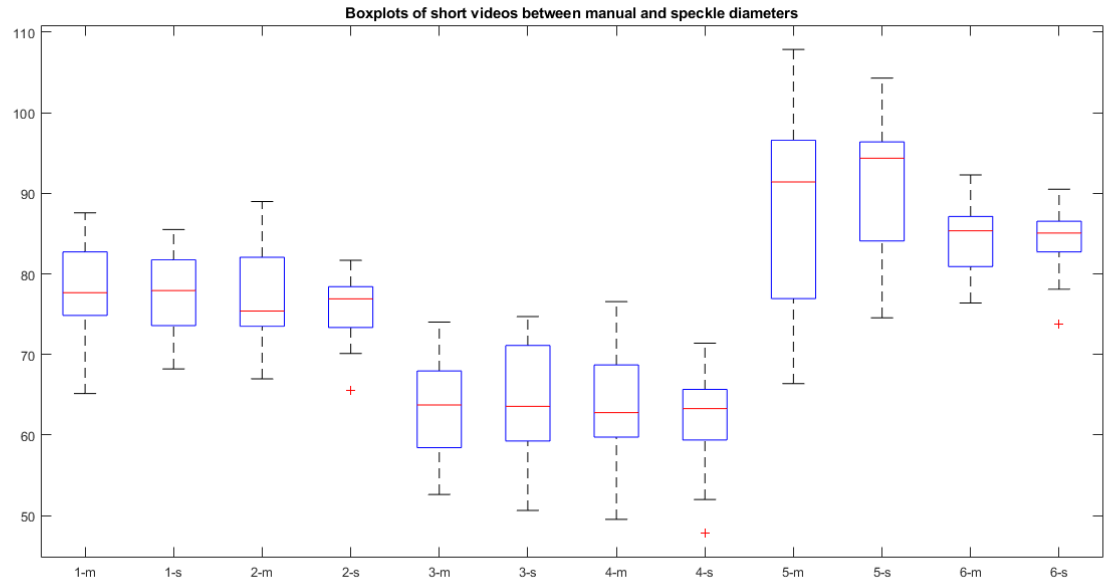## 3.1 Comparison between manual and speckle diameters, longitudinal plane

Figure 3.1: Boxplots of the subjects with short videos. The red line is the median and the blue lines above and below the red one represent respectively the 75th and 25th percentile. The diameters are expressed in pixels. The letter 'm' next to the number of the subject represent the diameters calculated manually, while the letter 's' represents the diameters obtained with the speckle tracking.
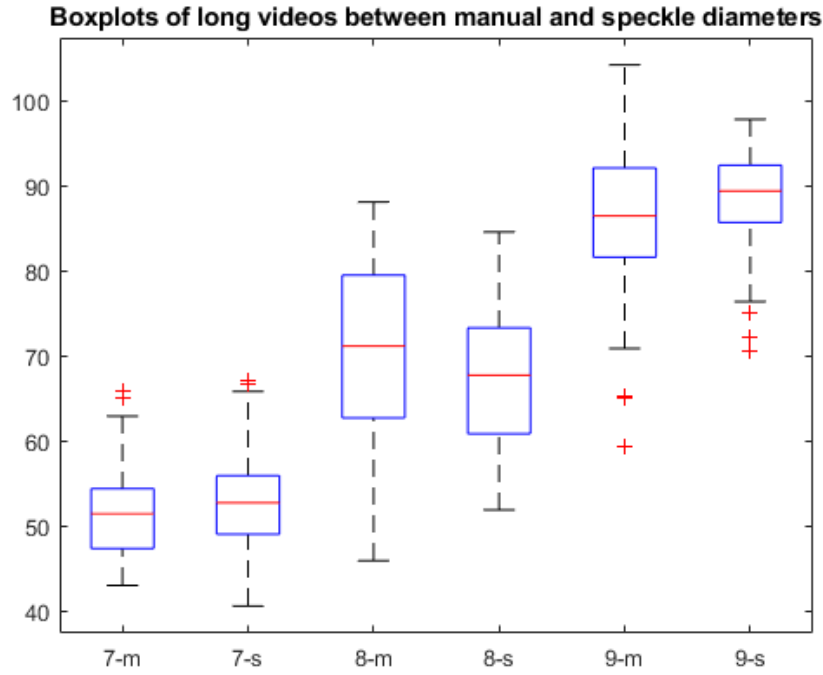
Figure 3.2: Boxplots of the subjects with long videos. The red line is the median and the blue lines above and below the red one represent respectively the 75th and 25th percentile. The diameters are expressed in pixels. The letter 'm' next to the number of the subject represent the diameters calculated manually, while the letter 's' represents the diameters obtained with the speckle tracking.

Subject	Mean Error	Standard deviation of the error
1	0.0329	0.0297
2	0.0463	0.037
3	0.0712	0.0652
4	0.0505	0.0351
5	0.0717	0.073
6	0.0318	0.0216
7	0.0689	0.0619
8	0.0866	0.064
9	0.0656	0.0647
Mean	0.05839	0.05024

Table 3.1: Table with the comparison between the manual and speckle mean diameters,longitudinal plane
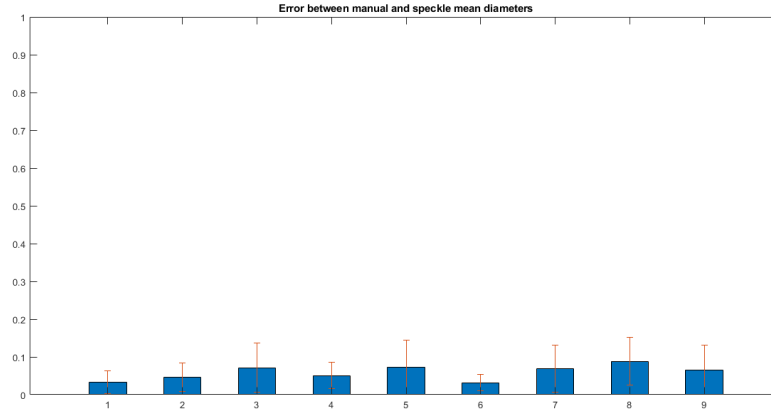
Figure 3.3: Graphics of the error between manual diameters and diameters obtained with the speckle. Mean value and standard deviation of the errors is represented.

In this section there is the comparison between the diameters calculated manually and those obtained with the speckle algorithm. As previously stated, the student test was performed on between the data with manual diameters and diameters obtained with speckle tracking. On all subjects the null hypothesis was accepted, which indicates that the two populations of diameters did not show statistical differences, at least for what concerns the mean. It is possible to notice that in the most cases, the diameters calculated manually show an a wider array of dimensions, it is easily seen on the maximum and minimums of the boxplots. This is probably due to the fact that the proposed algorithm has some difficulty to follow abrupt displacements, due to the limitations imposed by the dimensions of the search area. This may lead in some cases to the loss of tracking for certain specific frames, and also to the lesser wide array of dimensions for the diameters. For all the subjects it is possible to notice that the mean error is the always inferior to 0,1, and that the global mean error is of 0,05839. This error was deemed acceptable since in the case of some acquisitions there was a low frame rate, and in other cases the quality of the acquisitions was not ideal . Generally speaking, subject 1,2,6 and 9 had the acquisitions with the best quality and most stable noise overall. And subject 1,2 and 6 have the lowest errors of all acquisitions. Subject 9 despite having a good acquisition still has a relatively high error. This is probably due to the low frame rate of the video. The subjects 3 and 7 had the worse acquisition, with some portions of the borders of the vein which sometimes became completely black and not distinguishable from the internal area of the vein. This has of course influenced the error in a negative manner. The subjects presenting echographies with lower frame rates and lesser quality had a worse performance of the algorithm which was expected.

3.2 Comparison between speckle and viper diameters, longitudinal plane

For the comparison between speckle diameters and viper ones, only the subjects where it was possible to use the algorithm on the same portion of the vessel were taken into consideration. Those subjects were the 2,4,5,6 and 9. For what concerns subject 2, it is possible to notice that it is the subject with the lowest mean error, which is normal, considering that the acquisition was of good quality, and that there were not abrupt displacements, which would be a weak point for the speckle tracking algorithm. However, even if the mean diameters and their standard deviations are extremely close, the student test rejected the null hypothesis. This is probably due to the spike present on the diameters found with the viper algorithm, which is probably an error. Subject 4, on the other end, presents a slightly higher error, but in this case the student test accepted the null hypothesis. For subject 5, it is possible to notice that the mean diameter found with the speckle is generally inferior compared to the mean diameter obtained with the viper, even if only by around 8 pixels. This bias is possibly due to the manual initialisation: in the case of the viper, the borders are found in a semi-automated way, while the speckle tracking requires the points on the borders to be selected manually, and doing a manual initialisation with a pixel precision can be difficult. And if the initialisation is slightly off, the speckle tracking will bring the error all along the way. Even in this case the null hypothesis was rejected. For subject 6, the error was low, but there was still a slight bias in the mean diameters calculated with the speckle tracking. Again, the null hypothesis was rejected. Finally, for subject 9, the error was the second highest. This is probably due to the ending frames, where it is possible to notice that the diameters found with the speckle tracking deviate from the ones found with the viper. Also, it was one of the videos where the frame rate was low (10 fps).The null hypothesis was also rejected in this case. Generally specking, the diameters found with the speckle tracking and with the viper are quite similar, and even in the worst cases the difference is not enormous. Also, the mean percentage of points inside the confidence interval of the bland-altman plot is of 94,56, which is quite close to the 95 percent required to confirm that the two methods of measurements are interchangeable. However this condition is not sufficient, and the bias should also be low. In this case, the mean error of all the five subject is of 0.0439, which is low enough to consider that the two algorithms work in a similar way, even if they are not equivalent one to each other.

Subject	$Speckle_m$	$Viper_m$	$Speckle_s$	$Viper_s$	$Error_m$	$Error_s$	$Bl - Alt$
2	83.8354	84.4201	3.2289	3.6005	0.0165	0.0126	0.9207
4	61.3872	61.8165	5.7496	6.2897	0.0347	0.0250	0.9507
5	84.8824	92.0274	8.1473	11.9389	0.0795	0.0435	0.9720
6	79.6241	81.8469	4.3217	3.7123	0.0330	0.0210	0.9486
8	80.5448	84.1146	7.0696	8.7689	0.0558	0.0421	0.9363
Mean	-	-	-	-	0.0439	0.02884	0.9457

Table 3.2: Table with the comparison between the viper and speckle mean diameters,longitudinal plane. The subscript 'm' indicates the mean and the subscript 's' indicates the standard deviation.Bl-Alt indicates the percentage of points inside the confidence interval of the bland-altman plot.
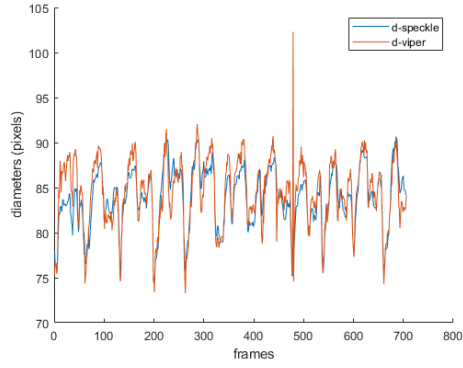
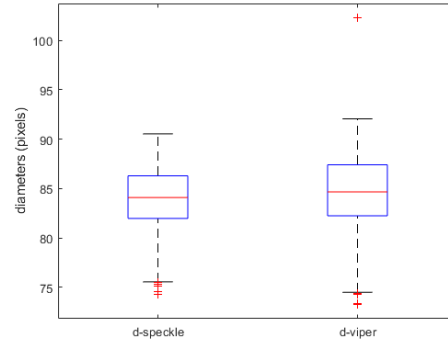Figure 3.4: Subject 2, mean diameters on each frame(in pixels)

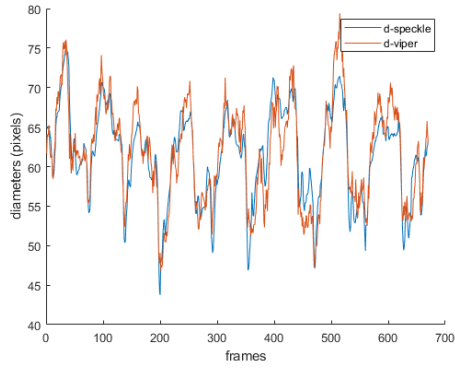Figure 3.5: Subject 2, boxplots of mean diameters(in pixels)

Figure 3.6: Subject 4, mean diameters on each frame(in pixels)
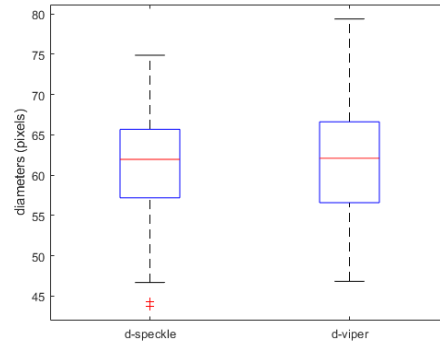

Figure 3.7: Subject 4, boxplots of mean diameters(in pixels)
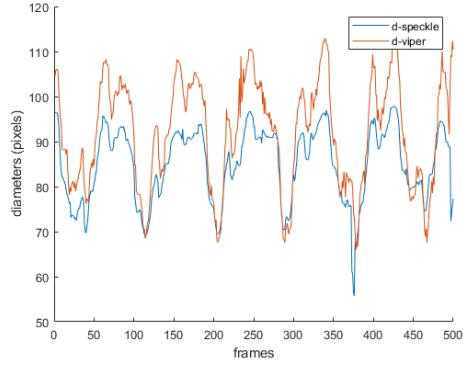
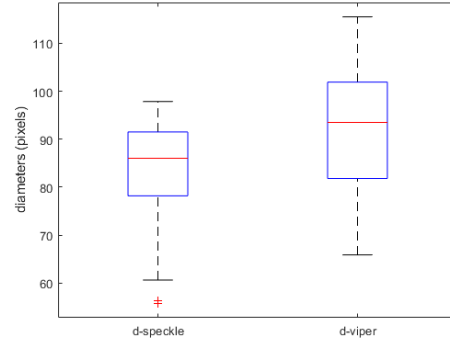Figure 3.8: Subject 5, mean diameters on each frame(in pixels)

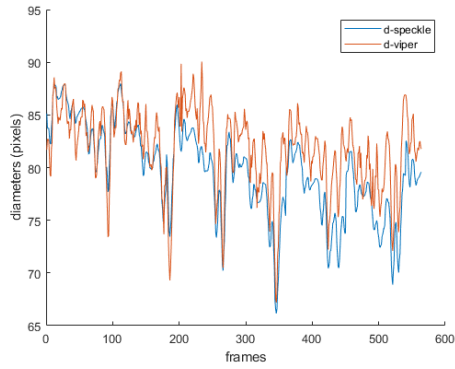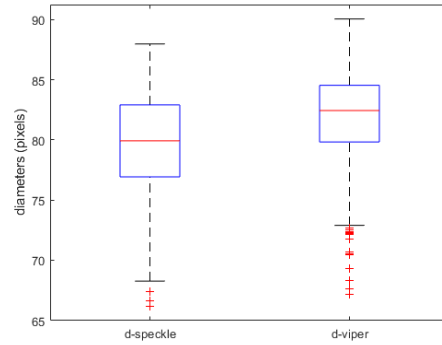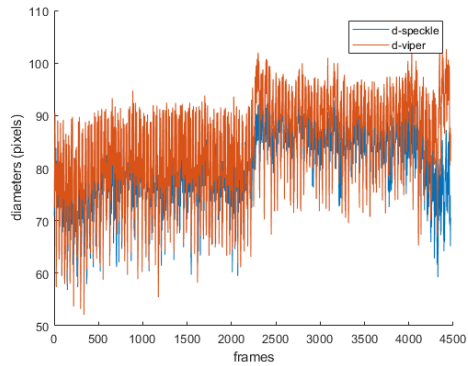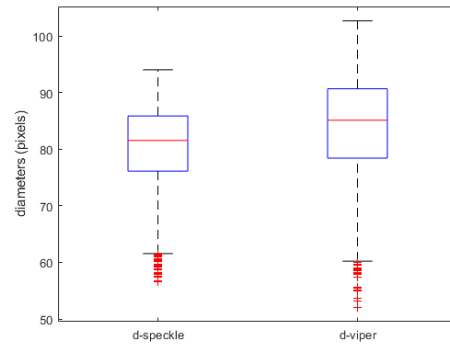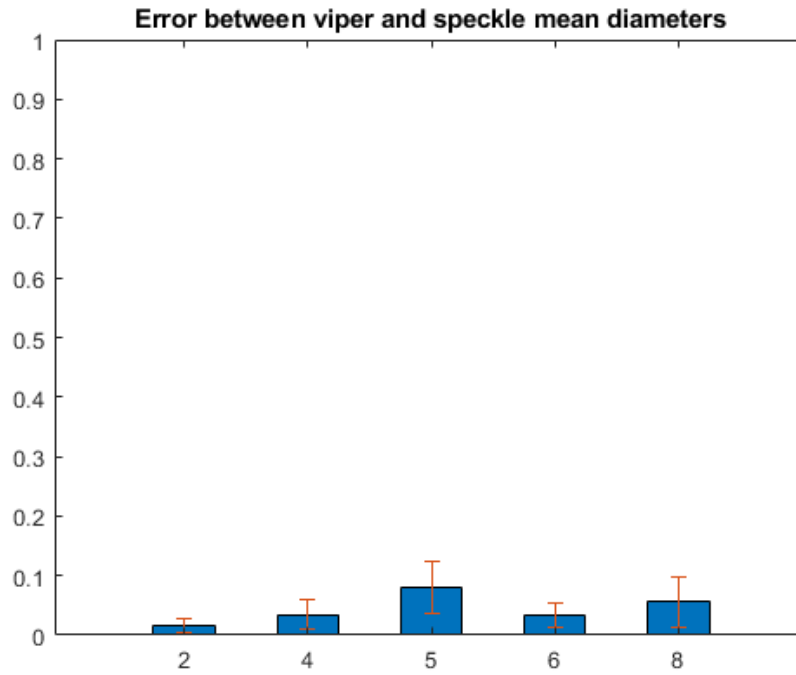Figure 3.9: Subject 5, boxplots of mean diameters(in pixels)

Figure 3.10: Subject 6, mean diameters on each frame(in pixels)

Figure 3.11: Subject 6, boxplots of mean diameters (in pixels)

Figure 3.12: Subject 9, mean diameters on each frame (in pixels)

Figure 3.13: Subject 9, boxplots on mean diameters (in pixels)

Figure 3.14: Graphics of the error between viper diameters and diameters obtained with the speckle. Mean value and standard deviation of the errors is represented.

3.3 Comparison between speckle and viper caval indexes, longitudinal plane

		Parameters					
		Bl-Alt	MCI-s	MCI-v	StdCI-s	StdCI-v	Error
Subject 2	CI	0.9717	0.1333	0.1234	0.0202	0.0178	0.0802
	RCI	0.9603	0.0284	0.0431	0.0076	0.0149	0.341
	CCI	0.9207	0.0858	0.0745	0.0212	0.0231	0.1517
Subject 4	CI	0.9343	0.2908	0.2480	0.0445	0.0165	0.1726
	RCI	0.9985	0.1336	0.0991	0.0404	0.0223	0.3481
	CCI	0.9791	0.1438	0.1379	0.0488	0.0482	0.04279
Subject 5	CI	1	0.2909	0.4087	0.0476	0.0589	0.2882
	RCI	0.8960	0.1633	0.2098	0.0188	0.0393	0.2216
	CCI	0.9520	0.1449	0.2173	0.0405	0.0621	0.3332
Subject 6	CI	1	0.1416	0.1265	0.0315	0.0238	0.1194
	RCI	0.9982	0.0505	0.0742	0.0149	0.0210	0.3194
	CCI	0.9273	0.0643	0.0547	0.0318	0.0257	0.1755
Subject 9	CI	0.9418	0.2047	0.2523	0.0614	0.0595	0.1887
	RCI	0.9592	0.0952	0.1248	0.0313	0.0347	0.2372
	CCI	0.9372	0.1296	0.1192	0.0428	0.0452	0.0872
Mean	CI	0.9696	-	-	-	-	0.1698
	RCI	0.9624	-	-	-	-	0.2935
	CCI	0.9432	-	-	-	-	0.1581

Table 3.3: Table with the comparison of the the various caval indexes obtained with speckle tracking and viper,longitudinal plane. The values in the column Bl-Alt are the percentage of points in the confidence area of the Bland-altman graph. MCI and StdCI are the mean and standard deviations of the caval indexes obtained with both algorithms. Error is the difference between the mean CI obtained with viper and the mean CI obtained with speckle tracking, all divided by the mean CI obtained with viper

For what concerns the different types of caval indexes calculated with speckle tracking and viper, it is possible to notice that in none of the cases the student test accepted the null hypothesis. Also, the error is much higher than when the diameters were calculated. This shows that a minimal bias towards the calculation of the mean diameters can lead to a much more different value of the different types of caval indexes. Generally, if the error was higher when the diameters were calculated, it will also be higher when the caval indexes are calculated. The most flagrant example is the subject 5, that having by far the highest error on the calculation of the diameters, also show the highest error on the calculation of the caval index. It should be noted that the error is of about 0.15 for caval index and cardiac caval index, but it is about of 0.3 for the respiratory caval index, which is approximately the double of the two other values. For what concerns the bland-altman graphs, it is possible to notice that the mean percentages of the points inside the confidence interval of the CI, RCI and CCI are respectively 96.96 %, 96.24 % and 94.32 %, two of those values are above 95%, and the one of the CCI comes close to it. However, due to the high biases it is not possible to say that the two methods to measure the various types of caval indexes are freely interchangeable.
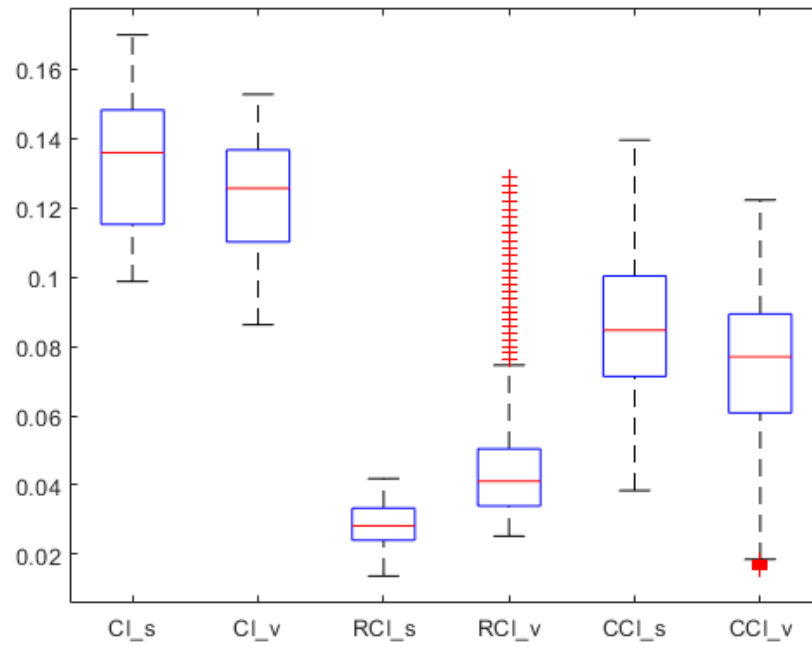
Figure 3.15: Subject 2, boxplots of CI,RCI and CCI obtained with speckle tracking and viper
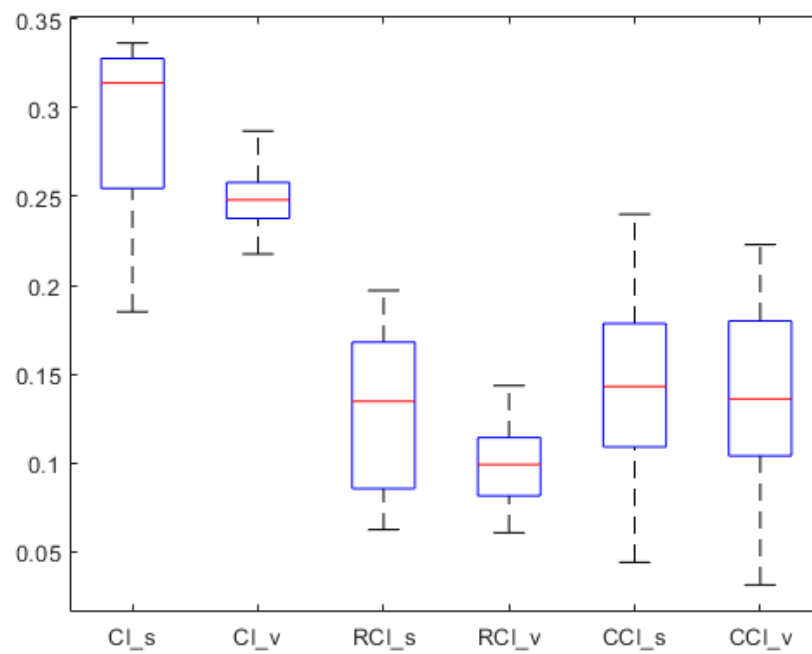
Figure 3.16: Subject 4, boxplots of CI,RCI and CCI obtained with speckle tracking and viper
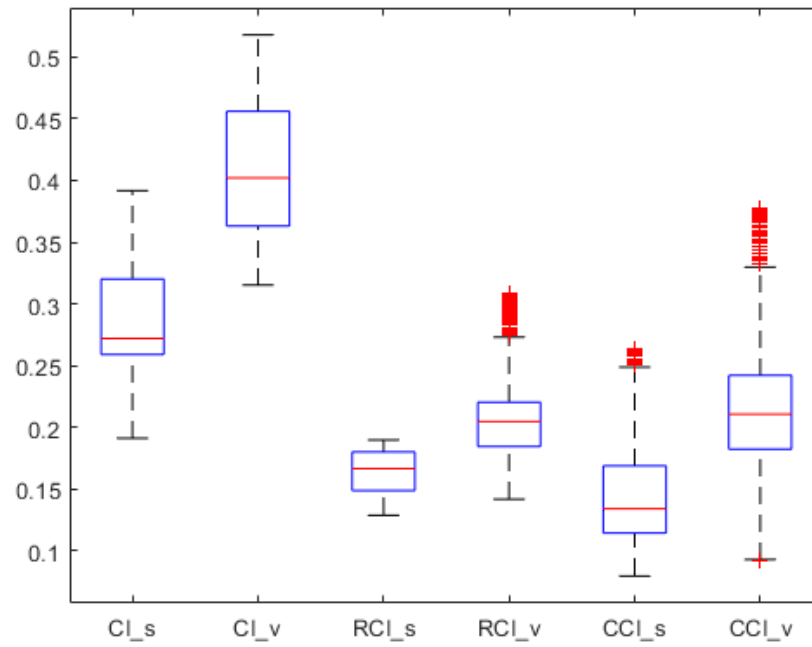
Figure 3.17: Subject 5, boxplots of CI,RCI and CCI obtained with speckle tracking and viper
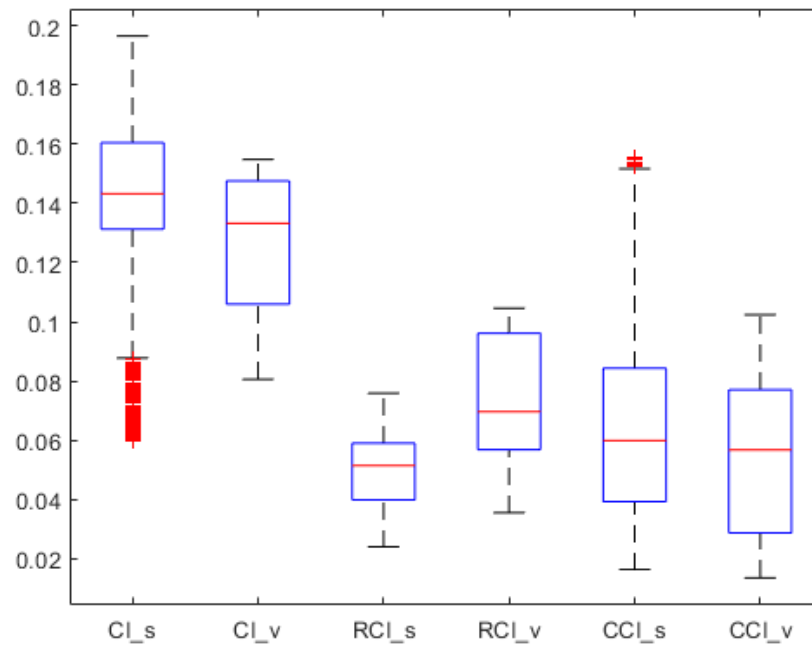
Figure 3.18: Subject 6, boxplots of CI,RCI and CCI obtained with speckle tracking and viper
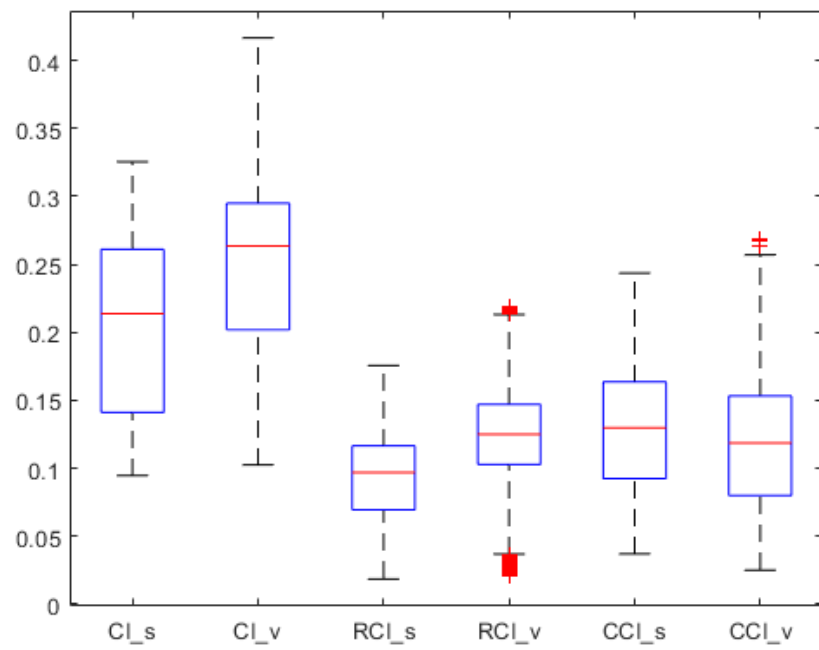
Figure 3.19: Subject 9, boxplots of CI,RCI and CCI obtained with speckle tracking and viper

3.4 Performances at different frame rates, longitudinal plane

Generally speaking, reducing the frame rate also diminishes the accuracy of the algorithm to follow the borders of the vessel. It is easily noticeable that the mean error and the standard deviation of the error increase as the frame rate lowers. For the acquisitions with an original frame rate of 30 fps , subjects 3 and 7 had the least stable noise, and it is easily noticeable that the error increases much faster compared to the other subjects. Also, the students tests in the most cases rejected the null hypothesis, meaning that the frame rate changes can affect the results in a sensible manner. However, it must be noted that qualitatively, the borders of the vessels are still followed in an acceptable manner at a ten fps. This result is in contrast with the ones found in literature, where it is suggested to have a frame rate of at least 30-40 fps. This can be due to two factors. The first one is that the results found in literature are mostly about the speckle tracking applied on myocardial tissue, while in this case the tracking is used on a vessel.It is plausible to think that the more abrupt displacements of the heart require an higher frame rate to be followed, at least compared to the displacements of the borders of a simple vessel. Second, the realignment of the points compared to the first frame, even if it is done sparingly, can help to mitigate the effect of the low frame rate, since on the first frame there is the warranty that the points are well placed. Also, certain acquisitions of the inferior vena cava are done at at 10 fps, due to the depth of the vein, so in some cases it would not be possible to have an higher frame rate. Instead, if the frame rate goes down to 5, it can be noted that graphically the boxplots change noticeably, and also that the error increases a lot compared to the increase that there is from the jump between 15 and 10 fps. Also, if the acquisition is done at 5 fps, the maximum frequency which can be reconstructed, respecting the Nyquist theorem, would be of 2.5 Hz. This frequency is really near the physiological heart rate and by computing the dimensions of the diameters in function of the time, some displacements on the higher frequencies could be missed. So, it is mandatory to have a frame rate of at least 10 Hz. For what concerns the various caval indexes, it is possible to notice that at 15 and 10 fps there is not a great difference between the CI and the RCI, but there is a great one for the CCI. This is not surprising , since the CCI depends more from the higher frequencies, and a lower frame rate is more likely to influence those values.
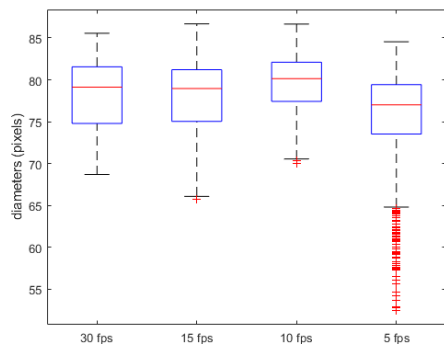
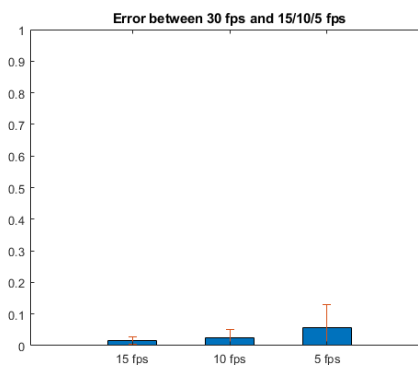Figure 3.20: Subject 1, boxplots of mean diameters on 30,15,10 and 5 fps

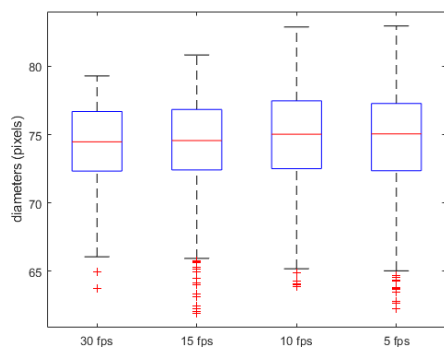Figure 3.21: Subject 1, errors between original acquisition and simulated lower frame rates

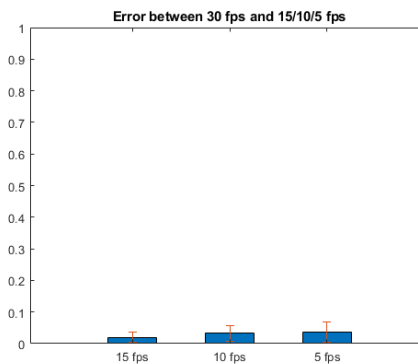Figure 3.22: Subject 2, boxplots of mean diameters on 30,15,10 and 5 fps

Figure 3.23: Subject 2, errors between original acquisition and simulated lower frame rates
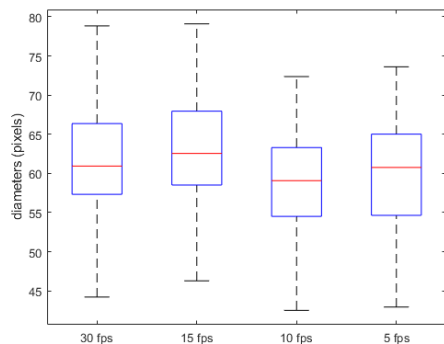
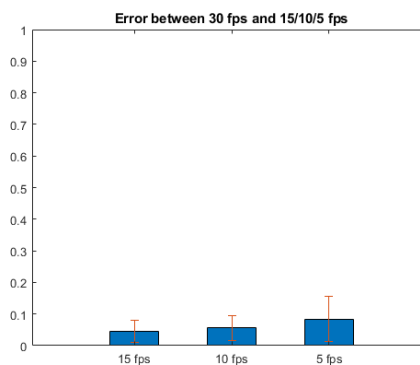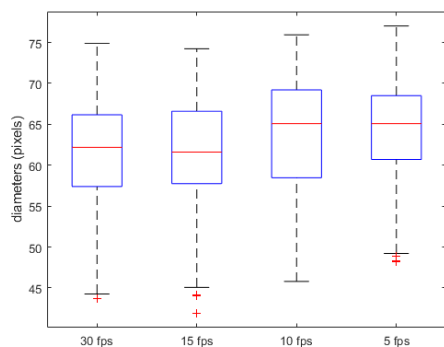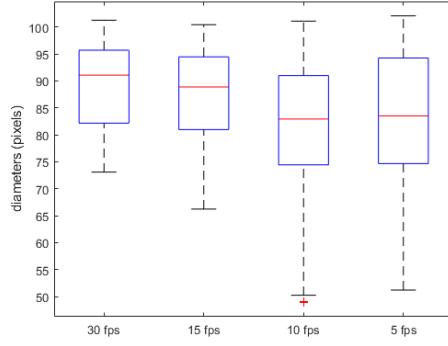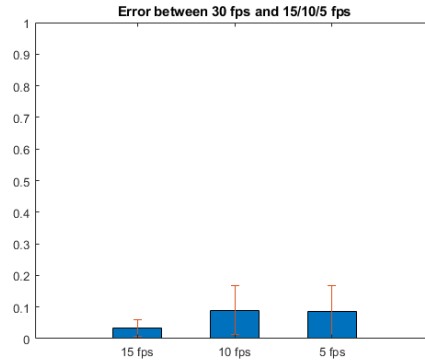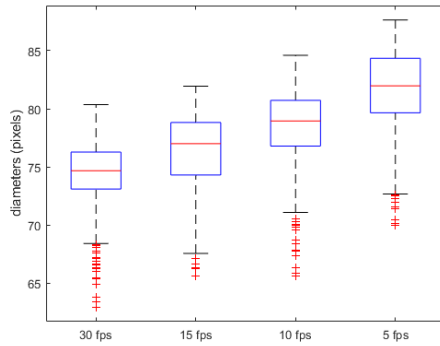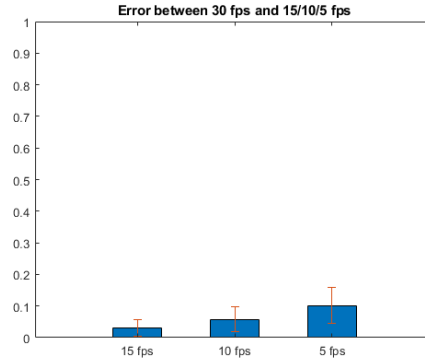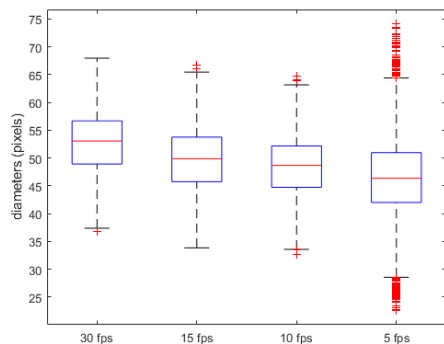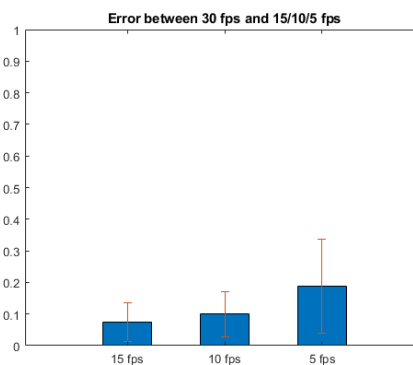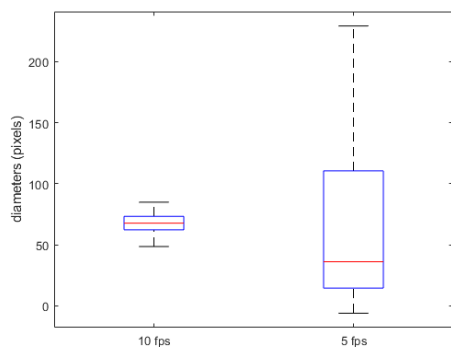Figure 3.24: Subject 3, boxplots of mean diameters on 30,15,10 and 5 fps

Figure 3.25: Subject 3, errors between original acquisition and simulated lower frame rates

Figure 3.26: Subject 4, boxplots of mean diameters on 30,15,10 and 5 fps

Figure 3.27: Subject 4, errors between original acquisition and simulated lower frame rates

Figure 3.28: Subject 5, boxplots of mean diameters on 30,15,10 and 5 fps

Figure 3.29: Subject 5, errors between original acquisition and simulated lower frame rates

Figure 3.30: Subject 6, boxplots of mean diameters on 30,15,10 and 5 fps

Figure 3.31: Subject 6, errors between original acquisition and simulated lower frame rates

Figure 3.32: Subject 7, boxplots of mean diameters on 30,15,10 and 5 fps

Figure 3.33: Subject 7, errors between original acquisition and simulated lower frame rates

Figure 3.34: Subject 8, boxplots of mean diameters on 10 and 5 fps
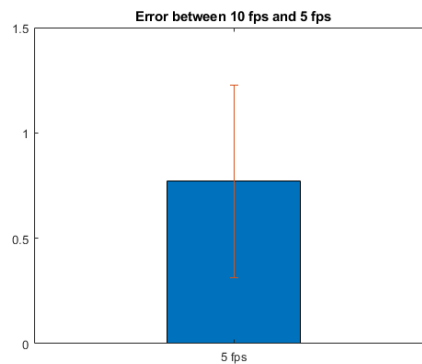
Figure 3.35: Subject 8, errors between original acquisition and simulated lower frame rates

		Frame rate		
		15	10	5
Subject 1	T-test	0	1	1
	Mean Error	0.0158	0.0253	0.0713
	Std Error	0.0130	0.0265	0.0880
Subject 2	T-test	0	1	0
	Mean Error	0.0204	0.0320	0.0412
	Std Error	0.0161	0.0244	0.0329
Subject 3	T-test	0	1	1
	Mean Error	0.0447	0.0652	0.0778
	Std Error	0.0373	0.0468	0.0669
Subject 4	T-test	0	1	1
	Mean Error	0.0228	0.0539	0.0723
	Std Error	0.0200	0.0426	0.0579
Subject 5	T-test	1	1	1
	Mean Error	0.0321	0.0836	0.0986
	Std Error	0.0255	0.0734	0.0999
Subject 6	T-test	1	1	1
	Mean Error	0.0315	0.0570	0.1096
	Std Error	0.0268	0.0368	0.0564
Subject 7	T-test	1	1	1
	Mean Error	0.0745	0.0995	0.1889
	Std Error	0.0621	0.0711	0.1485
Subject 8	T-test	-	-	1
	Mean Error	-	-	0.7664
	Std Error	-	-	0.4571
Subject 9	T-test	-	-	1
	Mean Error	-	-	0.0351
	Std Error	-	-	0.0314

Table 3.4: Table with the comparison between the diameters of the original acquisition and the various simulations at lower fps. A 0 in the T-test means that the null hypothesis was accepted, a 1 means that the hypothesis was rejected. Subjects 8 and 9 had an original acquisition of 10 fps, so the simulation was only done at 5 fps.

		Frame rate		
		CI	RCI	CCI
Subject 1	T-test-15 fps	1	1	0
	Error 15 fps	0.0740	0.2138	0.0130
	T-test 10 fps	1	0	1
	Error 10 fps	0.0654	0.0134	0.0909
Subject 2	T-test-15 fps	1	1	1
	Error 15 fps	0.1307	0.3915	0.1278
	T-test 10 fps	1	1	1
	Error 10 fps	0.0542	0.0735	0.0990
Subject 3	T-test-15 fps	1	0	1
	Error 15 fps	0.1721	0.0466	0.2576
	T-test 10 fps	1	1	1
	Error 10 fps	0.1597	0.1497	0.2166
Subject 4	T-test-15 fps	1	1	0
	Error 15 fps	0.1086	0.1306	0.0097
	T-test 10 fps	0	1	1
	Error 10 fps	0.0023	0.0606	0.0685
Subject 5	T-test-15 fps	1	1	0
	Error 15 fps	0.1027	0.0785	0.0181
	T-test 10 fps	1	1	1
	Error 10 fps	0.4484	0.4449	0.5580
Subject 6	T-test-15 fps	0	1	1
	Error 15 fps	0.0197	0.0310	0.0657
	T-test 10 fps	1	1	1
	Error 10 fps	0.0427	0.0371	0.0968
Subject 7	T-test-15 fps	1	1	0
	Error 15 fps	0.0486	0.1431	0.0141
	T-test 10 fps	1	1	1
	Error 10 fps	0.0324	0.1060	0.0682
Mean	Error 15 fps	0.09377	0.1479	0.0956
	Error 10 fps	0.1150	0.1265	0.2984

Table 3.5: Table with the comparison between the caval indexes of the original acquisition and the various simulations at lower fps. A 0 in the T-test means that the null hypothesis was accepted, a 1 means that the hypothesis was rejected.
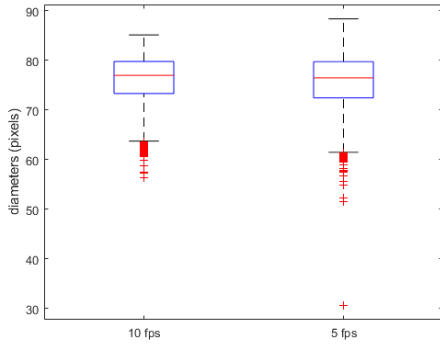
Figure 3.36: Subject 9, boxplots of mean diameters on 10 and 5 fps
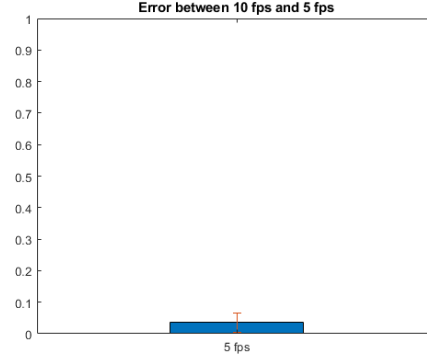
Figure 3.37: Subject 9, errors between original acquisition and simulated lower frame rates

3.5 Comparison between speckle and viper diameters, transverse plane

It is possible to notice that the error between the mean transverse diameters is around 6,64 %. It is higher than the ones found with the longitudinal algorithm. A factor contributing to the bias can be for subject one and subject two the fact that on the long run, the diameter of the vein tends to be reduced, due to the loss of the track of certain points of the borders. However, after a while, it seems that those points still stabilize and follow the the same trend of the viper algorithm, only with the aforementioned bias. For what concerns the bland altman plots, the mean number of points inside the confidence range is of 94.49 %, which is close to 95%. It should be noted that for the subject 7, both algorithms at a certain point lost tracking of the vena cava, although the speckle one lost track around 300 frames before the viper. The comparison of the diameters for this subject was done for the frames where both algorithms managed to follow correctly the borders. The student test was performed on all subjects, and for all of them the null hypothesis was rejected.
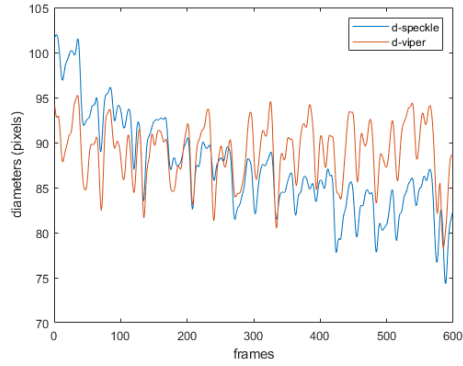
Figure 3.38: Subject 1,transverse plane, mean diameters on each frame (in pixels)
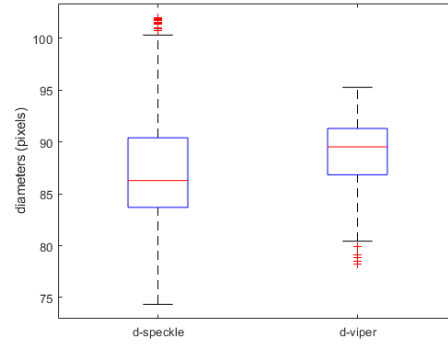
Figure 3.39: Subject 1,tranverse plane, box-plots on mean diameters (in pixels)
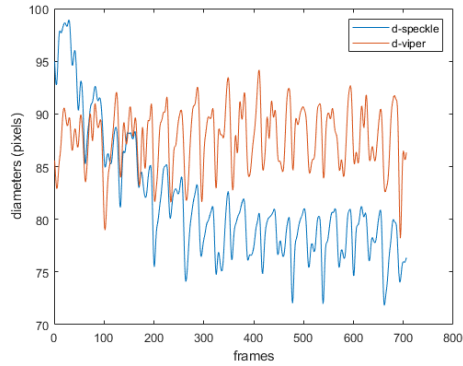
Figure 3.40: Subject 2,transverse plane, mean diameters on each frame (in pixels)
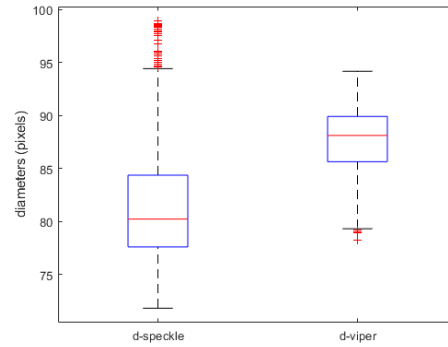
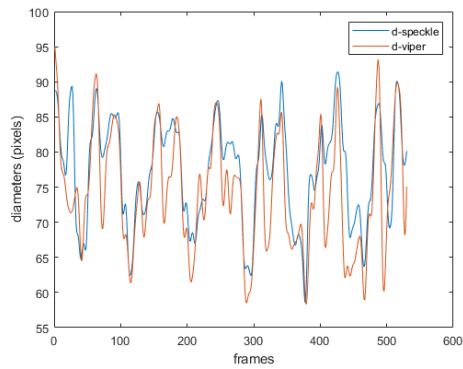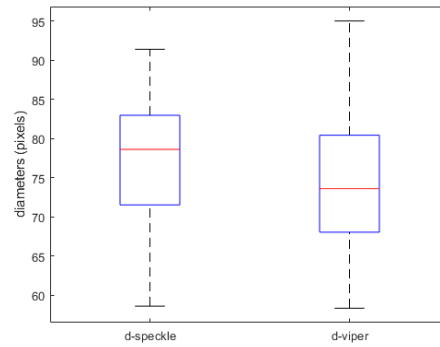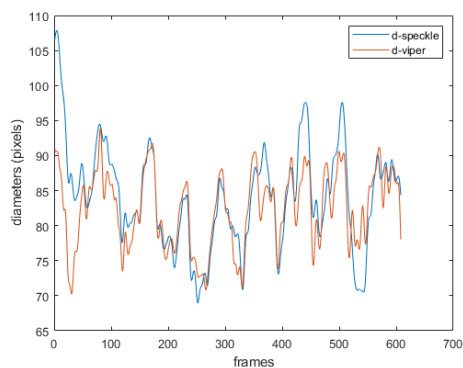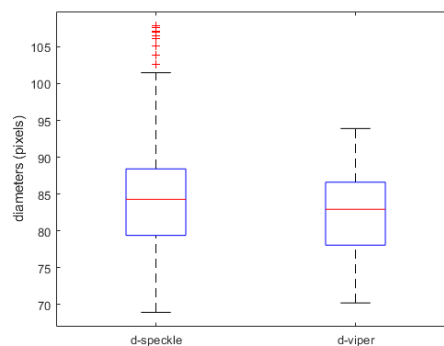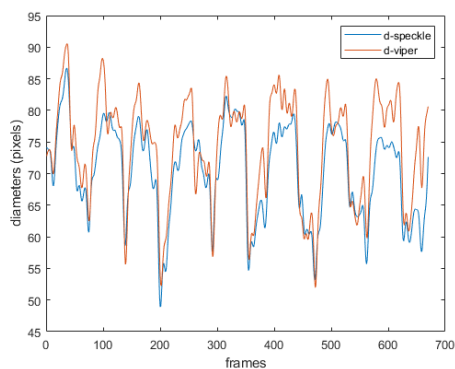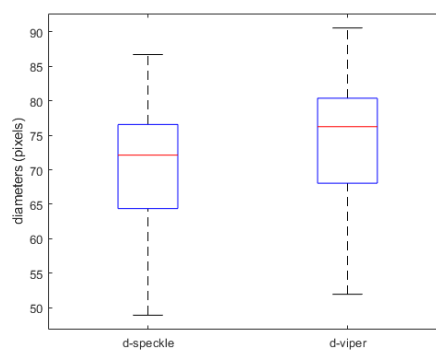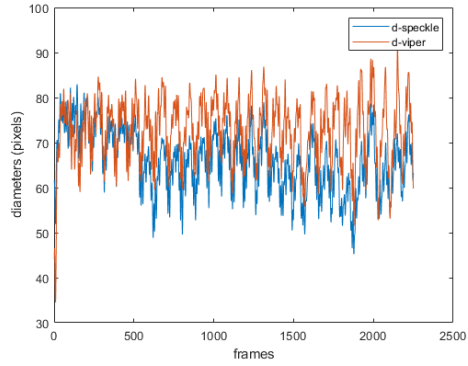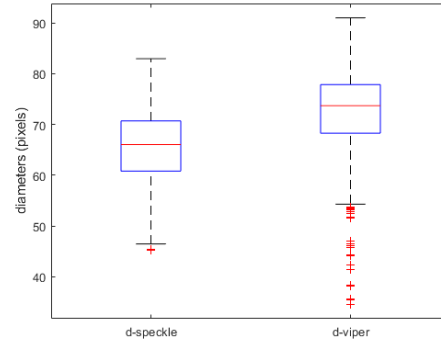Figure 3.41: Subject 2,transverse plane, box-plots on mean diameters (in pixels)

59
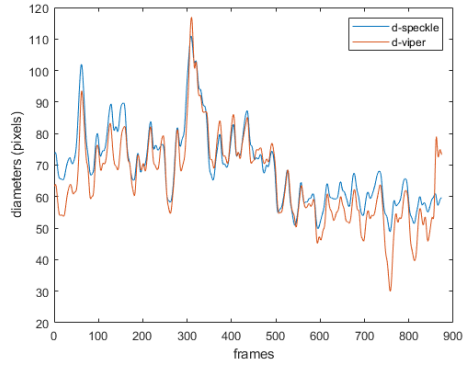
Figure 3.42: Subject 3,transverse plane, mean diameters on each frame (in pixels)
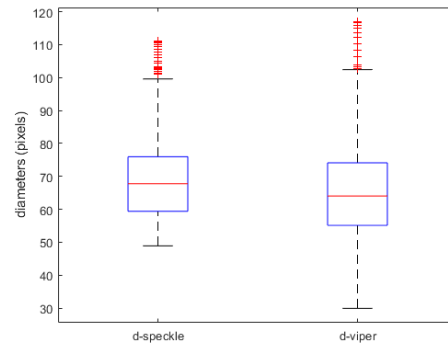
Figure 3.43: Subject 3,transverse plane, box-plots on mean diameters (in pixels)

Figure 3.44: Subject 4,transverse plane, mean diameters on each frame (in pixels)

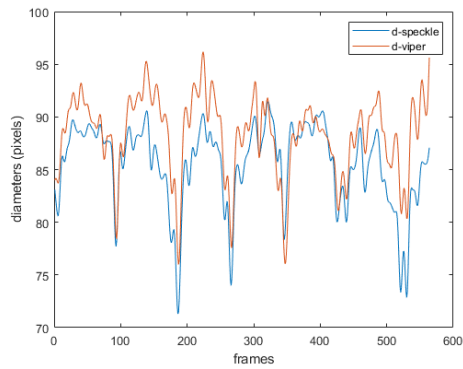Figure 3.45: Subject 4,transverse plane, box-plots on mean diameters (in pixels)

Figure 3.46: Subject 5,transverse plane, mean diameters on each frame (in pixels)
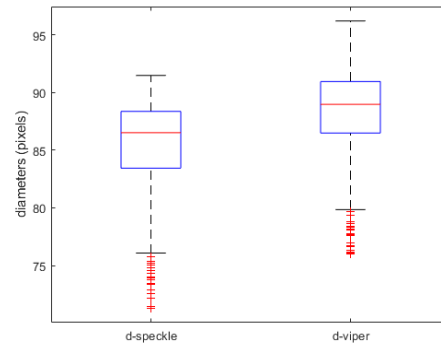

Figure 3.47: Subject 5,transverse plane, box-plots on mean diameters (in pixels)

Figure 3.48: Subject 6,transverse plane, mean diameters on each frame (in pixels)

Figure 3.49: Subject 6,transverse plane, box-plots on mean diameters (in pixels)

61

Figure 3.50: Subject 7,transverse plane, mean diameters on each frame (in pixels)

Figure 3.51: Subject 7,transverse plane, box-plots on mean diameters (in pixels)

Figure 3.52: Subject 8,transverse plane, mean diameters on each frame (in pixels)

Figure 3.53: Subject 8,transverse plane, box-plots on mean diameters (in pixels)

Subject	$Speckle_m$	$Viper_m$	$Speckle_s$	$Viper_s$	$Error_m$	$Error_s$	$Bl-Alt$
1	87.2853	88.9738	5.3887	3.2765	0.0502	0.0282	0.9583
2	81.7097	87.7265	5,8696	2.8312	0.0874	0.0378	0.9306
3	69.2772	65.6644	12.2223	13.6334	0.0879	0.0828	0.9600
4	77.3180	74.3122	7.4016	8.1382	0.0596	0.0572	0.9491
5	84.0809	82.4319	7.3207	5.4042	0.0446	0.0449	0.9342
6	70.4404	74.1244	7.4432	8.2640	0.0551	0.0375	0.9358
7	65.7665	72.8484	6.8623	7.1101	0.1100	0.0589	0.9316
8	85.4934	88.3142	3.9452	3.8080	0.0364	0.0232	0.9592
Mean	-	-	-	-	0.0664	0.0463	0.9449

Table 3.6: Table with the comparison between the viper and speckle mean diameters,transverse plane. The subscript 'm' indicates the mean and the subscript 's' indicates the standard deviation.Bl-Alt indicates the percentage of points inside the confidence interval of the bland-altman plot.

3.6 Comparison between speckle and viper caval indexes, transverse plane

For the caval indexes in the transverse plane it is possible to notice that the mean percentage of points in the confidence range of the bland altman plot for the CI, RCI and CCI are respectively 94.2 %, 94.72 % and 94.05 % . All of them are close to 95%. It is possible to notice that in the transverse plane, the mean errors are lesser for the CI and the RCI, compared to the longitudinal plane, but they are greater for the CCI. The mean error of the RCI is still the greater one. For the CI, RCI and CCI of all subjects the student test was performed, and and in this case the null hypothesis was rejected almost every time. The only cases where the null hypothesis was not rejected is for the CI on subject 2, the RCI on subject 6 and both the CI and CCI on subject 8, Unsurprisingly, those are all values where the error between speckle and viper are really low. Globally, it seems that the obtained caval indexes on the transverse plane are more similar to each others than the ones obtained on the longitudinal algorithm. This could be due to the fact that on the longitudinal plane the viper algorithm seems to be more reactive compared to the speckle one, while on the transverse plane they seem to have a similar shape, thus leading to have more similar caval indexes.

		Parameters					
		Bl-Alt	MCI-s	MCI-v	StdCI-s	StdCI-v	Error
Subject 1	CI	0.9699	0.1046	0.1303	0.0187	0.0181	0.1975
	RCI	1	0.0189	0.0213	0.0098	0.0075	0.1147
	CCI	0.9533	0.0734	0.1011	0.0175	0.0196	0.2737
Subject 2	CI	0.9773	0.1123	0.1142	0.0085	0.0148	0.0165
	RCI	0.9320	0.0238	0.0130	0.0109	0.0080	0.8369
	CCI	0.9249	0.0816	0.0918	0.0166	0.0203	0.1109
Subject 3	CI	0.8945	0.2978	0.3589	0.0767	0.0918	0.1704
	RCI	0.9904	0.1228	0.1202	0.0819	0.0648	0.0209
	CCI	0.9233	0.1823	0.2318	0.0429	0.0851	0.2137
Subject 4	CI	0.9642	0.2762	0.3210	0.0507	0.0238	0.1396
	RCI	0.9151	0.1489	0.1314	0.0181	0.0124	0.1336
	CCI	0.9340	0.1766	0.2261	0.0560	0.0625	0.2189
Subject 5	CI	0.9211	0.2004	0.1939	0.0383	0.0281	0.0334
	RCI	0.9695	0.0762	0.0708	0.0191	0.0360	0.0757
	CCI	0.9462	0.1330	0.1272	0.0330	0.0288	0.0452
Subject 6	CI	0.9134	0.3058	0.3166	0.0466	0.0510	0.0342
	RCI	0.9015	0.1564	0.1543	0.0462	0.0551	0.0140
	CCI	0.9552	0.1293	0.1761	0.0608	0.0503	0.2655
Subject 7	CI	0.9600	0.2477	0.2891	0.0392	0.0411	0.1434
	RCI	0.9040	0.0912	0.1080	0.0413	0.0337	0.1559
	CCI	0.9258	0.1251	0.1414	0.0322	0.0463	0.1159
Subject 8	CI	0.9358	0.1600	0.1608	0.0308	0.0345	0.0045
	RCI	0.9650	0.0639	0.0692	0.0181	0.0103	0.0760
	CCI	0.9611	0.0572	0.0547	0.0308	0.0283	0.0449
Mean	CI	0.9420	-	-	-	-	0.0924
	RCI	0.9472	-	-	-	-	0.1785
	CCI	0.9405	-	-	-	-	0.1611

Table 3.7: Table with the comparison of the the various caval indexes obtained with speckle tracking and viper,transverse plane. The values in the column Bl-Alt are the percentage of points in the confidence area of the Bland-altmann graph. MCI and StdCI are the mean and standard deviations of the caval indexes obtained with both algorithms. Error is the difference between the mean CI obtained with viper and the mean CI obtained with speckle tracking, all divided by the mean CI obtained with viper
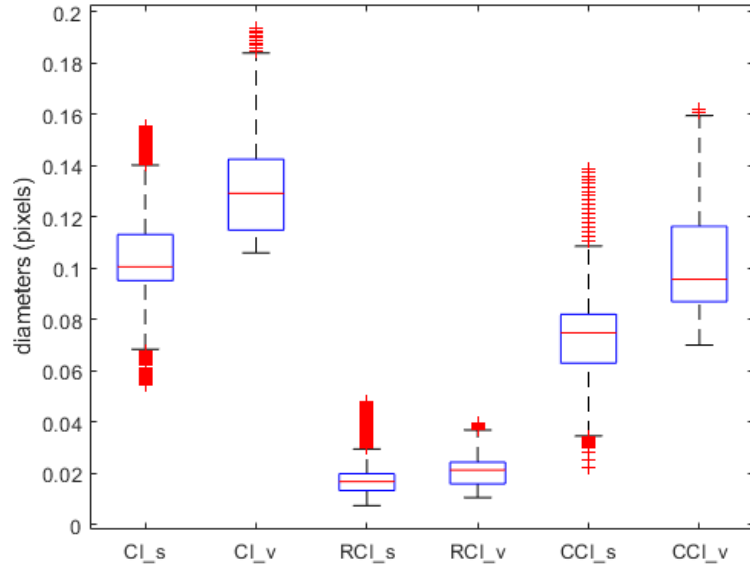
Figure 3.54: Subject 1, transverse plane, boxplots of CI,RCI and CCI obtained with speckle tracking and viper
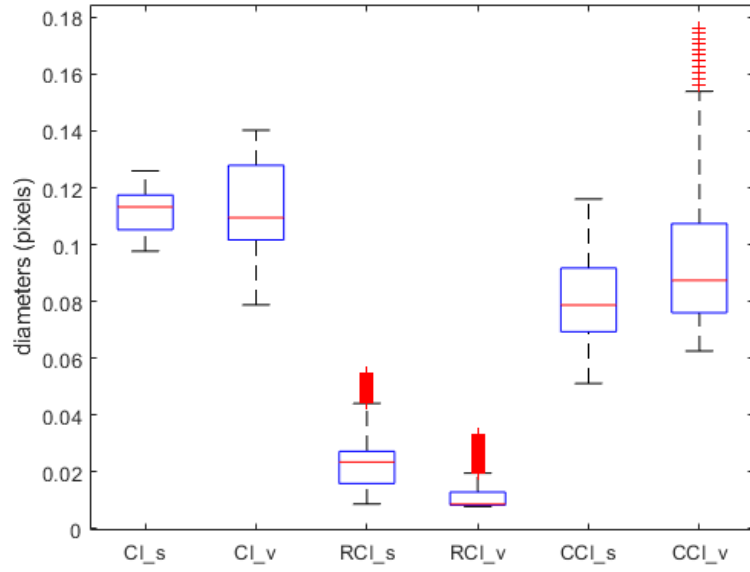

Figure 3.55: Subject 2,transverse plane, boxplots of CI,RCI and CCI obtained with speckle tracking and viper
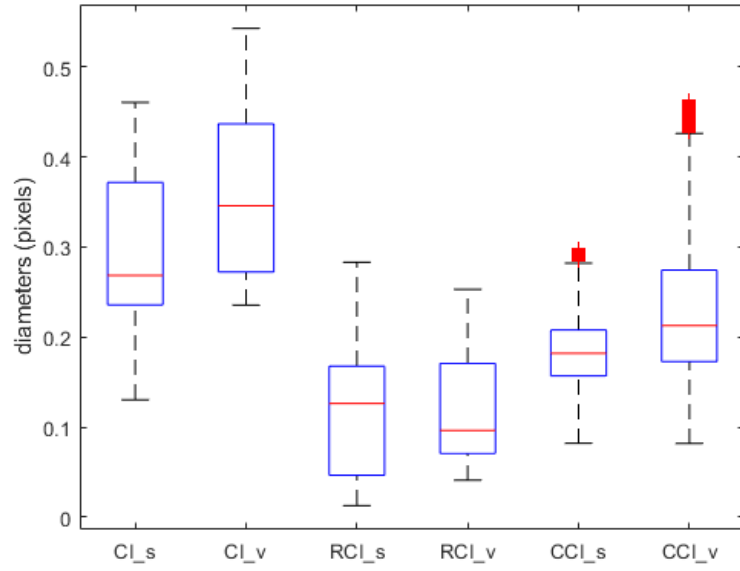
Figure 3.56: Subject 3, transverse plane, boxplots of CI,RCI and CCI obtained with speckle tracking and viper
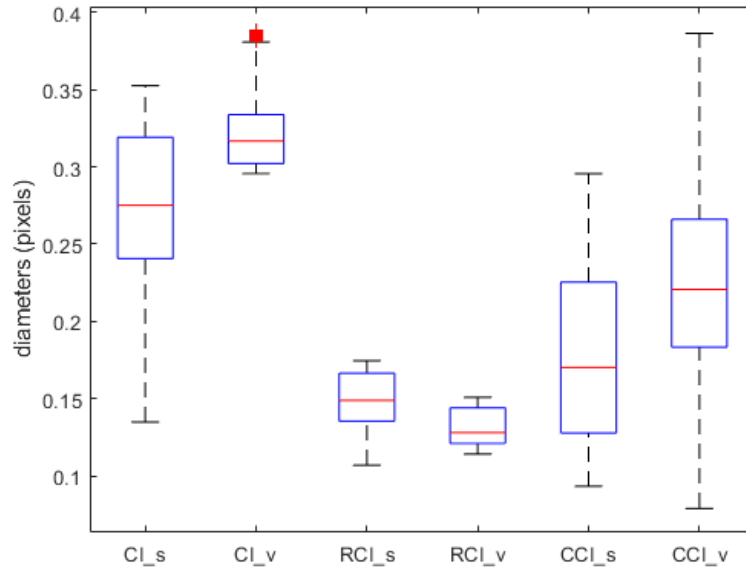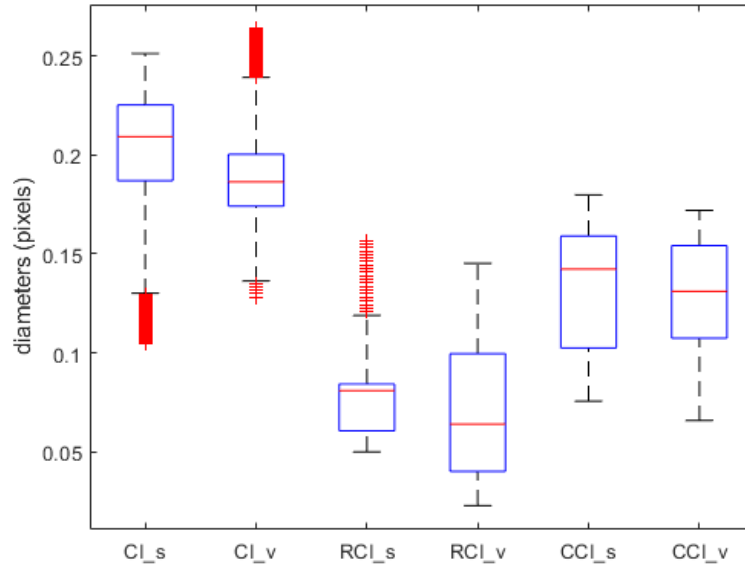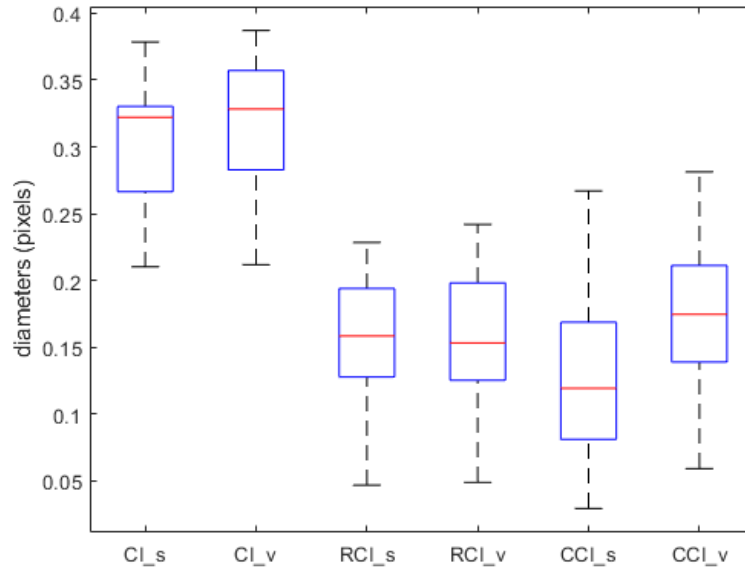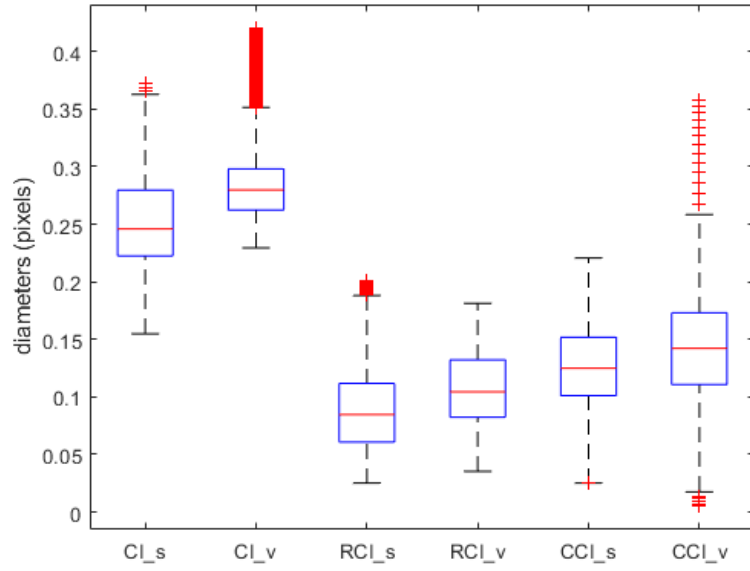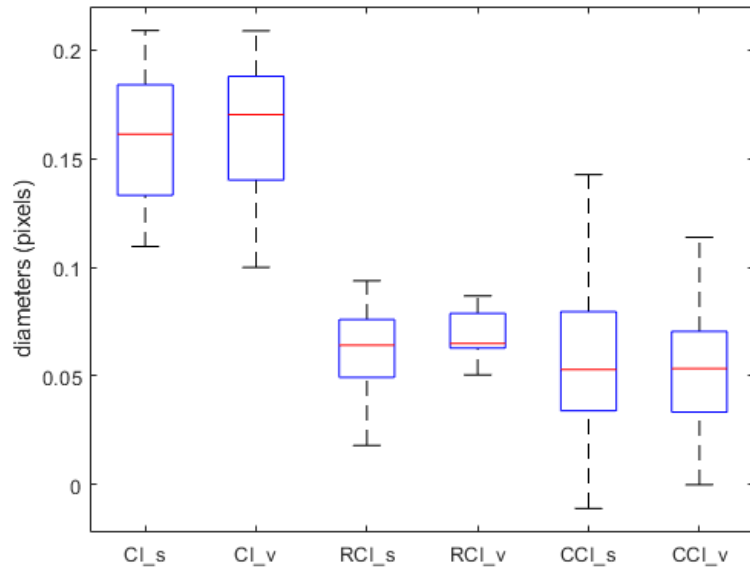

Figure 3.57: Subject 4,transverse plane, boxplots of CI,RCI and CCI obtained with speckle tracking and viper

Figure 3.58: Subject 5, transverse plane, boxplots of CI,RCI and CCI obtained with speckle tracking and viper

Figure 3.59: Subject 6,transverse plane, boxplots of CI,RCI and CCI obtained with speckle tracking and viper

67

Figure 3.60: Subject 7, transverse plane, boxplots of CI,RCI and CCI obtained with speckle tracking and viper

Figure 3.61: Subject 8,transverse plane, boxplots of CI,RCI and CCI obtained with speckle tracking and viper

3.7 Performances at different frame rates, transverse plane

Generally speaking, also in the case of the transverse plane, the speckle tracking algorithm presents an error between the original acquisition and the simulated ones at lower frame rate. The error generally increases as the frame rate of the simulated acquisition is lowered. It should be noted that on a particular subject the tracking is lost at 10 fps and 5 fps. This greatly affected the global mean of all subjects for the acquisitions at 10 fps and 5 fps. However, even without considering the subject where the tracking is lost, it seems that the errors would be globally higher on the case of the longitudinal algorithm, for 15, 10 and 5 fps simulated acquisitions. This could be due to the fact that the realignment corresponding to the first frame is not used in the case of the speckle tracking of the transverse plane. It is also possible to notice that the mean error for the various caval indexes increases in a considerable manner (around 5% or more) for the acquisition simulated at 10 fps compared to the one simulated at 15 fps. It is also possible to notice that the parameter with the highest error, for both simulated acquisition is the CCI. This is not surprinsing, since the cardia caval index is tied to the more abrupt displacements, which can be missed more easily if the frame rate is reduced. It is also possible to notice, that for the mean diameters, the student test accepts the null hypothesis much more often, especially on frame rates lower than 15. This could indicate that the results are less biased compared to the ones found on the longitudinal plane. It is also possible to notice that the subjects with the highest general errors were the one with the less clean acquisitions (subject 5) or the ones with abrupt displacements of the vein (subject 7).

		Frame rate		
		15	10	5
Subject 1	T-test	1	1	1
	Mean Error	0.0348	0.0584	0.0326
	Std Error	0.0233	0.0338	0.0257
Subject 2	T-test	0	0	0
	Mean Error	0.0257	0.0334	0.0421
	Std Error	0.0153	0.0220	0.0362
Subject 3	T-test	0	0	1
	Mean Error	0.0416	0.0473	0.0842
	Std Error	0.0276	0.0339	0.0656
Subject 4	T-test	0	0	0
	Mean Error	0.0447	0.0422	0.0482
	Std Error	0.0553	0.0389	0.0398
Subject 5	T-test	1	1	1
	Mean Error	0.0525	0.0840	0.0666
	Std Error	0.0554	0.0538	0.0553
Subject 6	T-test	1	0	0
	Mean Error	0.0571	0.0429	0.0602
	Std Error	0.0507	0.0338	0.0494
Subject 7	T-test	1	1	1
	Mean Error	0.0949	1.7128	2.5453
	Std Error	0.0761	1.5203	1.4237
Subject 8	T-test	0	1	1
	Mean Error	0.0223	0.0455	0.0498
	Std Error	0.0187	0.0404	0.0441
Mean	T-test	-	-	-
	Mean Error	0.0467	0.2583	0.3661
	Std Error	0.0403	0.2221	0.2175

Table 3.8: Table with the comparison between the diameters of the original acquisition and the various simulations at lower fps,transverse plane. A 0 in the T-test means that the null hypothesis was accepted, a 1 means that the hypothesis was rejected.
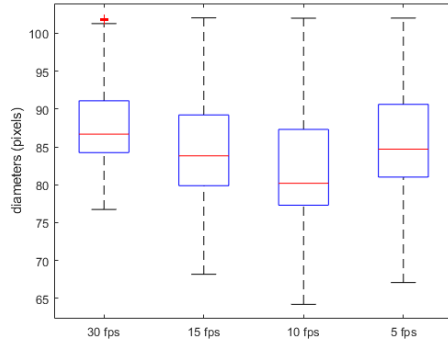
Figure 3.62: Subject 1, transverse plane box-plots of mean diameters on 30,15,10 and 5 fps
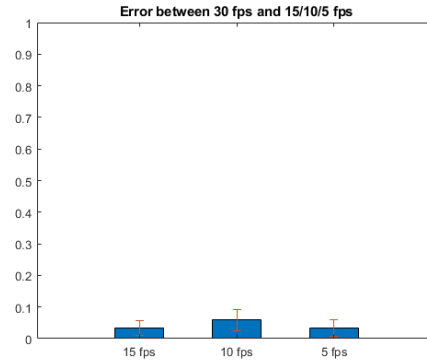
Figure 3.63: Subject 1, transverse plane errors between original acquisition and simulated lower frame rates
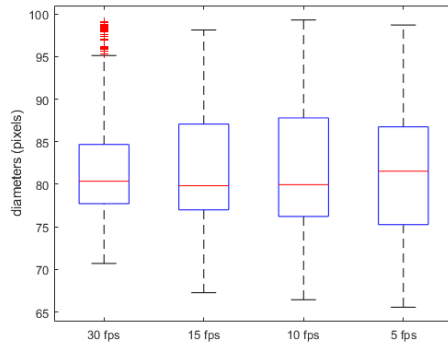
Figure 3.64: Subject 2, transverse plane box-plots of mean diameters on 30,15,10 and 5 fps
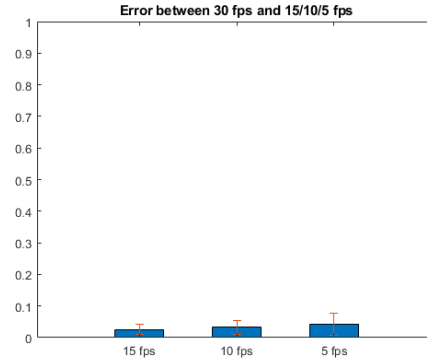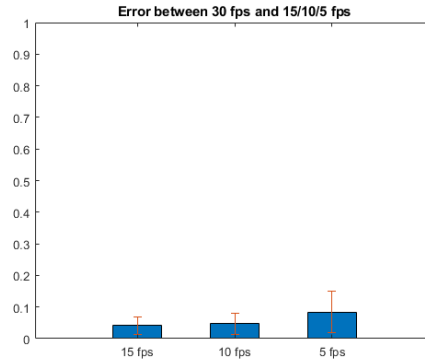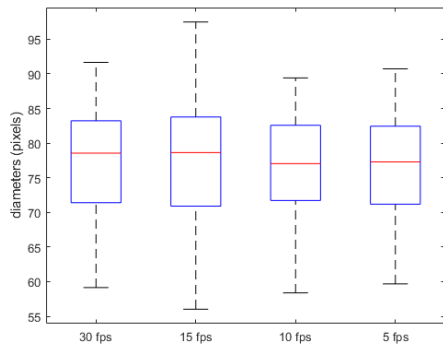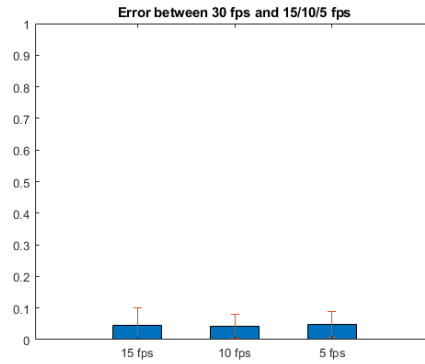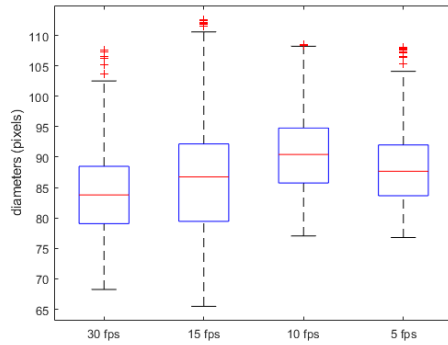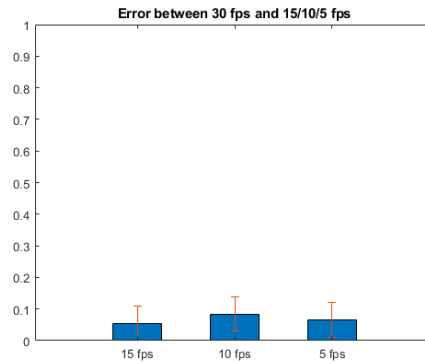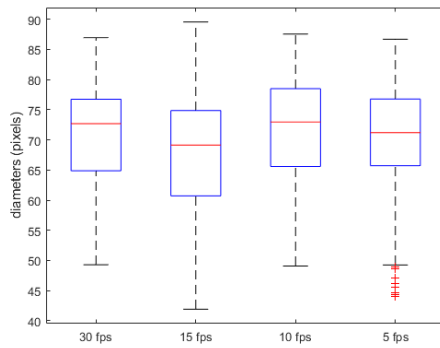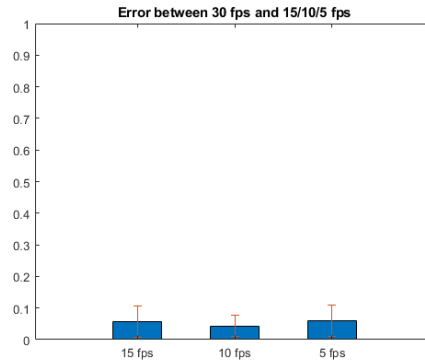

Figure 3.65: Subject 2, transverse plane errors between original acquisition and simulated lower frame rates
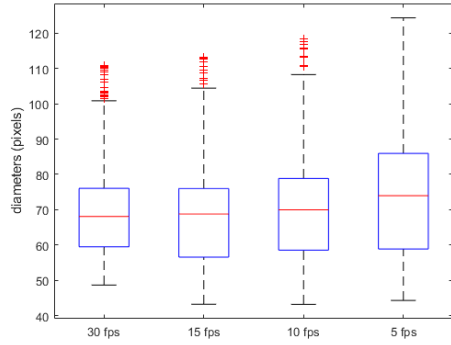
Figure 3.66: Subject 3, transverse plane boxplots of mean diameters on 30,15,10 and 5 fps

Figure 3.67: Subject 3, transverse plane errors between original acquisition and simulated lower frame rates
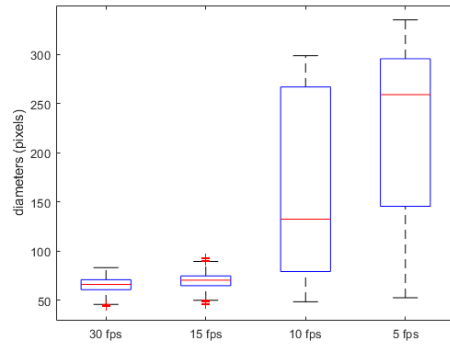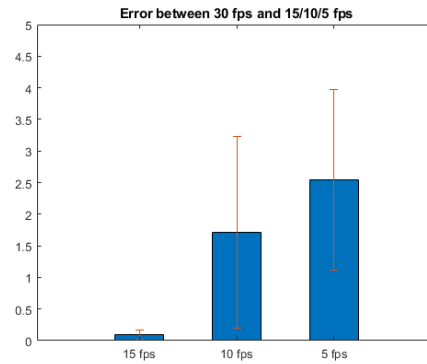

Figure 3.68: Subject 4, transverse plane boxplots of mean diameters on 30,15,10 and 5 fps

Figure 3.69: Subject 4, transverse plane errors between original acquisition and simulated lower frame rates

Figure 3.70: Subject 5, transverse plane box-plots of mean diameters on 30,15,10 and 5 fps

Figure 3.71: Subject 5, transverse plane errors between original acquisition and simulated lower frame rates
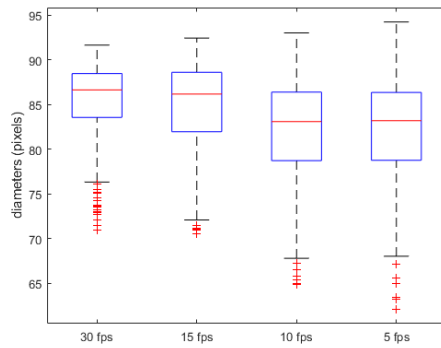

Figure 3.72: Subject 6, transverse plane box-plots of mean diameters on 30,15,10 and 5 fps
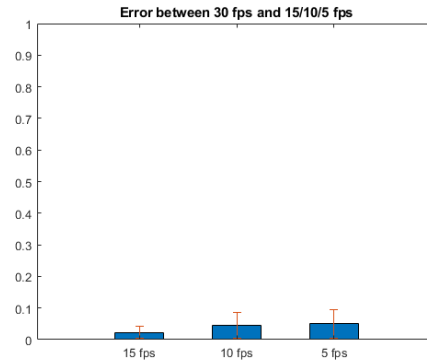

Figure 3.73: Subject 6, transverse plane errors between original acquisition and simulated lower frame rates

Figure 3.75: Subject 7, transverse plane errors between original acquisition and simulated lower frame rates

Figure 3.74: Subject 7, transverse plane boxplots of mean diameters on 30,15,10 and 5 fps

Figure 3.77: Subject 8, transverse plane errors between original acquisition and simulated lower frame rates

Figure 3.76: Subject 8, transverse plane boxplots of mean diameters on 30,15,10 and 5 fps

74

		Frame rate		
		CI	RCI	CCI
Subject 1	T-test-15 fps	0	1	1
	Error 15 fps	0.0175	0.3549	0.1234
	T-test 10 fps	1	1	1
	Error 10 fps	0.1359	0.3988	0.1182
Subject 2	T-test-15 fps	1	1	0
	Error 15 fps	0.0666	0.1459	0.0155
	T-test 10 fps	1	1	0
	Error 10 fps	0.0547	0.1080	0.0105
Subject 3	T-test-15 fps	1	0	0
	Error 15 fps	0.0772	0.0030	0.0128
	T-test 10 fps	1	0	0
	Error 10 fps	0.0465	0.0843	0.0011
Subject 4	T-test-15 fps	1	0	1
	Error 15 fps	0.1333	0.0023	0.1154
	T-test 10 fps	0	0	1
	Error 10 fps	0.0085	0.0038	0.1912
Subject 5	T-test-15 fps	0	0	1
	Error 15 fps	0.0277	0.0048	0.1240
	T-test 10 fps	0	1	1
	Error 10 fps	0.0198	0.2150	0.1620
Subject 6	T-test-15 fps	1	1	1
	Error 15 fps	0.1277	0.2291	0.1281
	T-test 10 fps	1	1	1
	Error 10 fps	0.0814	0.0502	0.1821
Subject 7	T-test-15 fps	0	1	1
	Error 15 fps	0.0077	0.1354	0.0480
	T-test 10 fps	1	1	1
	Error 10 fps	0.4193	0.4178	0.5623
Subject 8	T-test-15 fps	1	1	1
	Error 15 fps	0.0810	0.0786	0.8539
	T-test 10 fps	1	1	1
	Error 10 fps	0.1409	0.2260	0.7504
Mean	Error 15 fps	0.0673	0.1193	0.1776
	Error 10 fps	0.1134	0.1880	0.2472

Table 3.9: Table with the comparison between the caval indexes of the original acquisition and the various simulations at lower fps, transverse plane. A 0 in the T-test means that the null hypothesis was accepted, a 1 means that the hypothesis was rejected.

3.8 General comparison between speckle tracking and viper algorithm

In this section a general comparison between the two algorithms highlighting pros and cons of both will be done. For the longitudinal plane it seems that the speckle tracking and the viper algorithms can sometimes have a quite different behavior. For instance, on some subjects the comparison was not possible because the two algorithms could not track the same portion of the borders of the vena cava. This can be interesting, since they can sometimes complement each others and extract information of more sections of the vessel. It should be noted that an advantage of the viper on the longitudinal plane is that the algorithm is more reactive to adjust to the borders compared to the speckle tracking. On the other hand, the speckle tracking for some subjects managed to be more stable compared to the viper: for instance, on subject 7 for the longitudinal plane, to whole tracking had to be done in four parts, because at some points the viper lost the borders. The speckle algorithm, managed to track the acquisition in two parts only. This is probably due to the fact that at some points of the video, high noise inside the vein appeared, thus generating problems for the viper algorithm, which follows the displacements with the gradient. Also, from the personal point of view of the graduate student, sometimes it is difficult to place the reference points of the viper to obtain optimal results, thus in some cases the initialisation with the speckle algorithm was easier. However, it should be noted that this consideration is biased: the graduate student has used the viper algorithm much less than the speckle one. Also, he has written the code for the speckle algorithm, so he knows the weak points of it and thus it is easier for him to select the ideal borders of the vein. For another user the situation could probably be reversed. For what concerns the transverse plane, it seems that the viper algorithm performs generally better than the speckle one: it is easier to initialize, since only the point at the center of the vena cava is required, while for the speckle the user should place the points on the borders which are later fitted on an ellipse. Also, the viper algorithm does not have a shape fitted to an ellipse, so it can follow more easily the borders of vessel assuming more complex shapes. Finally, of the eight subject tested on the transverse plane, both the viper and the speckle algorithm lost track on one video. But the viper algorithm lost track of the subject around 300 frames after the speckle one. So, for the both the transverse and longitudinal planes, the speckle tracking algorithm seems to be less reactive than the viper one to follow the borders of the vein. For what concerns the stability, the viper is more stable on the transverse plane, while on the longitudinal plane it depends on the subject, in some cases there are better performances for the speckle. Finally, for the longitudinal plane, the speckle algorithm has an execution speed of around 180 ms per frame by tracking 42 points. On the other hand, the viper algorithm has an execution speed of around 150 ms for the longitudinal plane. For the transverse plane, the speckle algorithm has an execution speed of around 120 ms, by tracking 12 points. On the other hand, the viper algorithm has an execution speed of 130 ms on the transverse plane. So, the two algorithms seem to have comparable speed of execution.

3.9 Case study: patients with pulmonary diseases

Finally, it was possible to begin a study on some patients with pulmonary diseases. Due to some delays caused by the covid-19 pandemic, only the data of four patients (patient b,f,m and g) has been collected. This data was processed with both the viper and the speckle tracking algorithm, when possible. When it was not possible, only an algorithm was used. For the longitudinal planes,

the processing was possible with both the algorithms for the four patients On the other hand, for the transverse plane, the patient b could not be processed with any algorithm, due to the echography having a lot of noise and the vena cava being too little. The patient f could be processed only with the speckle tracking algorithm, because sometimes the vena cava seemed to disappear, and the tracking was lost with the viper algorithm, his reactivity in this case seemed to be a double edged sword. And patient m and g could be processed only with the viper algorithm, this because the speckle algorithm was following too slowly the borders of the diameters for the processing to be valid.

		Caval index		
		CI	RCI	CCI
patient b, viper	Transv mean	-	-	-
	Transv std	-	-	-
	Long mean	0.3283	0.1783	0.2608
	Long std	0.0765	0.0565	0.0659
patient b, speckle	Transv mean	-	-	-
	Transv std	-	-	-
	Long mean	0.1324	0.0422	0.0838
	Long std	0.0191	0.0152	0.0262
patient f, viper	Transv mean	-	-	-
	Transv std	-	-	-
	Long mean	0.2141	0.0547	0.1821
	Long std	0.0312	0.0162	0.0196
patient f, speckle	Transv mean	0.1467	0.0361	0.1040
	Transv std	0.0109	0.0090	0.0285
	Long mean	0.1008	0.0239	0.0741
	Long std	0.0107	0.0096	0.0116
patient m, viper	Transv mean	0.1595	0.0680	0.1134
	Transv std	0.0229	0.0439	0.0176
	Long mean	0.1760	0.0675	0.1171
	Long std	0.0148	0.0100	0.0168
patient m, speckle	Transv mean	-	-	-
	Transv std	-	-	-
	Long mean	0.1581	0.0749	0.0997
	Long std	0.0105	0.0227	0.0184
patient g, viper	Transv mean	0.1111	0.0702	0.0701
	Transv std	0.0480	0.0340	0.0316
	Long mean	0.2174	0.0927	0.1587
	Long std	0.0664	0.0262	0.0459
patient g, speckle	Transv mean	-	-	-
	Transv std	-	-	-
	Long mean	0.1605	0.0714	0.0951
	Long std	0.0320	0.0218	0.0281

Table 3.10: Table with the comparison between the original acquisition and the various simulations at lower fps. A 0 in the T-test means that the null hypothesis was accepted, a 1 means that the hypothesis was rejected.

What can easily be noticed is that the mean RCI for each patient, for both algorithms and for both planes, is always lower than the CCI, with the exception of the patient g on the transverse plane. This is not surprising, and seems to agree with the hypothesis that people presenting respiratory diseases present low variations of the diameter of the inferior vena cava due to lower variations of the various pulmonary pressures. However it is not possible to make such a conclusion since the data of only three patients is available, which is not a statistically significant number. Furthermore, the graduate student does not know specifically which disease has each patient, since the physicians who collected the data considered that a blind study would be more valuable.

Chapter 4

Conclusion

The main objective of this master thesis was to develop an algorithm to track the displacements of the inferior vena cava on the longitudinal and transverse plane using the speckle tracking technique, and to compare the results with an already existing algorithm. The comparison between the results was firstly done on the obtained mean diameters on each frame. For the longitudinal plane, the mean error between the viper and speckle algorithm was of 4.39% and the mean number of points inside the bland altman graph confidence interval was of 94.57%. The low value of the error shows a general low bias, and the percentage of points close to 95 seems to suggest that to evaluate to diameters on the longitudinal plane those two methods are quite similar. However, those results are based on an average of only five subjects, which is not a statistically significant number, on a larger population it is entirely possible that those results could change drastically. Also, it should be noted that a relatively low error on the mean diameters causes a much greater bias on the indexes estimating the pulsatility: the errors were of 16.98%, 29.35% and 15.81% for the CI, RCI and CCI respectively, which seem to be quite significant values. For the transverse plane, the mean error for the diameters was of 6.64%, and the percentage of points inside the confidence interval of the bland altman plot was of 94.49%. Again those two values seem to suggest that the two methods would be interchangeable, but the low error on the diameters causes again a greater bias on the pulsatility indexes: 9.24%, 17.85% and 16.11% for the CI, RCI and CCI respectively. It seems however that the bias is generally lower for the pulsatility indexes on the transverse plane. It should be noted that to really confirm if the two methods could be interchangeable or not it would be necessary to understand how much a bias on the pulsatility would be impactful for the diagnosis on some patients. It could vary depending on the final application, which this thesis do not cover. Also, the speckle algorithm was tested with some simulations at different frame rates, by simulating different acquisitions of 15, 10 and 5 fps. In this case, the references were the original echographies at 30 fps. Unsurprisingly, the bias for the diameters was higher the lower the frame rate got. It seems that this bias, for both the longitudinal and transverse plane becomes much higher when the frame rate passes from 10 to 5 fps compared from when the frame rate passes from 15 to 10 fps. Also, at 10 and 5 fps in some subjects the tracking was lost, although more frequently at 5 fps. The much higher error at five fps could be explained by the fact that some displacements of the vessel are done at the physiological frequency of the heart rate. By having a sampling frequency of 5 Hz, the Nyquist frequency would be of 2.5 Hz, which is in the range of the aforementioned heart rate, so some more abrupt displacements can be lost more easily. Finally,the

case study of the three patients with pulmonary diseases seems to suggest that the rigidity of the vessel is mostly due to low variation of the pulmonary pressure, since the RCI is always considerably lower than the CCI. For what concerns future developments, it is possible to say that the algorithm could be improved in different manners. For the execution speed, it would be interesting to see if there would be improvements by using the optimized lewis cross correlation algorithm, where the numerator of the normalized cross correlation is calculated in the frequency domain. It is not certain if there would be improvements, since the calculation of the convolution in the frequency domain is faster than the one calculated normally only if the window reaches a certain dimension, for smaller windows the regular method performs better. Also, it would be possible to try out the other two method generally used for the block matching algorithm: the sum of squared differences and the sum of absolute differences. Those two methods are much faster than the normalized cross correlation but are less robust, but it could be worth to try to see if they are robust enough for this specific application. For what concerns the robustness of the algorithm, probably the best way to improve it would be to use the some more refined edge rendering technique: for the algorithm on the longitudinal plane the sobel filtering was used only vertically and only for the upper border of the vein and it was used just if certain condition were met, while for the transverse algorithm no techniques based on the image gradient were used. Finally, some tuning to optimise the parameters of the algorithms such as the size of the windows and the number of points could be done to see if there would be any improvements in terms of robustness and computational speed.

Appendix A

Bland Altman plots, longitudinal plane
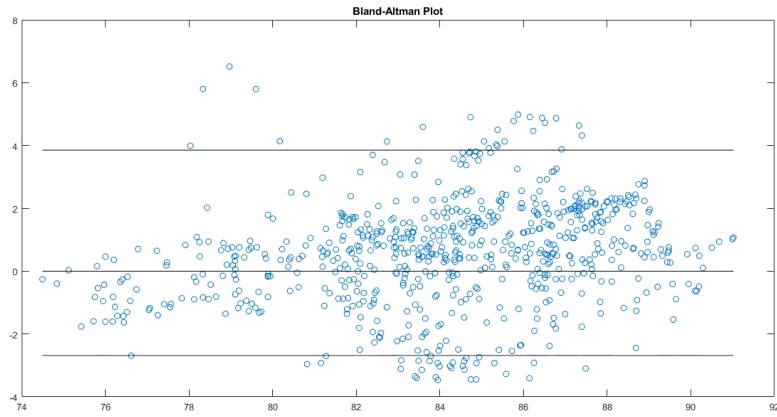
Figure A.1: Subject 2, Bland-altman plot of the diameters obtained with the two algorithms
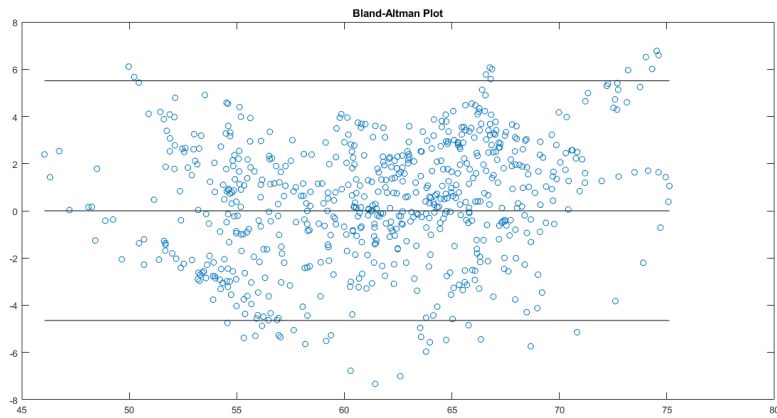
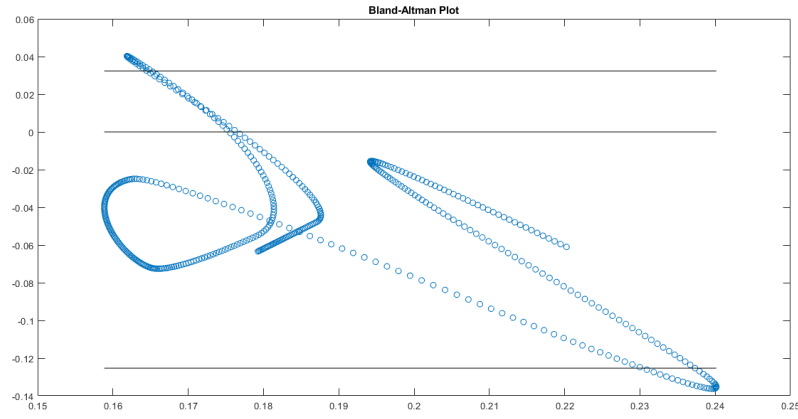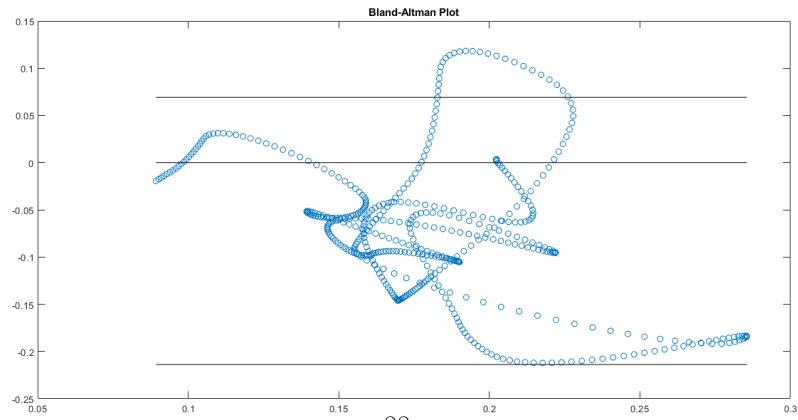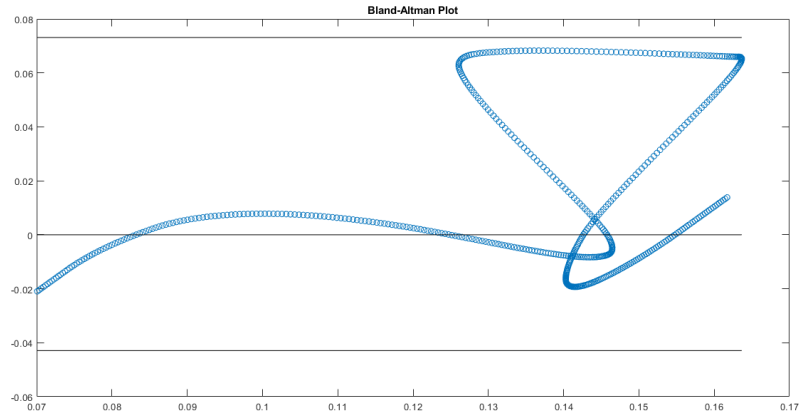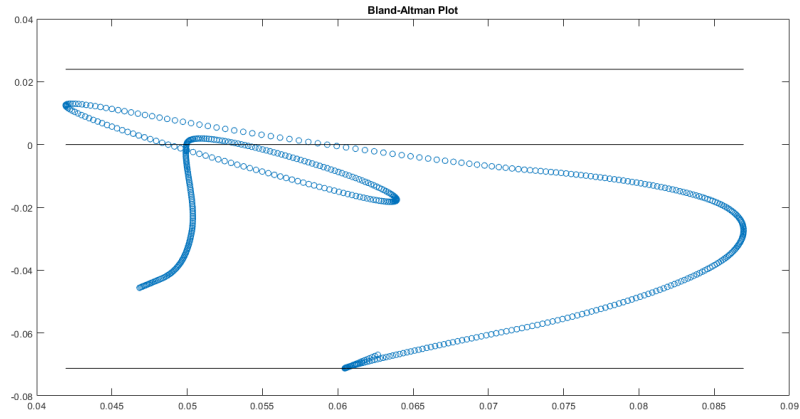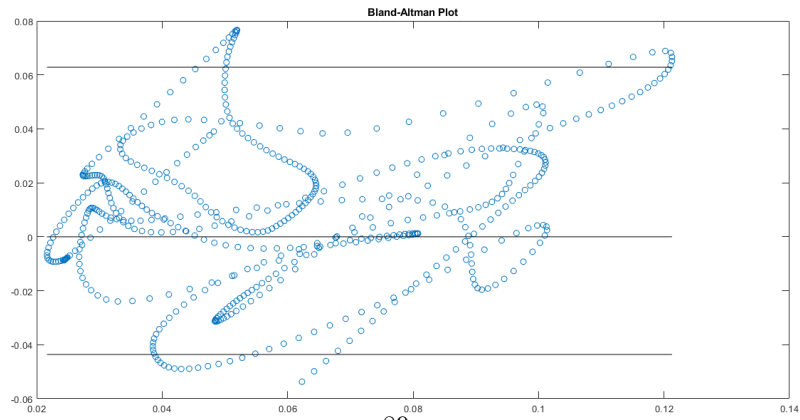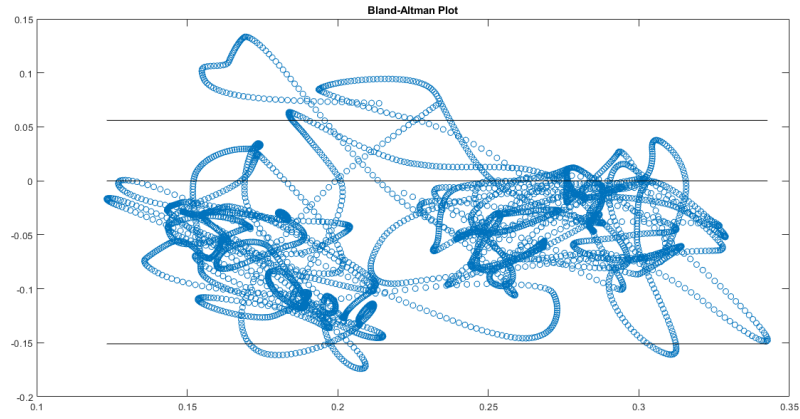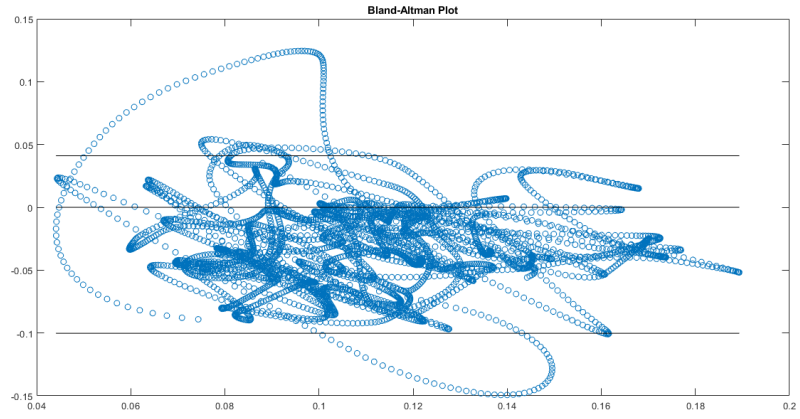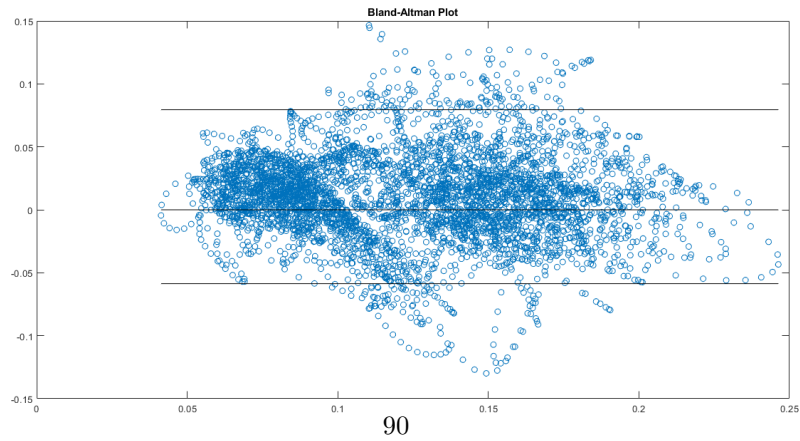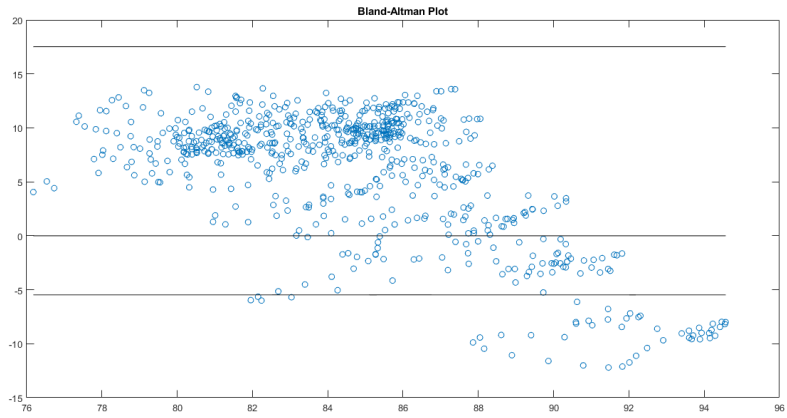Figure A.2: Subject 4, Bland-altman plot of the diameters obtained with the two algorithms

83
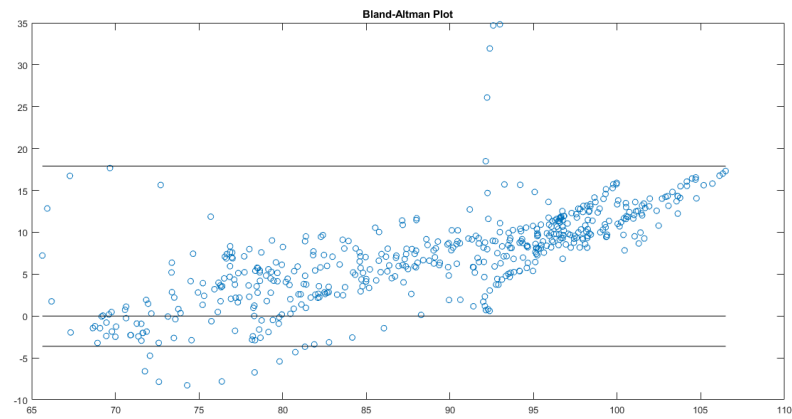
Figure A.3: Subject 5, Bland-altman plot of the diameters obtained with the two algorithms
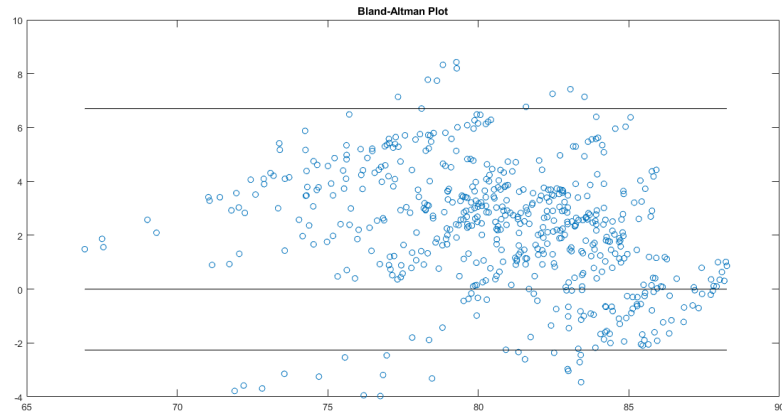
Figure A.4: Subject 6, Bland-altmann plot of the diameters obtained with the two algorithms
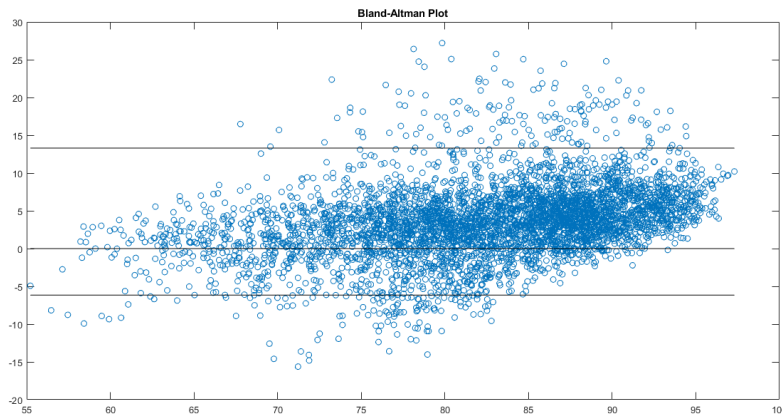
Figure A.5: Subject 9, Bland-altmann plot of the diameters obtained with the two algorithms
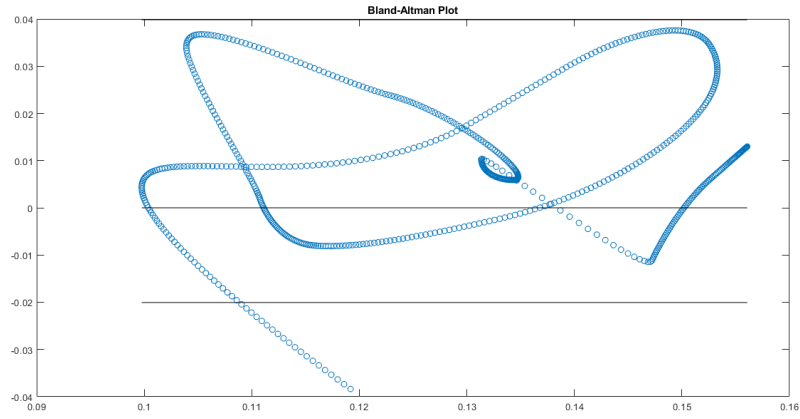
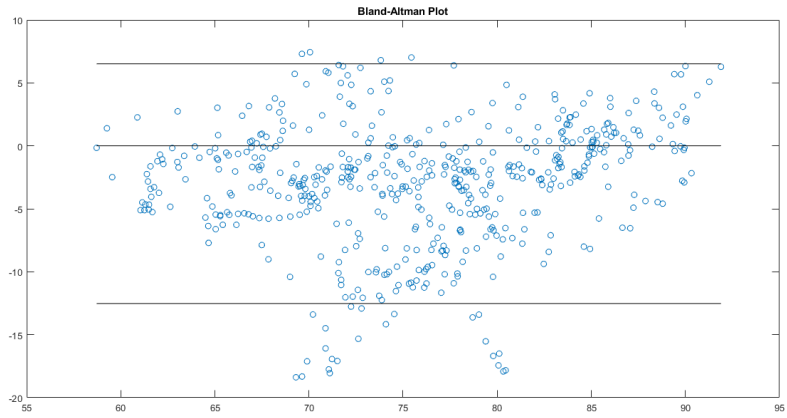Figure A.6: Subject 2, Bland-altmann plot of the CI obtained with the two algorithms
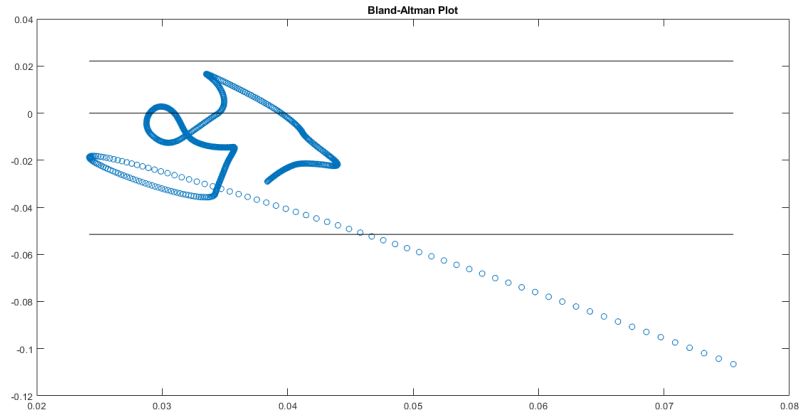
Figure A.7: Subject 2, Bland-altmann plot of the RCI obtained with the two algorithms

86
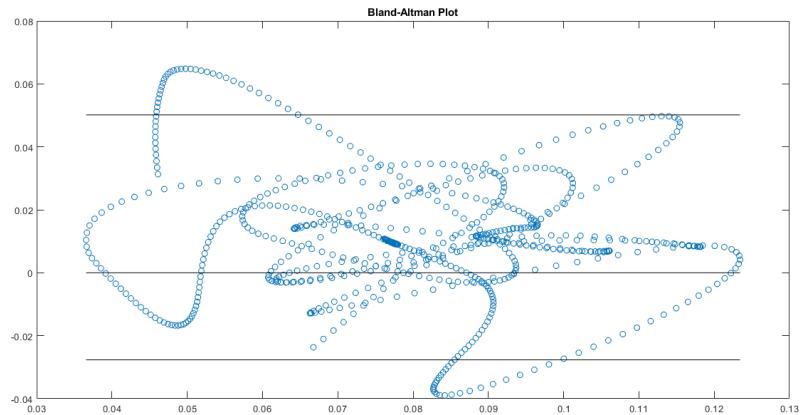
Figure A.8: Subject 2, Bland-altmann plot of the CCI obtained with the two algorithms
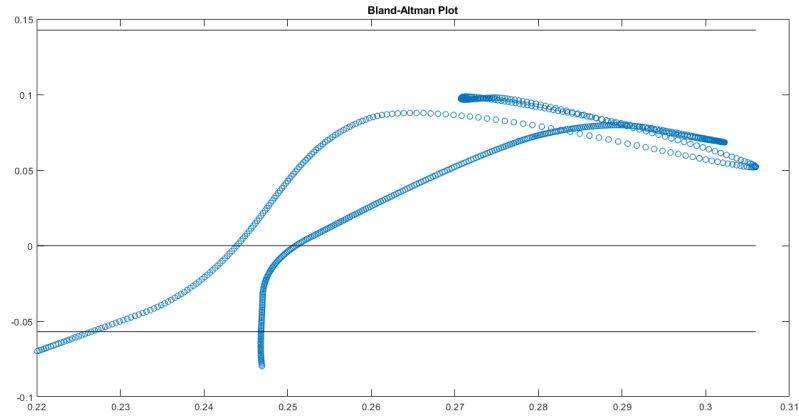
Figure A.9: Subject 4, Bland-altmann plot of the CI obtained with the two algorithms
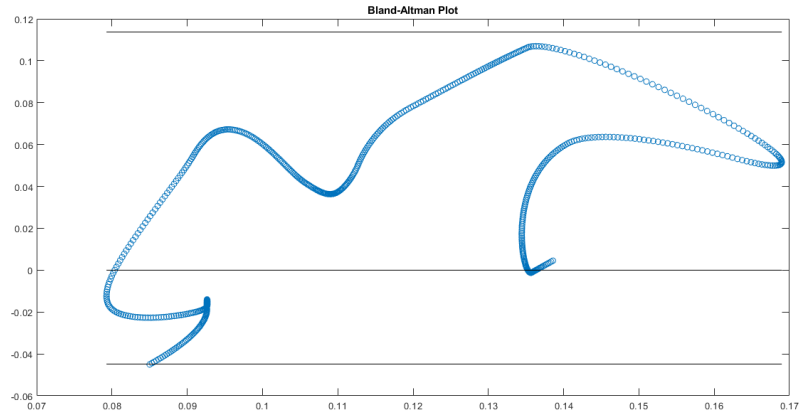
Figure A.10: Subject 4, Bland-altmann plot of the RCI obtained with the two algorithms

87
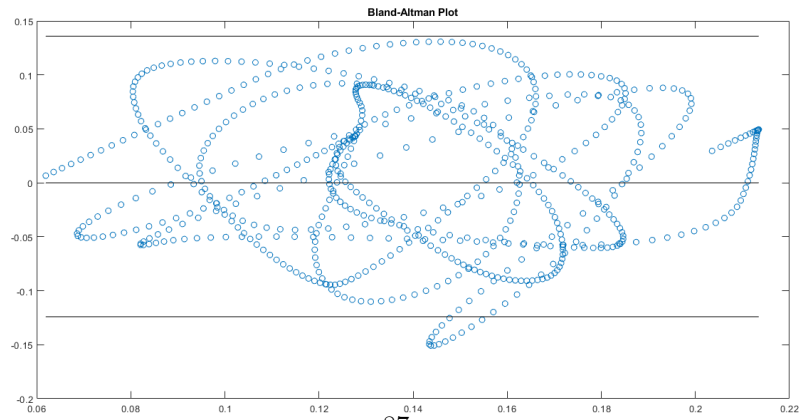
Figure A.11: Subject 4, Bland-altmann plot of the CCI obtained with the two algorithms
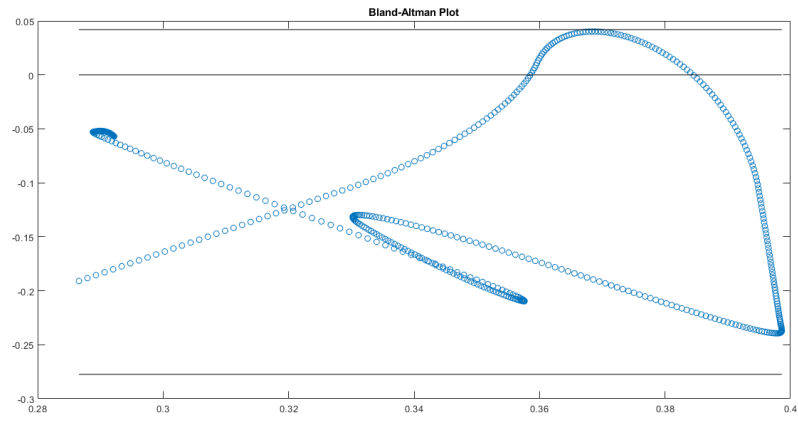
Figure A.12: Subject 5, Bland-altmann plot of the CI obtained with the two algorithms

Figure A.13: Subject 5, Bland-altmann plot of the RCI obtained with the two algorithms

88

Figure A.14: Subject 5, Bland-altmann plot of the CCI obtained with the two algorithms

Figure A.15: Subject 6, Bland-altmann plot of the CI obtained with the two algorithms

Figure A.16: Subject 6, Bland-altmann plot of the RCI obtained with the two algorithms

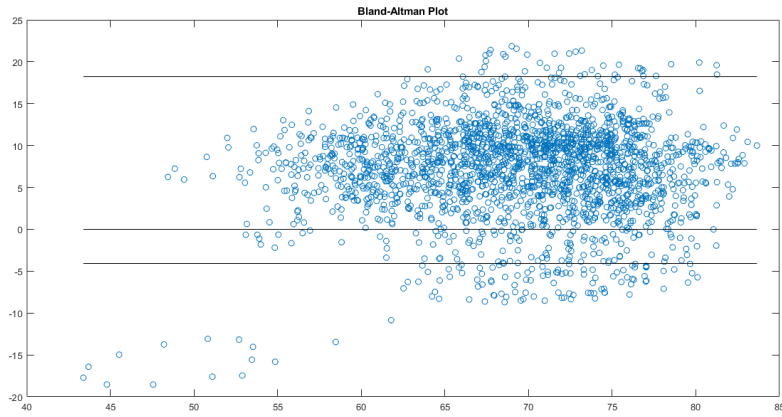Figure A.17: Subject 6, Bland-altmann plot of the CCI obtained with the two algorithms

Figure A.18: Subject 9, Bland-altman plot of the CI obtained with the two algorithms

Figure A.19: Subject 9, Bland-altman plot of the RCI obtained with the two algorithms

Figure A.20: Subject 9, Bland-altman plot of the CCI obtained with the two algorithms
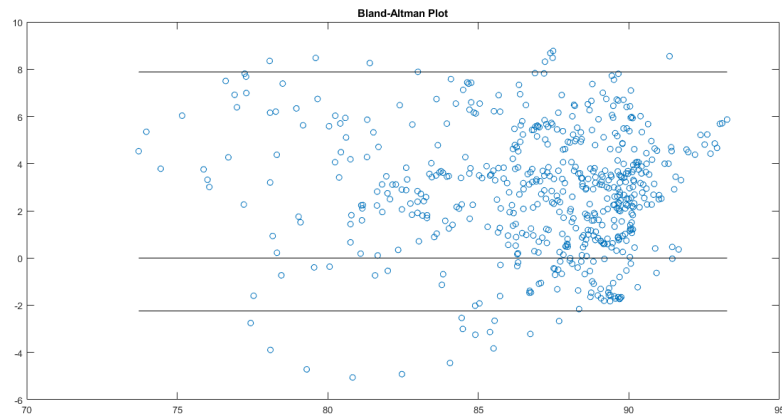
Appendix B

Bland Altman plots, transverse plane
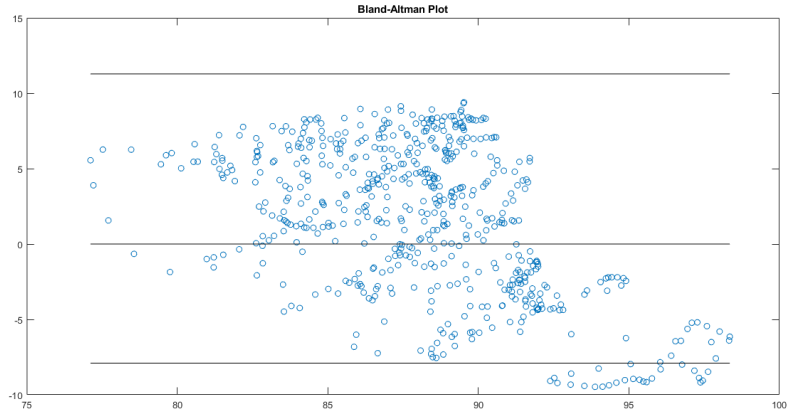
Figure B.1: Subject 1, transverse plane, Bland-altman plot of the diameters obtained with the two algorithms

Figure B.2: Subject 2, transverse plane, Bland-altman plot of the diameters obtained with the two algorithms
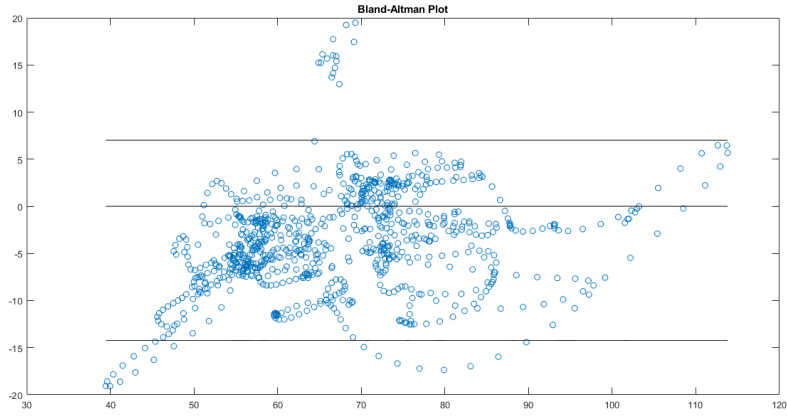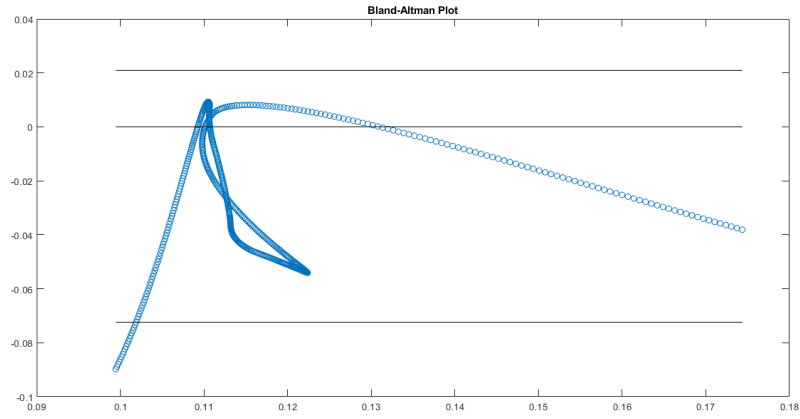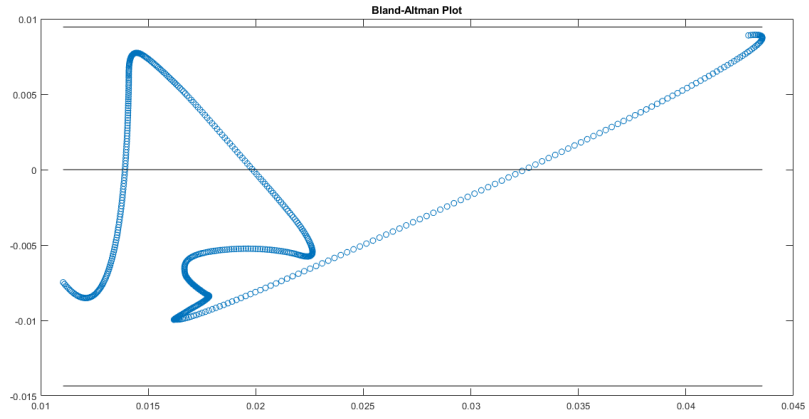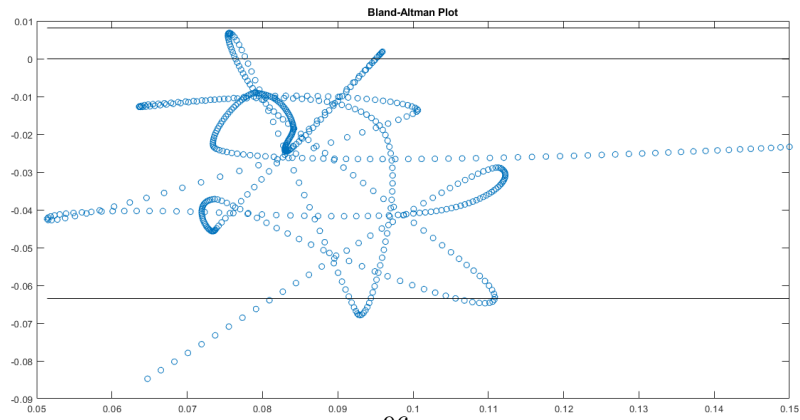
Figure B.3: Subject 3, transverse plane, Bland-altman plot of the diameters obtained with the two algorithms

Figure B.4: Subject 4, transverse plane, Bland-altman plot of the diameters obtained with the two algorithms
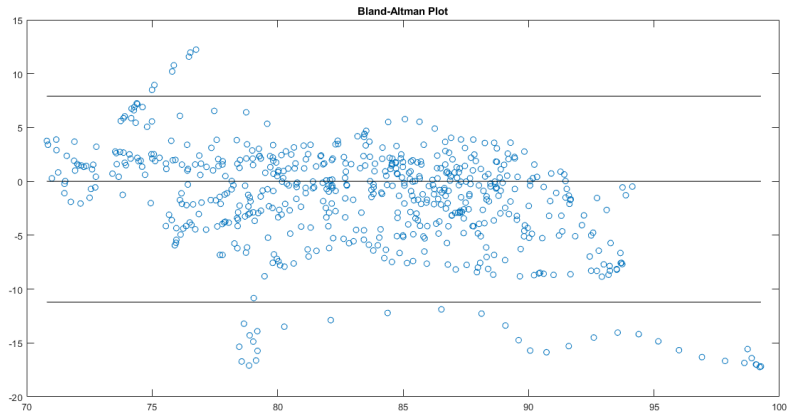
Figure B.5: Subject 5, transverse plane, Bland-altman plot of the diameters obtained with the two algorithms
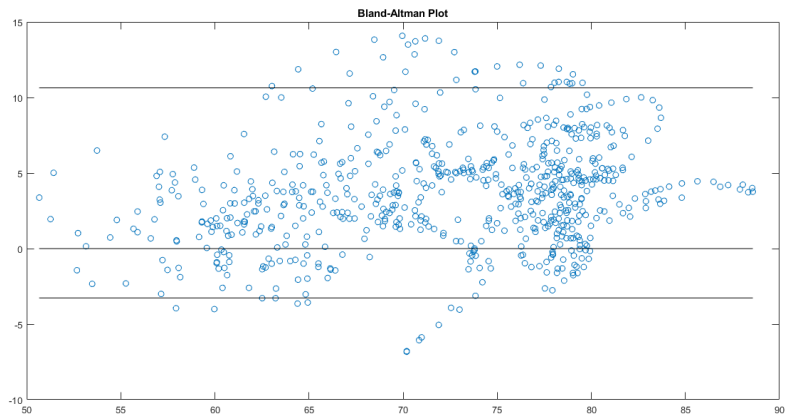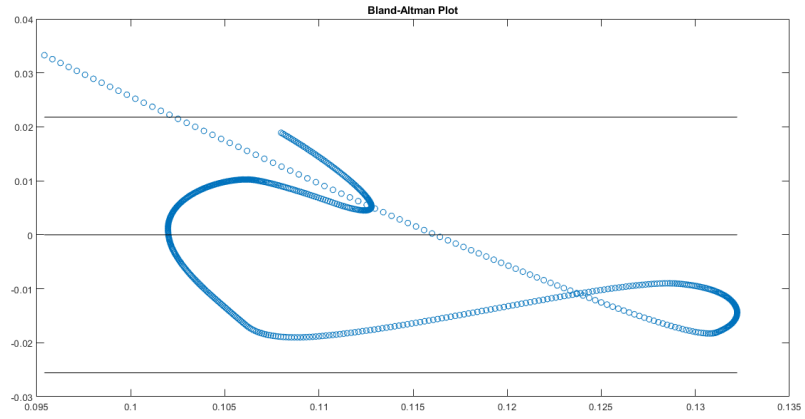

Figure B.6: Subject 6, transverse plane, Bland-altman plot of the diameters obtained with the two algorithms

Figure B.7: Subject 7, transverse plane, Bland-altman plot of the diameters obtained with the two algorithms

Figure B.8: Subject 8, transverse plane, Bland-altman plot of the diameters obtained with the two algorithms

Figure B.9: Subject 1, transverse plane, Bland-altman plot of the CI obtained with the two algorithms

Figure B.10: Subject 1, transverse plane, Bland-altman plot of the RCI obtained with the two algorithms
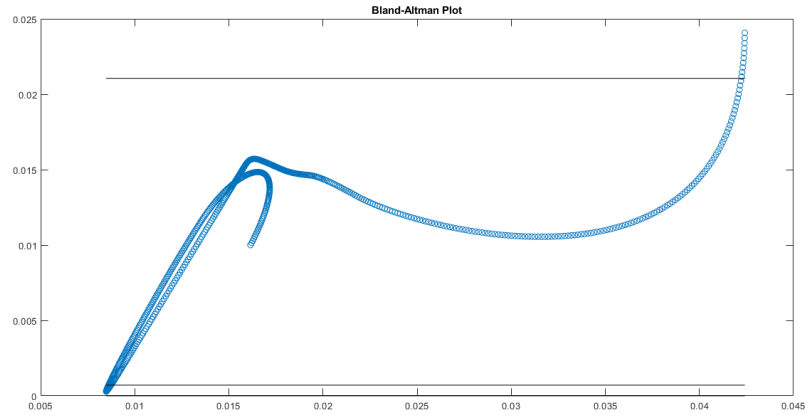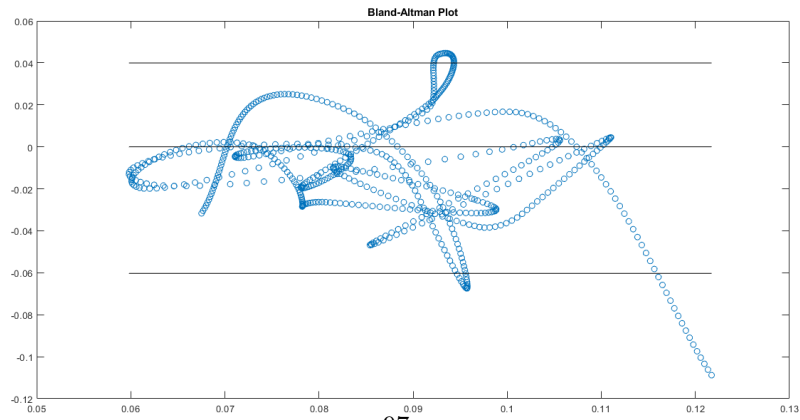
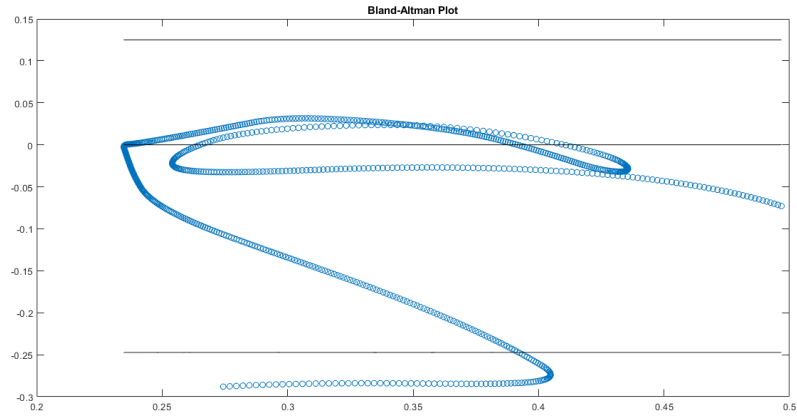Figure B.11: Subject 1, transverse plane Bland-altman plot of the CCI obtained with the two algorithms

Figure B.12: Subject 2, transverse plane, Bland-altman plot of the CI obtained with the two algorithms

Figure B.13: Subject 2, transverse plane, Bland-altman plot of the RCI obtained with the two algorithms

97

Figure B.14: Subject 2, transverse plane Bland-altman plot of the CCI obtained with the two algorithms

Figure B.15: Subject 3, transverse plane, Bland-altman plot of the CI obtained with the two algorithms
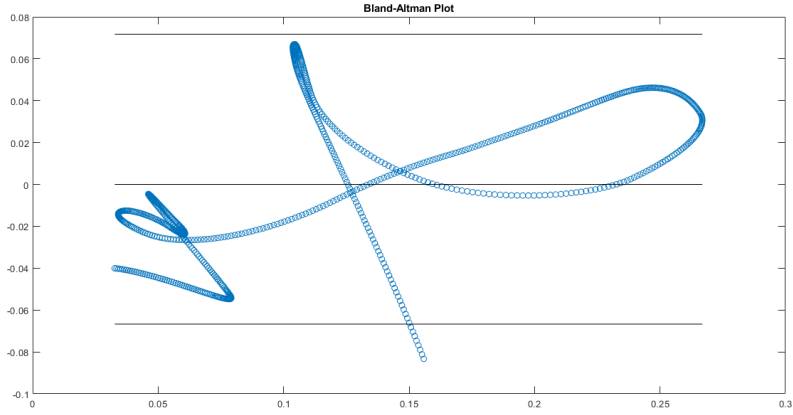

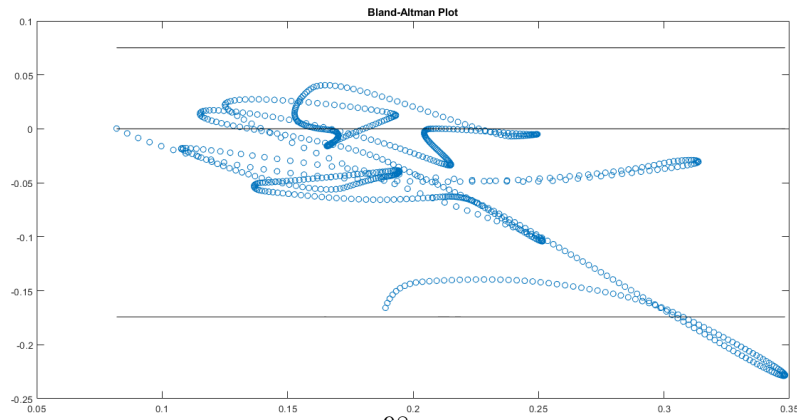Figure B.16: Subject 3, transverse plane, Bland-altman plot of the RCI obtained with the two algorithms   +

Figure B.17: Subject 3, transverse plane Bland-altman plot of the CCI obtained with the two algorithms
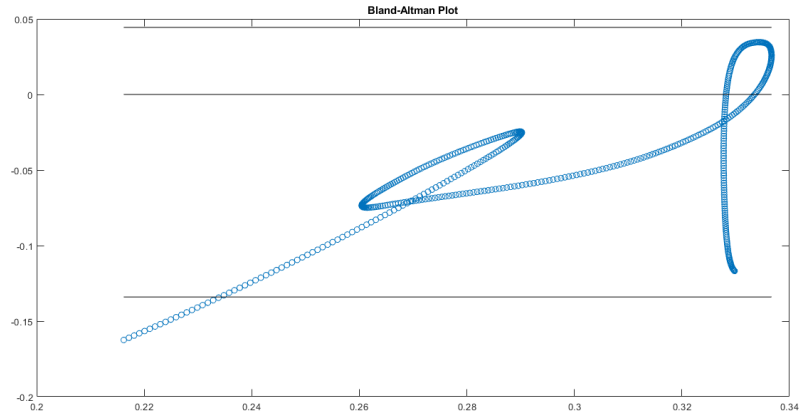
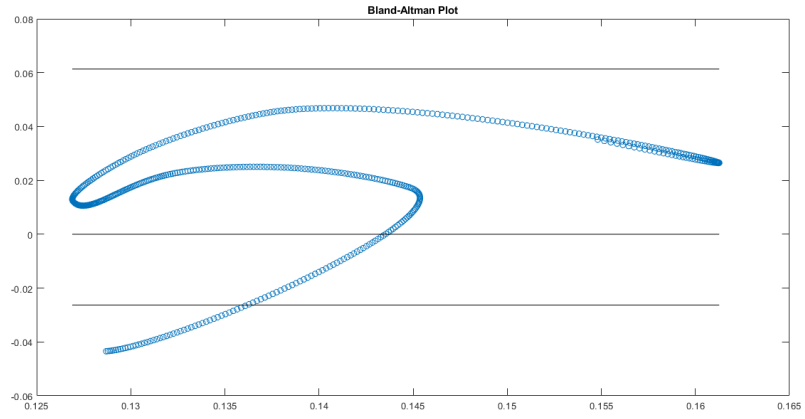Figure B.18: Subject 4, transverse plane, Bland-altman plot of the CI obtained with the two algorithms

Figure B.19: Subject 4, transverse plane, Bland-altman plot of the RCI obtained with the two algorithms
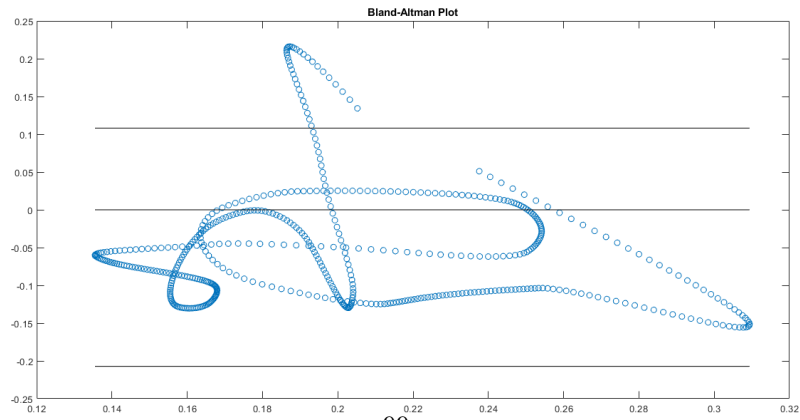
Figure B.20: Subject 4, transverse plane Bland-altman plot of the CCI obtained with the two algorithms

Figure B.21: Subject 5, transverse plane, Bland-altman plot of the CI obtained with the two algorithms

Figure B.22: Subject 5, transverse plane, Bland-altman plot of the RCI obtained with the two algorithms

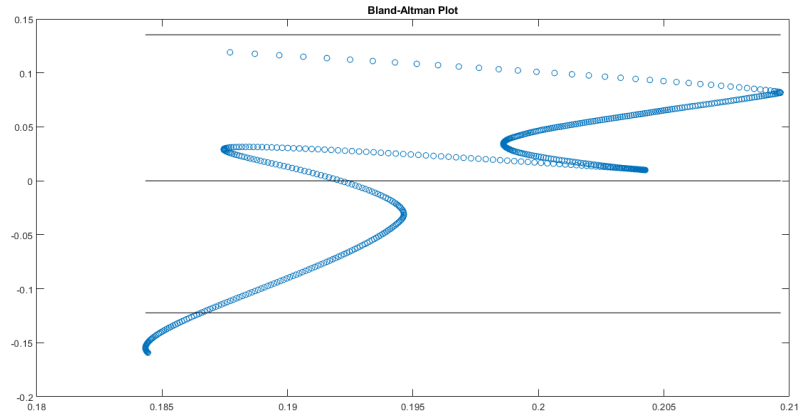Figure B.23: Subject 5, transverse plane Bland-altman plot of the CCI obtained with the two algorithms

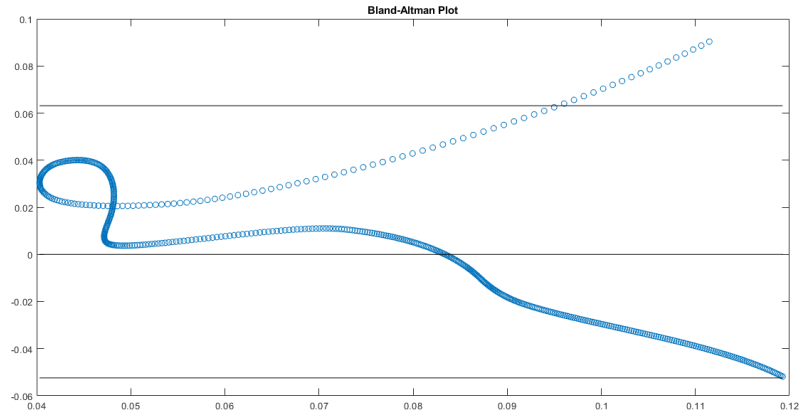Figure B.24: Subject 6, transverse plane, Bland-altman plot of the CI obtained with the two algorithms

Figure B.25: Subject 6, transverse plane, Bland-altman plot of the RCI obtained with the two algorithms

Figure B.26: Subject 6, transverse plane Bland-altman plot of the CCI obtained with the two algorithms

Figure B.27: Subject 7, transverse plane, Bland-altman plot of the CI obtained with the two algorithms

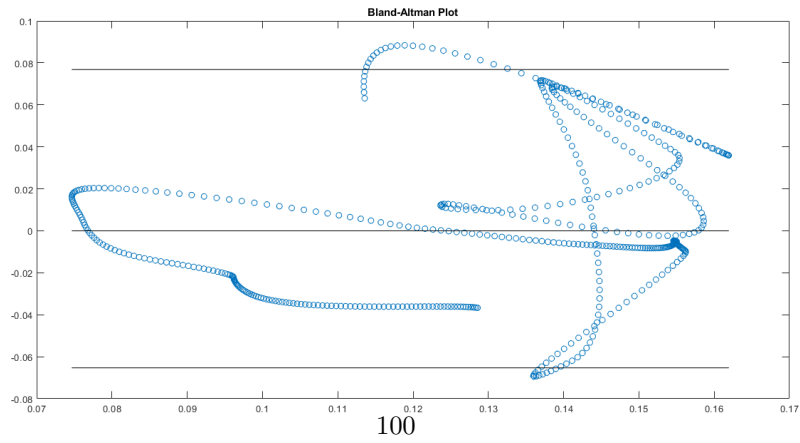Figure B.28: Subject 7, transverse plane, Bland-altman plot of the RCI obtained with the two algorithms   ù

102

Figure B.29: Subject 7, transverse plane Bland-altman plot of the CCI obtained with the two algorithms

Figure B.30: Subject 8, transverse plane, Bland-altman plot of the CI obtained with the two algorithms
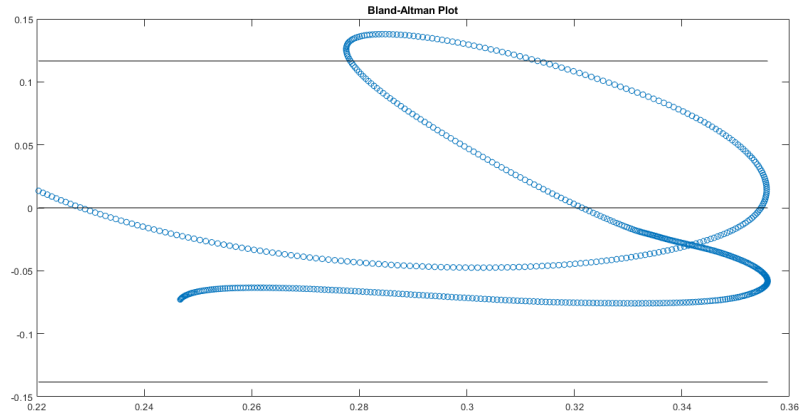

Figure B.31: Subject 8, transverse plane, Bland-altman plot of the RCI obtained with the two algorithms

103

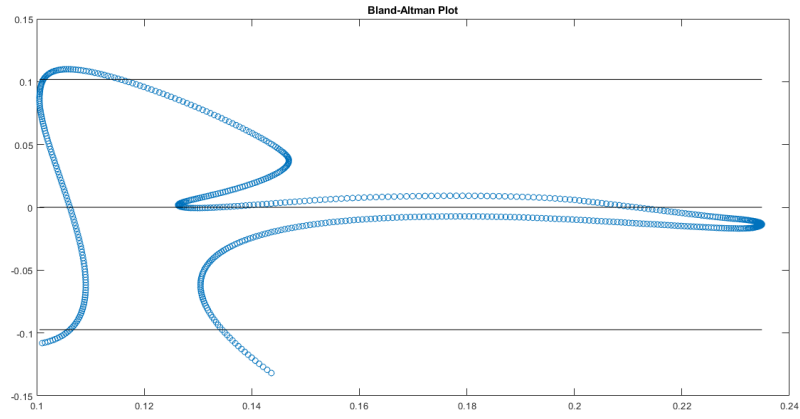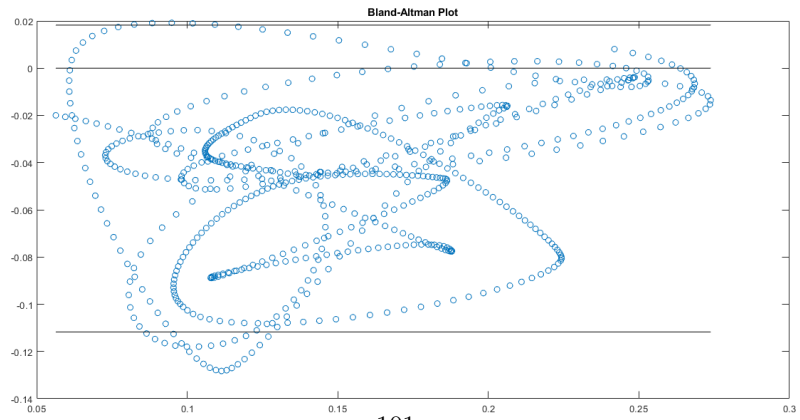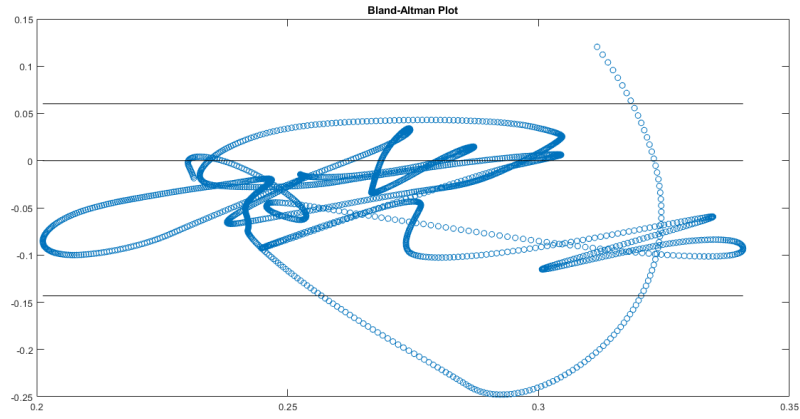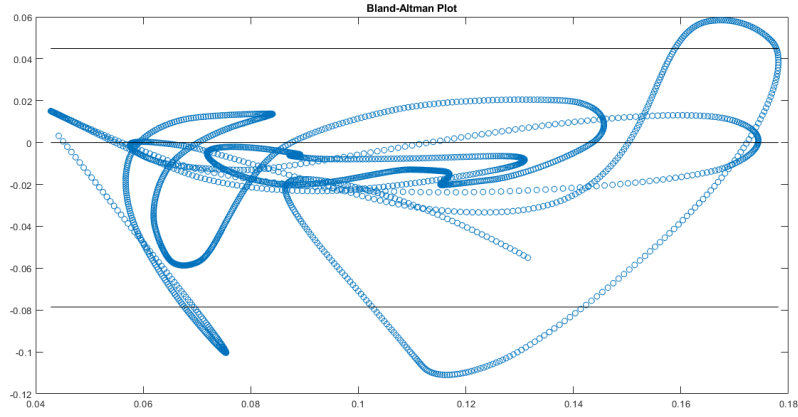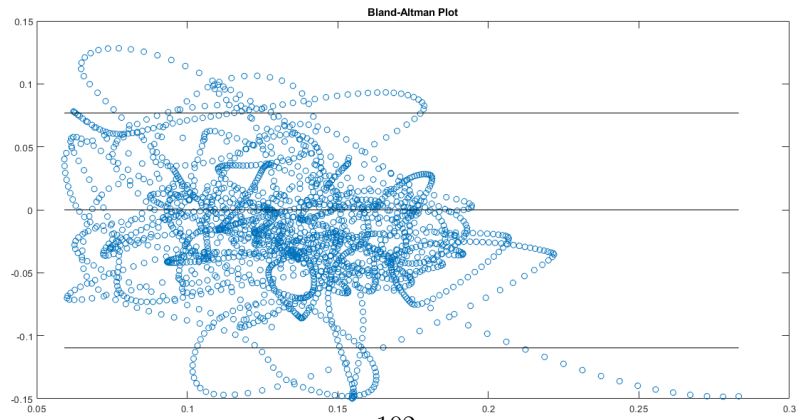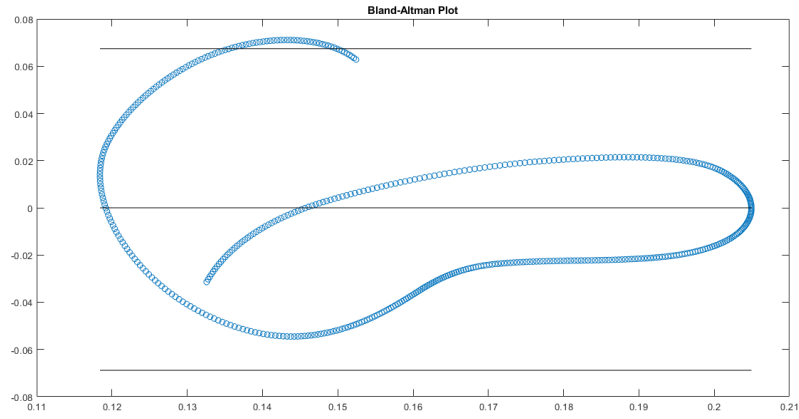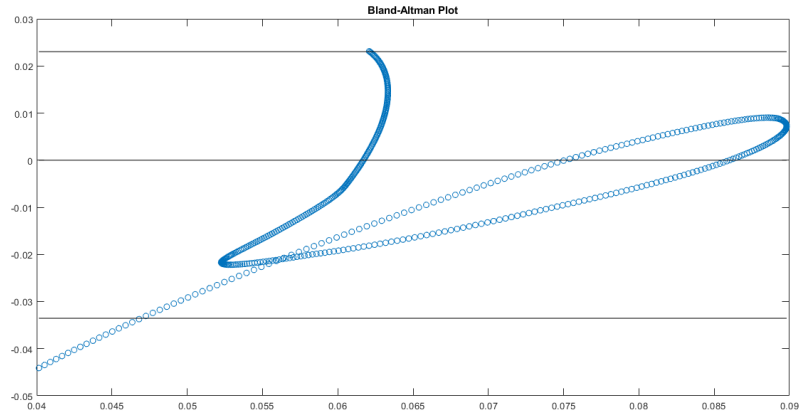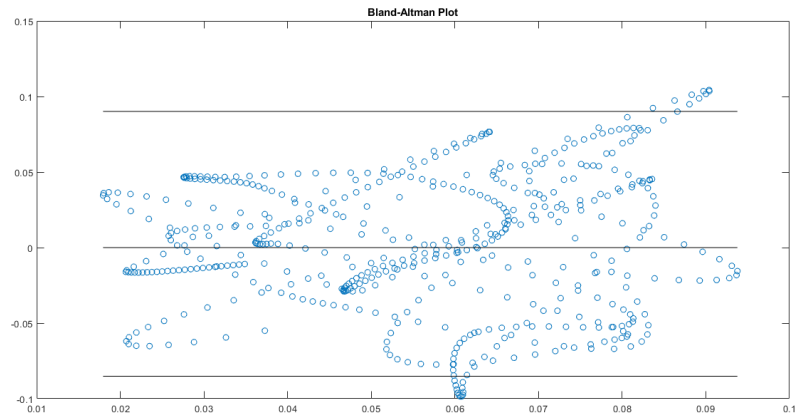Figure B.32: Subject 8, transverse plane Bland-altman plot of the CCI obtained with the two algorithms

Bibliography

[1] Weibel, E.R. (1963) Morphometry of the Human Lung. Springer Verlag and Academic Press, New York

[2] Cindy L. Stanfield, (2017) Principles of human physiology - VI edition, ISBN 978 88 7959 972 6

[3] https://medlineplus.gov/emphysema.html

[4] https://www.mayoclinic.org/diseases-conditions/emphysema/symptoms-causes/syc-20355555

[5] https://www.pulmonaryfibrosis.org/life-with-pf/about-pf

[6] Diagnostic radiology physics : a handbook for teachers and students. — Vienna : International Atomic Energy Agency, 2014. ISBN 978–92–131010–1

[7] Shah JP, Mann SD, McKinley RL, Tornai MP. Characterization of CT Hounsfield Units for 3D acquisition trajectories on a dedicated breast CT system. J Xray Sci Technol. 2018;26(4):535-551. doi: 10.3233/XST-17350. PMID: 29689765; PMCID: PMC6102078. doi: 10.3233/XST-17350

[8] Gattinoni L, Pesenti A, Matthay M. Understanding blood gas analysis. Intensive Care Med. 2018 Jan;44(1):91-93. [PubMed]

[9] Cowley NJ, Owen A, Bion JF. Interpreting arterial blood gas results. BMJ. 2013 Jan 16;346:f16. [PubMed]

[10] Larkin BG, Zimmanck RJ. Interpreting Arterial Blood Gases Successfully. AORN J. 2015 Oct;102(4):343-54; quiz 355-7. [PubMed]

[11] https://www.thoracic.org/professionals/clinical-resources/critical-care/clinical-education/abgs.php

[12] Chandan G, Cascella M. StatPearls [Internet]. StatPearls Publishing; Treasure Island (FL): Sep 3, 2020. Gas Laws and Clinical Application. [PubMed]

[13] "2017 ERS/ATS standards for single-breath carbon monoxide uptake in the lung." Brian L. Graham, Vito Brusasco, Felip Burgos, Brendan G. Cooper, Robert Jensen, Adrian Kendrick, Neil R. MacIntyre, Bruce R. Thompson and Jack Wanger. Eur Respir J 2017; 49: 1600016. Eur Respir J. 2018 Nov;52(5) [PubMed]

[14] Ponce MC, Sharma S. StatPearls [Internet]. StatPearls Publishing; Treasure Island (FL): Sep 2, 2020. Pulmonary Function Tests. [PubMed]

[15] Heckman EJ, O'Connor GT. Pulmonary function tests for diagnosing lung disease. JAMA. 2015 Jun 09;313(22):2278-9. [PMC free article] [PubMed]

[16] Rickey, Daniel. (1995). Evaluation of Doppler Ultrasound Velocity and Flow Measurements. 10.13140/RG.2.2.10944.53767.

[17] Genovese M. Ultrasound Transducers J Diagnostic Med Sonogr. 2016;32:48–53.

[18] https://www.nde-ed.org/Physics/Waves/attenuation.xhtml

[19] https://www.ndk.com/en/products/search/ultrasonic/index.html

[20] Hillis GS, Bloomfield P. Basic transthoracic echocardiography. BMJ. 2005;330:1432–6.

[21] de Valk et al.:The caval index: an adequate non-invasive ultrasound parameter to predict fluid responsiveness in theemergency department? BMC Anesthesiology 2014 14:114

[22] Mesin L., Albani S., Sinagra G. Non-invasive Estimation of Right Atrial Pressure Using Inferior Vena Cava Echography (2019) Ultrasound in Medicine and Biology, 45 (5) , pp. 1331-1337.

[23] Mesin, L.; Roatta, S.; Pasquero, P.; Porta, M. Automated Volume Status Assessment Using Inferior Vena Cava Pulsatility. Electronics 2020, 9, 1671. https://doi.org/10.3390/electronics9101671

[24] Luca Mesin, Paolo Pasquero, Silvestro Roatta, Multi-directional Assessment of Respiratory and Cardiac Pulsatility of the Inferior Vena Cava From Ultrasound Imaging in Short Axis,Ultrasound in Medicine & Biology, Volume 46, Issue 12, 2020, Pages 3475-3482, ISSN 0301-5629, https://doi.org/10.1016/j.ultrasmedbio.2020.08.027.

[25] Luca Mesin, Tatiana Giovinazzo, Simone D'Alessandro, Silvestro Roatta, Alessandro Raviolo, Flavia Chiacchiarini, Massimo Porta, Paolo Pasquero, Improved Repeatability of the Estimation of Pulsatility of Inferior Vena Cava, Ultrasound in Medicine & Biology, Volume 45, Issue 10, 2019, Pages 2830-2843,ISSN 0301-5629, https://doi.org/10.1016/j.ultrasmedbio.2019.06.002.

[26] Luca Mesin, Paolo Pasquero, Silvestro Roatta, Tracking and Monitoring Pulsatility of a Portion of Inferior Vena Cava from Ultrasound Imaging in Long Axis, Ultrasound in Medicine & Biology, Volume 45, Issue 5, 2019, Pages 1338-1343, ISSN 0301-5629, https://doi.org/10.1016/j.ultrasmedbio.2018.10.024.

[27] Jankowich MD, Rounds SIS. Combined pulmonary fibrosis and emphysema syndrome: a review. Chest. 2012;141:222–231. doi: 10.1378/chest.11-1062. [PMC free article] [PubMed] [CrossRef] [Google Scholar]

[28] Yildirimturk O, Tayyareci Y, Erdim R, Ozen E, Yurdakul S, Aytekin V, Demiroglu IC, Aytekin S. Assessment of right atrial pressure using echocardiography and correlation with catheterization. J Clin Ultrasound. 2011 Jul;39(6):337-43. doi: 10.1002/jcu.20837. Epub 2011 May 4. PMID: 21544830.

[29] https://courses.lumenlearning.com/boundless-ap/chapter/blood-vessel-structure-and-function/

[30] https://commons.wikimedia.org/wiki/File:Illu_quiz_lung05.jpg

[31] https://www.fda.gov/radiation-emitting-products/medical-x-ray-imaging/computed-tomography-ct

[32] https://commons.wikimedia.org/wiki/File:LungVolume.jpg

[33] Handbook of Speckle Filtering and Tracking in Cardiovascular Ultrasound Imaging and VideoChapter: 26Publisher: The Institution of Engineering and TechnologyEditors: Christos P. Loizou, Constantinos S. Pattichis, Jan D' hooge

[34] Mohamed, ASA 2015, Automated speckle tracking in ultrasound images of tendon movements , PhD thesis, University of Salford

[35] Dana Dabiri. Cross-Correlation Digital Particle Image Velocimetry – A Review . Department of Aeronautics & Astronautics Box 352400 University of Washington Seattle, WA, 98195

[36] Negoita M, Zolgharni M, Dadkho E, Pernigo M, Mielewczik M, Cole GD, Dhutia NM, Francis DP. Frame rate required for speckle tracking echocardiography: A quantitative clinical study with open-source, vendor-independent software. Int J Cardiol. 2016 Sep 1;218:31-36. doi: 10.1016/j.ijcard.2016.05.047. Epub 2016 May 14. PMID: 27232908

[37] Pedrizzetti, G., Claus, P., Kilner, P.J. et al. Principles of cardiovascular magnetic resonance feature tracking and echocardiographic speckle tracking for informed clinical use. J Cardiovasc Magn Reson 18, 51 (2016). https://doi.org/10.1186/s12968-016-0269-7

[38] Yo Fukushima (2021). curvspace (https://www.mathworks.com/matlabcentral/fileexchange/7233-curvspace), MATLAB Central File Exchange. Retrieved October 17, 2021.

[39] David Cumin (2021). Bland Altman Plot (https://www.mathworks.com/matlabcentral/fileexchange/24648-bland-altman-plot), MATLAB Central File Exchange. Retrieved October 28, 2021.

[40] Tal Hendel (2021). Ellipse Fit (https://www.mathworks.com/matlabcentral/fileexchange/22423-ellipse-fit), MATLAB Central File Exchange. Retrieved November 5, 2021.

[41] Lewis, J.P.. (2001). Fast Normalized Cross-Correlation. Ind. Light Magic. 10.

[42] Kaso A (2018) Computation of the normalized cross-correlation by fast Fourier transform. PLoS ONE 13(9): e0203434. https://doi.org/10.1371/journal.pone.0203434

Ringraziamenti

Terrei a ringraziare il mio relatore, il professor Luca Mesin, per avermi dato l'opportunità di lavorare a questa tesi, e per avermi guidato in quest'ultimo tratto della mia carriera universitaria. Vorrei anche ringraziare l'ingegnere Piero Policastro per la sua disponibilità nonostante il difficile periodo storico. Infine vorrei ringraziare i miei genitori, sia per avermi dato l'opportunità di studiare ciò che mi interessa, sia per il loro continuo sostegno e supporto, qualunque cosa facessi.